2017

Numerical Analysis Of Phase Change, Heat Transfer And Fluid Flow Within Miniature Heat Pipes

Mehdi Famouri
University of South Carolina

Recommended Citation

Famouri, M.(2017). *Numerical Analysis Of Phase Change, Heat Transfer And Fluid Flow Within Miniature Heat Pipes.* (Doctoral dissertation). Retrieved from http://scholarcommons.sc.edu/etd/4026

NUMERICAL ANALYSIS OF PHASE CHANGE, HEAT TRANSFER AND FLUID FLOW WITHIN MINIATURE HEAT PIPES

by

Mehdi Famouri

Bachelor of Science
Persian Gulf University, 2006

Master of Science
University of Mazandaran, 2008

Submitted in Partial Fulfillment of the Requirements

For the Degree of Doctor of Philosophy in

Mechanical Engineering

College of Engineering and Computing

University of South Carolina

2017

Accepted by:

Chen Li, Major Professor

Jamil Khan, Committee Member

Xingjian Xue, Committee Member

Xinfeng Liu, Committee Member

Cheryl L. Addy, Vice Provost and Dean of the Graduate School

DEDICATION

To my parents, Haj Ali Khan Famouri and Banoo Afzal Biglarbeygi, for their endless love, support and encouragements without which I would not be who I am, where I am.

اهدا

تقدیم به پدر و مادر مهربانم، حاج علی خان فاموری و بانو افضل بیگلربیگی، برای عشق، حمایت و تشویق بی انتهایشان که بدون انها نمیتوانستم این فردی باشم که همکنون هستم و در اینجایی باشم که همکنون هستم.

ACKNOWLEDGEMENTS

With immense pleasure and great respect, I express my whole-hearted gratitude, deep regards and sincere thanks to my PhD advisors Dr. Chen Li for his invaluable, thoughtful, and brilliant guidance throughout my PhD study at the University of South Carolina. His encouragement and support have been the constant source of inspiration ever since I entered this exciting field of research.

I would like to thank my committee members, Dr. Jamil Khan, Dr. Xingjian Xue and Dr. Xinfeng Liu for their invaluable advice and help throughout my research.

My sincere appreciation is extended to my co-advisors Dr. Gerardo Carbajal at the University of Turabo, Gurabo, Puerto Rico and Dr. Mahdi Abdollahzadeh at the University of Porto, Porto, Portugal for their time and help with my research.

I would like to express my sincere regards and thanks to all of my lab mates, especially Ahmed AbdulShaheed, GuangHan Huang for their suggestions, constant encouragement and generous help at all stages of my research work.

Special thanks to my fellow numerical friend, lab mate, lifelong friend, Mostafa Mobli for all the valuable numerical simulation and real life discussions we had over tea or other types of leisure activities.

Last but not least, the perpetual support and blessing of my family, which reinforced my determination throughout my career. Even to think of thanking them is to trivialize all they have done for me. My profound debt to them therefore, remains silent and unacknowledged.

ABSTRACT

Heat pipes with broad applications in thermal systems have the ability to provide effective heat transport with minimal losses in over reasonable distances due to their passive nature. Their exceptional flexibility, simple fabrication, and easy control, not to mention, all without any external pumping power make them especially attractive in electronics cooling. Heat pipe development is motivated to overcome the need to presumably manage thermal dissipation in progressively compressed and higher-density microelectronic components, while preserving the components temperatures to specification.

Computation of flow and heat transfer in a heat pipe is complicated by the strong coupling among the velocity, pressure and temperature fields with phase change at the interface between the vapor and wick. Not to mention, the small size and high aspect ratio of heat pipes brings their own challenges to the table. In this dissertation, a robust numerical scheme is employed and developed to investigate transient and steady-state operation of cylindrical heat pipes with hybrid wick structure for high heat fluxes based on an incompressible flow model. Despite many existing works, this is accomplished assuming as few assumptions as possible. The fundamental formulation of heat pipe is developed in such a way to properly take into account the change in the system pressure based on mass depletion\addition in the vapor core. The numerical sensitivity of the solution procedure on phase change at the liquid-vapor interface are recognized and effectively handled by

reformulating the mathematical equations governing the phase change. Hybrid wick structure of the heat pipe is modeled accurately to further investigate thermal and vicious novel wick structures.

A fully implicit, axisymmetric sequential finite volume method is devised in conjunction with the SIMPLE algorithm to solve the governing equations. ANSYS Fluent software with the power of User Defined Functions and User Defined Scalars is used to apply the numerical procedure in coupled system and standard levels. This two-dimensional simulation can solve for symmetrical cylindrical and flat heat pipes, as well as three-dimensional flat and non-symmetrical cylindrical heat pipes.

Using this powerful and reliable solver, a comprehensive parameter study is carried out to study the importance and effects of thermal properties, viscous properties, charging ratio, design parameter and the assumptions.

TABLE OF CONTENTS

LIST OF TABLES

LIST OF FIGURES

LIST OF SYMBOLS

A_E	Evaporation section area, m^2
A_C	Condensation section area, m^2
Cp	Specific heat, J/kg·K
C_E	Ergun's coefficient
C_f	comprerssion factor
h_{fg}	Latent heat, J/kg
h_∞	Coolant heat transfer coefficients, W/m^2·K
k	Thermal conductivity, W/m·K
k_{eff}	Wick effective thermal conductivity, W/m·K
K	wick permeability, m^2
L_E	Evaporation section length, m
L_A	Adiabatic section length, m
L_C	Condensation length of heat pipe, m
M	Mesh number, m^{-1}
m_i	Interface mass flow rate at node *i*, kg/s·m
M_w	Wick liquid mass, kg
M_v	Vapor liquid mass, kg
N_x	Number of axial nodes
N_r	Number of radial nodes for each domain
$\hat{P}$	Hydrodynamic pressure, Pa

P_{op}	System pressure, Pa
P_0	Reference pressure, Pa
q''	Input heat flux, W/m^2
Q	Input heat, W
Q_{loss}	Heat loss from the entire heat pipe, W
Q_{Out}	Heat output from condensation section, W
$Q_{in,real}$	Heat input from evaporation section, W
R	Gas constant, J/kg·K
t	Time variable, s
T	Temperature variable, ^{o}C
T_i	Interface temperature, ^{o}C
T_0	Reference temperature, ^{o}C
T_∞	Coolant temperature, ^{o}C
th	thickness, m
$\vec{u}$	Velocity vector, m/s
u_x	Axial velocity component, m/s
u_r	Radial velocity component, m/s
x	Axial coordinate, m
r	Radial coordinate, m

Greek symbols

Δx	*x*-direction width of control volume, m
Δr	*r*-direction width of control volume, m
ΔA	Face area of a control volume, m^2

ΔV	Volume of a control volume, m^3
ρ	Density, kg/m^3
μ	Viscosity, $N.s/m^2$
φ	Wick volumetric ratio
σ	Accommodation coefficient

Superscripts

0	Old values
*	Previous iteration value

Subscripts

l	Liquid
grv	Grooves
msh	Mesh
m	Mean value
o	Outside
s	Solid
v	Vapor
$wall$	Wall
w	Wick

CHAPTER 1:
INTRODUCTION

1.1 Background

Heat pipes are used widespread in broad applications since their operation is generally passive in essence. High heat transfer rates are doable by heat pipes over long distances, with minimal temperature difference, exceptional flexibility, simple fabrication, and easy control, not to mention, all without any external pumping power applied. Possible applications are varied from aerospace engineering to energy conversion devices, and from electronics cooling to biomedical engineering. Heat pipe development is motivated to overcome the need to presumably manage thermal dissipation in progressively compressed and higher-density microelectronic components, while preserving the components temperatures to specification [1]. For example, according to the report for NASA [2], reducing one pound of weight on a spacecraft can help save $10,000 US dollars in launch costs. Also, in terms of a telecommunication satellite, more than a hundred heat pipes are often required [3]. Many different types of heat pipes are developed in recent years to address electronics thermal management problems [4-6], solar energy [7-10] as well as lots of other applications [6, 11-14] and are shown promising results.

Heat pipes could be manufactured as small as 30 μm × 80 μm ×19.75 mm (micro heat pipes (MHPs)) or as large as 100 m in length [15]. Micro heat pipe concept is first proposed by Cotter [16] for the cooling of electronic devices. The micro heat pipe is characterized as a heat pipe in which the mean curvature of the liquid–vapor interface is comparable in magnitude to the reciprocal of the hydraulic radius of the total flow channel [17]. Typically, micro heat pipes have convex but cusped cross sections (for example, a polygon), with a hydraulic diameter in range of 10–500 μm [18]. A miniature heat pipe is defined as a heat pipe with a hydraulic diameter in the range of 0.5 to 5 mm [19]. However, the concept of micro and miniature heat pipes are not always properly addressed in the open literature the way mentioned earlier. For example, miniature heat pipes with micro grooves are sometimes improperly referred to as micro heat pipes [15]. Note, beyond the size ranges noted earlier, there are additionally other structural differences between micro and miniature heat pipes. A heat pipe in which both liquid and gas flow through a single noncircular channel is a true micro heat pipe where the liquid is pumped by capillary force, on the edges of channel, from the condensation section to the evaporation section [15]. An array of parallel micro heat pipes are normally mounted on the substrate surface to boost the area and consequently the heat transfer. Miniature heat pipes can be designed based on micro axially grooved structure (1D capillary structure), meshes or cross grooves (2D capillary structure).

The fluid flow, heat transfer and phase change in heat pipes needs to be better studied in order to improve the designs to costume specific applications and concepts. The effects of parameters such as thermal conductivity of the wick and wall, thickness of the wall, wick and vapor core, permeability of the wick, working fluid, operation conditions etc on the temperature, velocity and pressure distributions in the heat pipe have to be thoroughly addressed both in transient and steady-state operation to enrich a novel design. The analysis of the operation and performance of heat pipes has received a lot of attention, as reviewed by Faghri [20], Garimella and Sobhan [1], Faghri [15], Vadakkan [21], Carbajal [22], Ranjan [23], Issacci [24], Simionescu [25], Sharifi [26], Jiao [27], Chen and Faghri [28] and Singh [29].

1.2 Fundamentals of Heat Pipe

The operation of a heat pipe [15, 30] is simply explained based on a cylindrical geometry as an example, as shown in Figure 1.1, however, the shape and size of the heat pipes can be different. Heat pipes are consisted of a closed container (pipe wall and end caps), a wick region\structure, and working liquid in equilibrium state with its own vapor. Most used working fluid choices are water, acetone, methanol, ammonia, or sodium depending on the operating temperature. The exterior walls of heat pipe are split into three sections: the evaporator section, adiabatic section and condenser section. Although, a heat pipe can have no adiabatic section and also could have multiple evaporation and condensation sections depending on specific applications and design. The heat implemented to the outside wall of evaporator section is conducted through the wall of heat pipe first and then the wick region. At the interface of wick and vapor region, working fluid vaporizes to vapor and flows to the vapor core which increase the pressure of vapor core. The arisen vapor pressure is the driving force to push the vapor through the heat pipe to the condenser, where the vapor condenses to liquid flowing back to the wick region, releasing its latent heat of vaporization. On the other hand, the condensed liquid is pumped to the evaporation section through the wick region by the capillary pressure formed by the menisci in the wick structure. With this loop, the heat pipe can continuously carry the latent heat of vaporization\condensation back and forth between the evaporation and condensation sections. As long as there is enough capillary pressure as the driving force to push the liquid from condensation section to evaporation section, this loop will be continued [15].

The menisci at the liquid–vapor interface are highly curved in the evaporator section because the liquid recedes into the wick structures while in the condensation section, the menisci are close to flat, as shown in Figure 1.1 [15]. The surface tension between the working fluid and wick structure at the liquid-vapor interface is how the capillary pressure built and the change in the curvature of menisci along the heat pipe would vary the capillary pressure along the heat pipe. This capillary pressure gradient circulates the fluid against the liquid and vapor pressure losses, and adverse body forces, such as gravity or acceleration. The pressure drop along the vapor core is a results of friction, inertia and blowing (evaporation), and suction (condensation) effects, while the pressure drop along the wick region is mainly as a result of friction [15]. The liquid–vapor interface is not curved at the end of condensation section and that is where can be used as a zero reference point for hydrodynamic pressure. A typical liquid and vapor pressures drops are shown Figure 1.2, however, the axial pressure distribution can be different for the heat pipes with thin vapor core [31].

The maximum local pressure difference is developed near the end of evaporation section. The maximum capillary pressure should be as equal as or greater than the sum of the pressure drops in the wick region and vapor core, assuming there is no body forces. If there is any body forces, such as gravitational force (assuming it works against liquid pumping), the liquid pressure drop would be higher, meaning the capillary pressure should also be greater in order to have enough pumping power to circulate the working fluid. At normal heat pipe (normal vapor flow rates in the vapor core), the dynamic effects of vapor flow cause the pressure drop and increase along the heat pipe, as shown in Figure 1.2.

Basically, heat pipe theory deals with fundamentals of hydrodynamic and heat transfer. Fluid mechanics analysis is adopted to address the liquid and vapor flow (and pressure drops consequently) and also capillary pressure. Heat transfer is adopted to analysis the heat applied\removed, conjugate heat conduction in the wall and wick, evaporation\condensation at the liquid–vapor interface, and forced convection in the both vapor core and wick region. Fundamentally, one expects to analyze the internal thermal processes of a heat pipe as a thermodynamic cycle subject to the first and second laws of thermodynamics [32, 33].

As heat is being applied before the heat pipe reaches steady-state, the system pressure in the heat pipes increases with time as more evaporation occurs at the liquid-vapor interface than condensation. Even small changes in the net rate of phase change at the interface can cause large changes in system pressure since the liquid/vapor density ratio is large. Then, the interface pressure (also the saturation temperature) changes based on Clausius-Clapeyron equation as the system pressure changes. The rates of evaporation and condensation are dependent of the interfacial resistance [34], which itself is function both the interfacial pressure and bulk pressure. Not to mention, the density of vapor changes globally with system pressure and locally with temperature using the perfect gas law. These non-linear relationships however, can cause difficulties in the convergence of numerical schemes, particularly at high rates of heat addition [21].

1.3 Summary of Previous Heat Pipe Modeling

Assumptions and formulations play a very crucial role in the heat pipe simulation. A real simulation of heat pipe takes a lot of work and is almost impossible since phenomenon in multi scales levels need to be addressed. Some of the general critical drawbacks\advantages of heat pipe modeling efforts available in the literature are listed in this section.

1.3.1 Simplified Analytical Solution

Some researchers [35-39] simplified the equations based on many assumptions in order to be able to solve them analytically. Some of these assumptions are listed as but not limited to: steady-state, linear temperature profile across the wall and wick structure, constant saturation temperature at the liquid-vapor interface, predefined velocity distribution throughout the vapor core, predefined mass transfer pattern at the liquid-vapor interface, constant vapor pressure, constant vapor temperature, negligible viscous and inertia effects in the wick, constant thermal and viscous properties. Needless to say, the assumptions are not necessary valid for all the heat pipes geometries. In this study, none of the above assumptions are made.

1.3.2. Predefined\Assumed Phase Change Pattern

Some heat pipe simulations [35, 38, 40-45] assumed that evaporative length at the liquid-vapor interface is as a long as evaporation length outside of the heat pipe where the heat input applies. Also, the condensation at the liquid-vapor interface happens only along the condensation section outside of the heat pipe where the cooling happens. Moreover, the condensation and evaporation rates are assumed to be uniform which are calculated purely based on the amount of heat input and evaporation\condensation area outside of the heat pipe, which means it is assumed that 100% of heat is being transferred through phase change. These set of assumptions is only usable for steady-state modeling however depending on the problem, it might be a fair estimation or may not be. Some of the factors involving can be listed as: geometry of condensation and evaporation sections, thickness of the wick, effective thermal conductivity of the wick, velocity distribution within the wick, thermal conductivity of the wall and thickness of the wall. In this study, phase change has been calculated for all the cells at the interface and all the time steps. There is no assumption either where\when evaporation\condensation occurs, nor the amount of evaporation\condensation in this study.

1.3.3. Uniform\Constant Vapor Temperature\Pressure

Some of the numerical simulations of heat pipes [40, 46-48] assumed that the temperature of the vapor core is constant (steady-state) or uniform (transient). Also, the vapor pressure is sometimes assumed to be constant or uniform. It is clear they are not necessary accurate assumptions however they might result in satisfactory outcome, depending on the problem of course. For long heat pipes whereas the vapor core is long, the axial temperature difference might be crucial. Same thing goes for pressure as part of the pressure term comes from ideal gas law where pressure is a function of temperature. Not to mention, for thin vapor cores where the axial hydrodynamic pressure term is not negligible, the axial pressure difference in the vapor core can play a major role in the thermal performance of the heat pipe. In this study, both local temperature and pressure are calculated throughout the vapor core and such an assumption has no place.

1.3.4. System Pressure

System pressure in the vapor core is dealt with in different forms in previous studies whether the simulation is steady-state [28, 49] or transient [50-55] and whether the Navier–Stokes equations are solved compressible [22, 24, 28, 49-53, 55-59] or incompressible [21, 31, 60-64]. In the case of incompressible fluid flow in the vapor core, system pressure has to be assumed since the Navier-Stokes equations only include the pressure gradient term and not the pressure term itself. To the best of the author's knowledge, all the previous studies assumed compressible flow except the comprehensive work done by Vadakkan [21] which also reported\employed by Vadakkan et al. [31, 60, 61], Ranjan et al. [65, 66], Famouri et al. [63] and Solomon et al. [67]. Also in this study, incompressible formulation introduced by Vadakkan [21] is properly used to account the system pressure build-up with time.

1.3.5. Interface Pressure

The evaporation/condensation resistance at the interface are missed by the most existing publications and based on their methodology, the interface pressure and the system pressure are the same. Tournier and El-Genk [52] was the first work to incorporate the interfacial resistance into their formulation however in the form of compressible flow formulation with constant vapor temperature. Following, Vadakkan [21] was the first heat pipe incompressible formulation where the interfacial resistance is incorporated into the model along with temperature change in the vapor core. In this study, Vadakkan's [21] formulation is employed.

1.3.6. Hybrid Wick Modeling

The most important limitation in a heat pipe is the capillary limit which limits the maximum heat flux (also known as critical heat flux) that a heat pipe can handle before dry-out. The capillary limit is dependent on wicking capability of the wick structure. Not to mention, the heat pipe performance and efficiency are also a function of effective thermal conductivity, evaporative characteristics and also the permeability of the wick. With the advances in heat pipe technology, new hybrid wick structures [63, 68-72] are introduced and employed however not enough attempts are made to model them in the heat pipe. To the best of author's knowledge, Famouri et al. [63] is the first and only study to model a hybrid wick structure in a heat pipe, however, the effective viscous and thermal properties are calculated for the entire wick structure as one homogeneous structure. This might not be the best approach since different structures of the hybrid wick has its own characteristics, in the case of screen wire mesh and grooves as the hybrid wick for instance, the liquid can be pumped through the grooves easier and the screen mesh can enhance the evaporation and critical heat flux on the other hand. In this study, different structures of the hybrid wick region are treated differently meaning the wick region is modeled as a nonhomogeneous porous media.

1.4 Literature Review

There are many analytical and numerical studies on heat pipe based on varieties of assumptions and problems. They are presented here under different categories based on their importance related to this study.

1.4.1 Early Works

One of the earliest studies of the vapor flow in heat pipes was published by Cotter [73], where one-dimensional modeling, laminar, steady-state, incompressible flow were assumed based on a cylindrical heat pipe application. Later on, Cotter [16] introduced the idea of micro heat pipe for the first time and suggested the micro heat pipe is suitable where close temperature control is required. Bankston and Smith [74] parametrically studied the vapor flow in a cylindrical heat pipe based on a laminar, steady-state, incompressible and axisymmetric model using finite difference method. Using a steady-state 2D analysis, they shew that the one dimensional vapor flow model is not able accurately to predict the axial heat and mass transfer and pressure drop. Vapor flow in a flat heat pipe was investigated by Ooijen and Hoogendoorn [75] where a laminar, steady-state and incompressible model were used to study the pressure drop and velocity profile in the vapor core. A gas-filled heat pipe was studied by Bystrov and Goncharov [76] analytically and experimentally during start-up and five stages were categorized as: heat-transfer-agent melting to the onset of intense evaporation, formation of an axial vapor flux, sonic regime, rearrangement to subsonic regime, and switching to isothermal operation. A transient model was developed by Costello et al. [77] to model the heat pipe from frozen state through steady-state conditions. The model included compressible formulation for the vapor core and incompressible for the liquid in the wick. Pulsed heat pipe startup was studied by Ambrose et al. [78] and dry-out\rewetting was compared against capillary limit.

1.4.2 Reduced From

The compressible flow of vapor in a heat pipe and in the transient state was analyzed using a one-dimensional model by Jang et al. [79] and the numerical results were compared with experimental results. Faghri and Harley [80] introduced a transient lumped heat pipe formulation for different heating and cooling boundary conditions and the results were reported to be in good agreement with the existing experimental results. A steady-state closed form solution of cylindrical heat pipe was presented by Zhu and Vafai [38] based on a non-Daracian transport model for the fluid flow in the wick region and including incorporating the effects of liquid-vapor coupling. Shafahi et al. [44, 45] developed the work of Zhu and Vafai [38] to investigate the effects of using nanofluids in a cylindrical and flat-shaped heat pipes. Predefined mass transfer patterns were assumed for the liquid-vapor interface in these works (Ref.s [38, 44, 45]). Lefevre and Lallemand [81] introduced a two-dimensional steady-state coupled thermal and hydrodynamic model to analytically study flat micro heat pipes in three dimensions. Their method was employed and developed by Harmand et al. [39] and Sonan et al. [82] to study the transient thermal performance of flat heat pipes for electronic cooling. The vapor temperature was assumed constant in these studies (Ref.s [39, 81, 82]) and heat convection terms were neglected. Arab and Abbas [83] introduced a steady-state reduced-order model to analyze the effects of the thermophysical properties of working fluids.

1.4.3 Compressible

1.4.3.1 Steady-State

A concentric annular heat pipe has been developed and studied theoretically and experimentally by Faghri and Thomas [84, 85] to increase the heat capacity per unit length. Capillary limits and simple incompressible and compressible analysis were presented for the concentric annular heat pipe. Chen and Faghri [28] numerically solved the Navier-Stokes equations in cylindrical coordinates for the vapor flow and only pure conduction equations for the wick and wall region were solved. They analyzed the effects of single and multiple heat sources using a compressible, steady-state model. In a similar study but based on a steady-state model by Faghri and Buchko [49], a cylindrical heat pipe with multiple heat sources combinations investigated numerically and experimentally which is later used as a benchmark by most studies on cylindrical heat pipes. Using the same methodology but in three dimensions, Schmalhofer and Faghri [86, 87] studied circumferentially heated low temperature cylindrical heat pipe.

1.4.3.2 Transient

The vapor flow in a flat heat pipe is studied by Issacci et al. [56, 57] and Issacci [24] using a two-dimensional, transient and compressible model. They also reported that reverse flow can happen in the vapor core at the condensation and even adiabatic sections for high heat flux. Cao and Faghri [54] presented a transient, two-dimensional, compressible model based on cylindrical coordinates to analyze a heat pipe with pules heat inputs however, pure conduction model were used for the wick.. A high-temperature sodium/stainless steel cylindrical heat pipe was fabricated and tested by Faghri et al. [88, 89] and numerically studied the steady-state and transient responses of the heat pipe. The rarefied vapor flow were model for the first time by [55] based on a self-diffusion model to study the startup of a heat pipe from the frozen state based on a compressible, cylindrical and transient model. Cao and Faghri [55] studied a cylindrical heat pipe startup from frozen state based on an axisymmetric, cylindrical and compressible model. The heat transfer in the wall, wick and vapor were solved as a conjugate problem for the first time. A gas-loaded heat pipe is modeled by Harley and Faghri [90] based on a transient, compressible, two-dimensional and axisymmetric cylindrical model. They considered and numerically analyzed the noncondensable gas in the heat pipe as a separate entity for the first time. Tournier and El-Genk [50-53, 91] and Huang et al. [92] developed a compressible model to numerically study transient performance of cylindrical heat pipe taking into account the effect of interfacial pressure for the first time. They also modeled the wick as porous media and included the heat transfer convective terms in the wick for the first time. Carbajal [22] and Carbajal et al. [58, 59, 93] studied flat heat pipes in two and three dimensions based a compressible and transient model. They used kinetic theory to calculate the mass transfer at the interface and took into account the effect of the change in the size of the capillary radius along the liquid–vapor interface, for the first time based on Young–Laplace equation. They reported uniform temperature distribution on the cooling side of heat pipe while the heating side was subjected to a very non-uniform heat flux suggesting their flat heat pipe as a very good heat spreader.

1.4.4 Incompressible

1.4.4.1 Steady-State

Layeghi and Nouri-Borujerdi [94] and Nouri-Borujerdi and Layeghi [41, 95] studied the flow in the vapor core and wick in a concentric annular heat pipe using a steady-state incompressible model. They assumed predefined mass transfer patterns meaning evaporation and condensation only happen along the heating and cooling surfaces of the outer walls. Koito et al. [96], numerically investigated the thermal performance of flat-plate vapor camper based on a steady-state incompressible model. It was assumed that the entire liquid-vapor has a uniform temperature which was set to be the saturation temperature at a given pressure. Lu et al. [46] employed the simplified method suggested by Chen at al. [97] to model the fluid flow and heat transfer within a flat plate heat pipe with wick column in two dimensions. The liquid-vapor interface was assumed to have uniform temperature however, this interfacial temperature was calculated based on an energy balance. A steady-state incompressible model is used by Kaya and Goldak [98] based on Bai’s work [99] to simulate a cylindrical heat pipe in three dimensions. They did not assume any predefined mass transfer pattern at the interface however, they assumed a reference pressure, to calculate the pressure in the vapor core, only based on a guess of what the saturation temperature of the heat pipe was going to be. Thuchayapong et al. [42] studied the effects of capillary pressure on performance of a calendrical heat pipe based on a steady-state incompressible model. The capillary radius along a heat pipe was assumed to be a simple linear function while they assumed evaporation and condensation only happen along the heating and cooling surfaces of the outer walls. In a steady-state incompressible study by Pooyoo [40] in three dimensions, fluid flow and heat transfer was studied in a cylindrical heat pipe. Uniform temperature was assumed for the vapor core and the mass transfer at the liquid-vapor interface was predefined based on the evaporation and condensation lengths on the outside walls. They used a non-Darcy model to model the fluid flow in the wick region.

1.4.4.2 Transient

Transient behaviors of flat plate heat pipes was investigated by Xuan et al.[48] using a transient incompressible model however, the entire vapor was assumed to have uniform temperature and pressure and treated lump model is applied instead of solving for the vapor core. Not to mention, the convective heat transfer terms were neglected in the wick structure.

The most comprehensive incompressible model was introduced by Vadakkan [21] taking into account the interface resistance, temperature distribution in the vapor core, system pressure, mass depletion\addition in the vapor and wick regions, and variable density while no predefined mass transfer pattern were assumed. The proposed method is used in both two-dimensional [31] and three-dimensional [60, 61] flat heat pipes with single and multiple heat sources to investigate the steady-state and transient performance of the heat pipe. They also introduced an improved formulation to solve for the system pressure and interface temperature without which the solver is very unstable for high heat fluxes. Same numerical procedure followed by Famorui et al. [63] to investigate a polymer-based micro flat heat pipe with hybrid wicks in transient and state-state conditions. The very Vadakkan's model [21] was employed by Solomon et al. [67] to study effects of Cu/water nanofluid on thermal performance of a screen mesh cylindrical heat pipe and 20% heat transfer enhancement was reported. Famouri et al. [64] also adopted Vadakkan's model [21] to study different wick structures in a cylindrical heat pipe. In order to further increase the accuracy of Vadakkan's model [21], Ranjan [23] and Ranjan et al. [100] studied the wick microstructure effects such as meniscus curvature, thin-film evaporation, and Marangoni convection in micro scale and incorporated in the heat pipe in macro scale [62, 101]. A simplified transient incompressible model was proposed by Chen at al. [97] to study the thermal performance of vapor chambers (flat plate heat pipe). The heat transfer through the wick was assumed linear (only conduction) and uniform temperature was assumed for the liquid-vapor interface however, they proposed an equation based on a balance of energy in the vapor core to calculate this interfacial temperature each time step.

Same method but in three dimensions was applied to a heat sink embedded with a vapor chamber by Chen et al. [102] to investigate the effective conductivity of the vapor chamber.

1.5 Objectives of Dissertation

The goals of the present work are to employ and develop a robust numerical method to study the steady-state and transient performance of high heat flux heat pipes using as few assumptions as possible. Instead of playing with the thermal and viscous properties, the goal of this study is to compute them based on the real heat pipe experiments.

Since there is a strong coupling between the phase change at liquid-vapor interface, pressure, temperature and velocity fields, the numerical techniques to investigate steady-state and transient operation of heat pipe is very difficult to devise. Sequential pressure-based methods do not need storage requirement as much as other method and they are widely used in fluid flow and heat transfer problem, however, sequential procedures like SIMPLE algorithm [103], can experience difficulties in convergence when solving such strongly coupled systems of equations. One of the main objective of this study is to employ and develop a framework based on a sequential solution (SIMPLE algorithm) to design a stable and accurate computational procedure for heat pipe simulation, in the incompressible limit. The two key adjustments are: 1- The fundamental formulation of heat pipe is developed in such a way to properly take into account the change in the system pressure based on mass depletion\addition in the vapor core. 2- The numerical sensitivity of the solution procedure on phase change at the liquid-vapor interface are recognized and effectively handled by reformulating the mathematical equations governing the phase change. The outcome shows how stable this methodology is.

For the most part, the numerical simulation works have simply been using thermal and vicious properties for the wick structure of heat pipes without paying much attention to the background and some studies even played with these properties so they can get better results. One of the objectives of this study is to analyze the wick structure in details and use the most accurate models to estimate these properties for the wick. Moreover, hybrid wick structures are only modeled once however the model was not comprehensive and could not distinguish the unique features of the hybrid wick. Special attenuation is paid in this work to use a comprehensive model to predict the behavior of a hybrid wick.

Last but not least, not enough material is published to investigate the effects of each parameter on performance of heat pipe. Another goal of this work is to analyze the importance and effects of each parameter on temperature, velocity and pressure results in heat pipes.

1.6 Organization of Dissertation

The thesis is organized as follows. Chapter 1 introduced the operation of heat pipes, the previous works available in the literature, and explained the motivation for this study. Chapter 2 describes the mathematical model used in this work, including the details of the heat pipe structure, the governing equations, boundary conditions and initial conditions. Chapter 3 explains the details of numerical methods and tools used to solve the governing equations described in the previous chapter. Chapter 4 presents the validations process, results, comparisons and also the parameter study of the heat pipe. Chapter 5 summarizes the results and finding of the thesis and makes suggestions for future work.

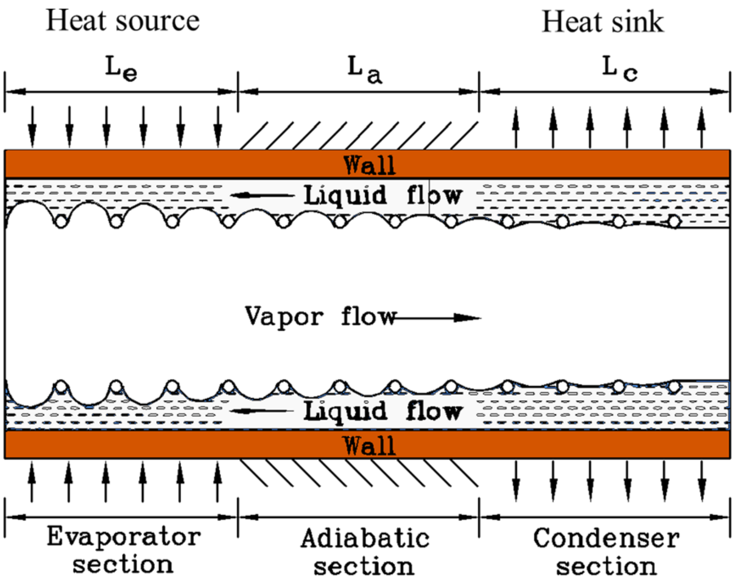

Figure 1.1 Schematic of a heat pipe showing liquid-vapor interface (Ref. [15])

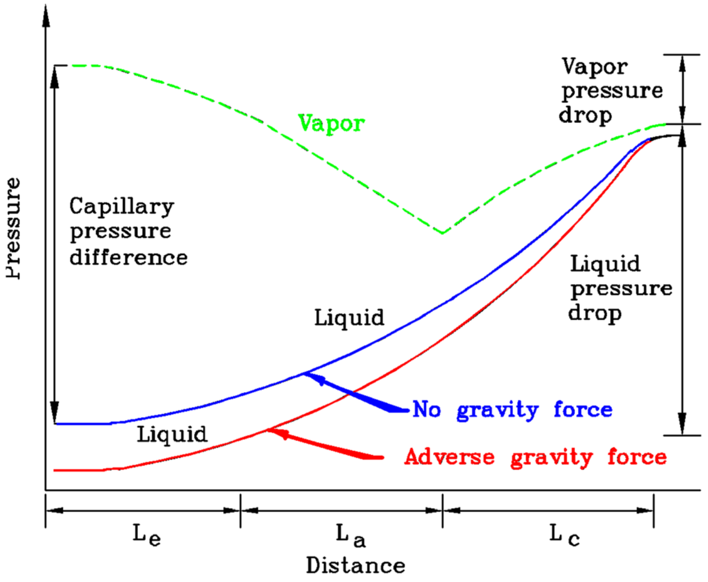

Figure 1.2 typical vapor and liquid pressure distribution inside a heat pipe (Ref. [15])

CHAPTER 2:
MODEL DESCRIPTION

This chapter shed light on the basics and details of the theories behind the phase change, heat transfer and fluid flow in heat pipes. The model is explained based on a two-dimensional cylindrical heat pipe however it can be easily applied to any other problems.

2.1 Problem Description

The schematic and physical representations of the cylindrical heat pipe are depicted in Figure 2.1 and Figure 2.2. Note, in order to show the details of the problem, this schematics are not to scale and all the dimensions in *r*-axis are exaggerated. Schematic radial and axial cross sections of the cylindrical heat pipe are shown in Figure 2.1 (a) and Figure 2.1 (b) respectively. The heat pipe chosen to be illustrated in Figure 2.1 consists of a combination of grooves and a mesh layer as the wick.

The physical dimensions of the two-dimensional cylindrical heat pipe along applied heat transfer conditions on evaporation and condensation sites have shown in Figure 2.2. Since the external applied heating and cooling are symmetric, the heat pipe can be modeled as an axisymmetric problem with the center line of the pipe being the axisymmetric line, as shown. The heat pipe is separated into three different regions: *Wall*, *Wick* and *Vapor* domains. The *Wall* domain is the very wall of the pipe which is made of copper and is treated as a solid phase. Meanwhile, the grooves on the wall of heat pipe and the screen mesh (if there is any) are considered as the *Wick* domain which is treated as a liquid phase but as a porous media. And the *Vapor* domain, is the very vapor core and only consists of vapor which is treated as an ideal gas. At the external surface of evaporation section, a uniform heat flux is applied while the condensation section external surface, an ambient temperature (T_∞ =21°C) with an average effective heat transfer coefficient (h_∞ =836.63 W/m^2.K) are. The wall and wick are made of copper and the working fluid is water. The heat pipe dimensions and other heat transfer parameters are chosen to correspond to an actual heat transfer experiment. The heat pipe is 370 mm long (L_E = 110 mm, L_A = 100 mm and L_C = 160 mm) with outside diameter of 12.7 mm (r_o = 6.35 mm) and 0.8 mm wall thickness (th_{wall} =0. 8 mm, r_w =5.55 mm).

2.1.1 Applied Heat Transfer

The heat pipe is tested with 5 different heat inputs ranging from 30 W to 150W applied to the evaporation section with the total area of 4.39×10^{-3} m^2 ($A_E = 2\pi \times r_o \times L_E$). However, because of the heat losses, the real heat input to the heat pipe is slightly less than the applied heat input, which is listed in Table 2.1 along with the corresponding heat fluxes. In order to accurately assess the heat loss during the operation of a heat pipe in evaporate section, as reported by Huang et al.[71], two thermal couples are mounted on the surface of thermal insulation outer surfaces and one thermal couple is used to measure the air temperature. The heat loss primarily comes from air convection, thus, the heat loss can correlated using the temperature difference, area of surface and a heat transfer coefficient. A set of preliminary experiments have been conducted to predict the heat loss by Huang et al.[71] based on the heat pipe investigated in this thesis.

A water heat exchanger is used to cool down the heat pipe. The condenser end of the heat pipe is placed in chamber of the heat exchanger and the gaps around the circumference were sealed to prevent water leakage and the water is flowed transverse to the condenser. Water is supplied with a large reservoir tank (thermostatic water source) and the water mass flow rate is carefully controlled to keep the condenser section temperature stable. The heat is dumped by flow of 21°C water (T_∞ =21°C) over the condensation section with the total area of 6.38×10^{-3} m^2 ($A_C = 2\pi \times r_o \times L_C$). Three different types of heat pipes are tested and the average condensation teampreature are listed in Table 2.2 for each heat input. The three tpes wich later would be explained in details are: ***Groove*** (type A), ***Fully Hybrid*** (type B) and ***Partially Hybrid*** (type C).

2.1.2 Wick Structures

The thermal and hydrodynamic performance of passive two-phase cooling devices such as heat pipes and vapor chambers is limited by the capabilities of the capillary wick structures employed. The desired characteristics of wick microstructures are high permeability, high wicking capability and large extended meniscus area that sustains thin-film evaporation [104]. Micro structures used in the heat pipe investigated in this study are groove and mesh.

2.1.2.1 Grooves

Axial helical traingular grooves are fabricitaed in the interior wall of the heat pipe envelope as the wick efficiently pulls condensate back to the evaporator from the cooler surfaces where working fluid had condensed. Axially grooved heat pipes work best where gravity is not a factor, e.g., in horizontal configurations or aerospace/satellite applications. Axial groove heat pipes are very efficient in returning condensate to the evaporation, cost less to fabricate than heat pipes with conventional wicks and have a long-range heat transfer capabilities [19, 105-108]. While the permeability of grooved wicks is high, capability in generating large capillary pressure is limitted [71]. Triangular helical grooves with the angel of 50°±5° and height of 0.28 mm (th_{grv} =0.28 mm) are mounted inside the pipe on the wall and there are 75±2 grooves in each pipe. More details about the grooves are depicted in Figure 2.3 (a) while a real photo of the pipe with the helical grooves studied in this dissertation is shown in Figure 2.3 (b).

2.1.2.2 Screen Mesh

Due to the ease of fabrication and high degree of accuracy with which the various parameters, such as volumetric porosity and specific surface area can be controlled, layers of sintered wire screen are often used in commercial applications to provide enhanced heat transfer or capillary assisted reflow in two-phase systems [67, 109-114]. These layers of wire screen are routinely used in numerous applications such as porous fins, capillary wick structures in heat pipes, filling materials and regenerators for Stirling engines, and many other applications. The woven copper screen mesh used in this study has wire diameter of 56 μm (d =56 μm) and mesh number of 5709 m^{-1} (M =5709 m^{-1} =145 $inch^{-1}$). Detailed geometric relationship of wire dimeter and the mesh number within a unit cell has been depicted in Figure 2.4 (a) and picture of a real copper screen mesh has been shown in Figure 2.4 (b). Screen mesh wick structure can be one layer or combined of a few layers of screen mesh. Two layers of screen mesh with compression factor of 0.9 (C_f =0.9) and thickness 0.2 mm (th_{msh} =2×2×d× C_f) are used as the screen mesh wick structure in the heat pipe studied in this dissertation.

2.1.2.3 Hybrid Wick

During the capillary evaporation, the counter interactions of flow resistance and capillary force determine the overall liquid supply and thus, the CHF. Fine copper woven meshes with microscale pores can generate high capillary pressure, but the associated flow resistance through the in-plane direction was significantly high [70]. Microgrooves [106, 108] or channels [115] were superior for liquid supply because of the low flow resistance, but with limited capillarity [108]. The combination of the advantages of single layer meshes and microchannels (grooves) could lead to a new type of capillary evaporating surfaces with high capillary pressure and low flow resistance, which would consequently result in much higher CHF than each individual [70]. This concept of hybrid wick to enhance the evaporation is illustrated in Figure 2.5 and is studied in Ref.s [63, 68-72, 110, 116, 117].

Schematic view of the cross sector of the cylindrical heat pipe (not-to-scale) with groove and hybrid wick are depicted in Figure 2.6 (a) and Figure 2.6 (b) respectively. As previously mentioned, the heat pipe wall thickness is 0.8 mm and the outside radius of the pipe is 6.35 mm (th_{wall} =0.8 mm, r_o =6.35 mm and r_w =5.55 mm). With the thickness of grooves and mesh to be 0.28mm and 0.20 mm respectively, the radiuses of vapor core for groove and hybrid heat pipe are 5.27 mm and 5.07 mm respectively (th_{grv} =0.28 mm, th_{msh} =0.20 mm, $r_{v,groove}$ =5.27 mm and $r_{v, hybrid}$ =5.07 mm)

With different combinations of screen mesh and grooves in the heat pipe, 3 different wick structures are developed and studied: *Groove* (Figure 2.7 (a)), *Fully Hybrid* (Figure 2.7 (b)) and *Partially Hybrid* (Figure 2.7 (c)). As for the partially hybrid case, the axial length of the mesh is considered to be as long as the evaporation length outside the heat pipe and is only mounted on top the groove at the evaporation site.

2.2 Assumptions

In the present study, the following assumptions are made:

- Both wick and vapor domains are assumed to be at equilibrium state throughout the process.
- Wick is assumed to be filled only by liquid and the vapor core only by vapor. There is no two-phase flow rather single phase flow at each domain.
- Fluid flow in both wick and vapor is assumed to be laminar.
- Fluid flow in both wick and vapor is assumed to be incompressible.
- Saturation condition was only assumed at the liquid vapor interface.
- The vapor core is assumed to follow ideal gas law.
- The temperature of the coolant is assumed to be constant at the condensation side with uniform heat transfer coefficient.
- All the dissipation effects were neglected.
- Liquid and vapor phases are assumed saturated at their corresponding initial pressure and temperature.
- The operational heat flux distribution is assumed below the critical heat flux.
- Constant material properties are assumed for solid phase.
- Constant material properties are assumed for liquid phase except the density.
- Constant material properties are assumed for vapor phase except the density.
- Partial isotropic and homogenous porous media is assumed. Different constant permeability, porosity, effective thermal conductivity are assumed for each type of wick structure.
- The gravity is assumed to have no effects on the heat pipe.
- It is assumed that the tangential component of interface velocity is negligible and the velocities at the liquid-vapor interface are normal to the interface.

- It is assumed that the vapor flow in the vapor core stays within subsonic limits.
- No-Slip boundary condition is assumed at the wick-wall interface.
- It is assumed that the numerical grid is made in such a way that neighboring cells at all the interface have the same contact area.
- Bubble generation, bubble size, the onset of nucleate boiling are not analyzed in this study.
- It is assumed that condensation and evaporation accommodation coefficients have the same value.

2.3 Governing Equations

The three computational domains of *Wall*, *Wick* and *Vapor*, as shown in Figure 2.2, are separately solved however they are coupled through boundary conditions at interfaces between them. In this section, all the equations used in the model are discussed in details.

Since a two-dimensional axisymmetric model is used, the equations are written in a cylindrical coordinate system however, only longitudinal (*x*) and radial (*r*) coordinates exist and the angular coordinate (θ) and all its correspondents are removed. For example, the velocity vector ($\vec{u}$) could originally be composed of 3 components ($\overrightarrow{u_x}, \overrightarrow{u_r}, \overrightarrow{u_\theta}$) in a cylindrical coordinate system however, it is consisted of only the radial ($\overrightarrow{u_r}$) and longitudinal ($\overrightarrow{u_x}$) components written as:

$$\vec{u} = \overrightarrow{u_x} + \overrightarrow{u_r} \tag{2.1}$$

Schematic view of the two-dimensional axisymmetric model with a grid is showcased in Figure 2.8 (a) with radial (*r*) and longitudinal (*x*) axes. Moreover, one cell is chosen to be showcased in Figure 2.8 (b) with radial (*r*) and longitudinal (*x*) velocities

($\overrightarrow{u_x}, \overrightarrow{u_r}$). Note, there is no grid in angular coordinate (θ) and the angle of the sector is only been shown to illustrate the model and the fact that the volume of cells change in radial (r) direction regardless of the grid.

Under the above assumptions and model, the governing equations are written as below.

2.3.1 Continuity Equation

The continuity equation for the *Wick* and *Vapor* domains can be written as

$$\varphi \frac{\partial \rho}{\partial t} + \frac{\partial}{\partial x}(\rho u_x) + \frac{\partial}{r \partial r}(r \rho u_r) = 0 \tag{2.2}$$

Where φ, ρ, t and r parameters are porosity (of the wick), density, time and radius respectively and the $\partial\rho/\partial t$ term accounts for the mass addition\depletion in the *Wick* and *Vapor* domains. Also, $\overrightarrow{u_x}$ and $\overrightarrow{u_r}$ are the axial and radial component of the velocity, respectively. Note the porosity is 1 (φ =1) for the *Vapor* domain and the velocity components ($\overrightarrow{u_x}, \overrightarrow{u_r}$) in the *Wick* domain are the volume-averaged value.

2.3.2 Momentum Equation

The two-dimensional axisymmetric momentum equations in the *Wick* and *Vapor* domains are written as:

$$\begin{aligned} \frac{\partial \rho u_x}{\partial t} + \frac{\partial}{r \partial x}(r \rho u_x u_x) + \frac{\partial}{r \partial r}(r \rho u_r u_x) \\ = -\frac{\varphi \partial P}{\partial x} + \frac{1}{r}\frac{\partial}{\partial x}\left(r\mu\left(2\frac{\partial u_x}{\partial x} - \frac{2}{3}(\nabla . \vec{u})\right)\right) \\ + \frac{1}{r}\frac{\partial}{\partial r}\left(r\mu\left(\frac{\partial u_x}{\partial r} + \frac{\partial u_r}{\partial x}\right)\right) + S_x \end{aligned} \tag{2.3}$$

$$\frac{\partial \rho u_r}{\partial t} + \frac{\partial}{r\partial x}(r\rho u_x u_r) + \frac{\partial}{r\partial r}(r\rho u_r u_r)$$

$$= -\frac{\varphi \partial P}{\partial r} + \frac{1}{r}\frac{\partial}{\partial x}\left(r\mu\left(\frac{\partial u_x}{\partial r} + \frac{\partial u_r}{\partial x}\right)\right)$$

$$+ \frac{1}{r}\frac{\partial}{\partial r}\left(r\mu\left(2\frac{\partial u_r}{\partial r} - \frac{2}{3}(\nabla.\vec{u})\right)\right) - 2\mu\frac{u_r}{r^2} + \frac{2}{3}\frac{\mu}{r}(\nabla.\vec{u}) \tag{2.4}$$

$$+ \rho\frac{u_x^2}{r} + S_r$$

Where μ, S_r and S_x are fluid dynamic viscosity, radial and axial component source term respectively. Moreover, S_r S_x and $\nabla.\vec{u}$ are as follow:

$$\nabla.\vec{u} = \frac{\partial}{\partial x}(u_x) + \frac{\partial}{r\partial r}(ru_r) \tag{2.5}$$

$$S_x = -\frac{\mu\varphi}{K}u_x - \frac{C_E\varphi\rho|\vec{u}|}{K^{\frac{1}{2}}}u_x \tag{2.6}$$

$$S_r = -\frac{\mu\varphi}{K}u_r - \frac{C_E\varphi\rho|\vec{u}|}{K^{\frac{1}{2}}}u_r \tag{2.7}$$

Where K,C_E and $|\vec{u}|$ are the Permeability, the Ergun coefficient of the porous media (*Wick* domain) and the absolute value of the velocity vector, respectively. Note, the Permeability is infinity ($K = \infty$) for the *Vapor* domain which makes the both source terms zero for the *Vapor* domain ($S_r = S_x = 0$).

2.3.3 Energy Equation

The two-dimensional axisymmetric energy equations for *Wall* (Eq. (2.8)), *Wick* (Eq. (2.9)) and *Vapor* (Eq. (2.10)) domains are as follow:

$$[\rho c_p]_s \frac{\partial T}{\partial t} = k_s\left(\frac{1}{r}\frac{\partial}{\partial r}\left(r\frac{\partial T}{\partial r}\right) + \frac{\partial^2 T}{\partial x^2}\right) \tag{2.8}$$

$$\left((1-\varphi)[\rho c_p]_s + \varphi[\rho c_p]_l\right)\frac{\partial T}{\partial t} + \frac{1}{r}\frac{\partial}{\partial r}\left([\rho c_p]_l r u_r T\right) + \frac{\partial}{\partial x}\left([\rho c_p]_l u_x T\right) = k_{eff}\left(\frac{1}{r}\frac{\partial}{\partial r}\left(r\frac{\partial T}{\partial r}\right) + \frac{\partial^2 T}{\partial x^2}\right) + \emptyset \tag{2.9}$$

$$[\rho c_p]_v \frac{\partial T}{\partial t} + \frac{1}{r}\frac{\partial}{\partial r}\left([\rho c_p]_v r u_r T\right) + \frac{\partial}{\partial x}\left([\rho c_p]_v u_x T\right) = k_v\left(\frac{1}{r}\frac{\partial}{\partial r}\left(r\frac{\partial T}{\partial r}\right) + \frac{\partial^2 T}{\partial x^2}\right) + \emptyset \tag{2.10}$$

Where k, c_p and $\emptyset$ are thermal conductivity, heat capacity and viscous dissipation respectively. Also, suberscript s, l and v are referring to solid, liquid and vapor properties, respectively. Moreover, k_{eff} is the effective conductivity of the *Wick* domain which is calculated based on both the conductivity of the solid and liquid, and also the type of wick structure used. The viscous dissipation in a two-dimensional axisymmetric model is written as Eq. (2.11) however, this term is negligible for such a low velocity application and this term is set to be zero ($\emptyset = 0$) in this study.

$$\emptyset = 2\mu\left\{\left(\frac{\partial u_r}{\partial r}\right)^2 + \left(\frac{u_r}{r}\right)^2 + \left(\frac{\partial u_x}{\partial x}\right)^2\right\} + \mu\left\{\left(\frac{\partial u_x}{\partial r} + \frac{\partial u_r}{\partial x}\right)^2 - \frac{1}{3}(\nabla.\vec{u})^2\right\} \tag{2.11}$$

2.4 Boundary Conditions

As mentioned previously, the domains are coupled only through the boundary condition at the interfaces between them. Not to mention, the phase change which is the most important aspect of the heat pipe happens at the interface between the Wick and Vapor domain. Therefore, the boundary conditions are the most critical part of this model. All the boundary conations applied to the *Wall, Wick* and *Vapor* domains are explained in this section.

2.4.1 Outside Wall

The boundary conditions for the outside wall for evaporation (Eq. (2.12)), adiabatic (Eq. (2.13)) and condensation (Eq. (2.14)) sections are listed below. These boundary conditions are the only mechanisms to apply\remove heat to\from heat pipe, as shown in Figure 2.2.

$$-k\frac{\partial T}{\partial r} = q'' \qquad r = r_o, 0 \le x \le L_E \tag{2.12}$$

$$-k\frac{\partial T}{\partial r} = 0 \qquad r = r_o, L_E < x < L_E + L_A \tag{2.13}$$

$$-k\frac{\partial T}{\partial r} = h_\infty(T - T_\infty) \qquad r = r_o, L_E + L_A \le x \le L_E + L_A + L_C \tag{2.14}$$

2.4.2 Wick-Wall Interface

The velocity and temperature boundary conditions for the interface between *Wall* and *Wick* domains are listed below. At this interface, the fluid is assumed not slip on the solid wall (no-slip boundary condition) which leads to Eq. (2.15). Also, assuming the energy balance at this interface, Eq. (2.16) is derived.

$$\mathrm{u_r} = u_x = 0 \qquad r = r_w, 0 \le x \le L_E + L_A + L_C \tag{2.15}$$

$$-k_s\left[\frac{\partial T}{\partial r}\right]_{Wall} = -k_{eff}\left[\frac{\partial T}{\partial r}\right]_{Wick} \qquad r = r_w, 0 \le x \le L_E + L_A + L_C \tag{2.16}$$

As shown in Figure 2.9, the grids are made in way that the axial grid are exactly in line in all the domains (Figure 2.9 (a)) and therefore, the contact area between the two cells from different domains are identical at their interface (Figure 2.9 (b)). That is why the Eq. (2.16) is simplified and there is no area term included since the cells areas from both sides were identical. Note there is no gap between the domains in reality and the gap in Figure

2.9 is only made to shed light on the details of the model and there is only one interface between two domains. Moreover, the same assumption is made for Wick-vapor interface in this study too.

2.4.3 Vapor-Wick Interface

It is assumed that the *Wick* domain is always filled with a liquid and the *Vapor* domain with vapor, therefore, phase change only and exactly happens at the Vapor-Wick interface. Also, it is assumed that the velocities are only normal to the interface which means the axial component of the velocity ($\vec{u}_x$) are assumed to be zero (Eq. (2.17)) at the both side of the Vapor-Wick interface. Also, the entire mass transfer from phase change is being transferred in radial direction through radial component of the velocity ($\vec{u}_r$). Since the mass transfer is the same and the densities are different for the *Wick* and *Vapor* domains, the radial velocities for *Wick* and *Vapor* domains are different (Eq. (2.18) and Eq. (2.19)) and their ratio is the ratio of the densities in two domains. The velocity boundary conditions are listed below for the Wick-Vapor interface.

$$[u_x]_{\mathrm{Wick}} = [u_x]_{\mathrm{Vapor}} = 0 \qquad r = r_v, 0 \le x \le L_E + L_A + L_C \tag{2.17}$$

$$[u_r]_{\mathrm{Wick}} = \frac{\dot{m}''}{\rho_l} \qquad r = r_v, 0 \le x \le L_E + L_A + L_C \tag{2.18}$$

$$[u_r]_{\mathrm{Vapor}} = \frac{\dot{m}''}{\rho_v} \qquad r = r_v, 0 \le x \le L_E + L_A + L_C \tag{2.19}$$

Where $\dot{m}''$ is the local mass flux which is the local mass flow rate ($\dot{m}$) per area and is calculated as follow for each cell.

$$\dot{m}'' = \frac{\dot{m}}{\Delta A} \tag{2.20}$$

Where ΔA is the contact area of the interface cell in one domain with the corresponding interface cell on the other domain. Also, $\dot{m}<0$ denotes evaporation and $\dot{m}>0$ denotes condensation.

The energy balance boundary condition is used to calculate the interface temperature (T_{int}) as follow.

$$-k_{eff}\left[\frac{\partial T}{\partial r}\right]_{\text{Wick}} = -k_v\left[\frac{\partial T}{\partial r}\right]_{Vapor} + \dot{m}''^{h_{fg}} \qquad r = r_v, 0 \le x \le L_E + L_A + L_C \tag{2.21}$$

Where h_{fg} is the latent heat of the working fluid and there is no area term for the same reason mentions previously. The interfacial energy balance (Eq. (2.21)) presented here (and also Ref.s [22, 58, 59, 63, 93, 118]) is a more accurate representation than the interfacial energy balance previously used (Eq. (2.22)) by Ref.s [21, 31, 54, 61]. They included the sensible heat, however, they did not consider that the latent heat occurs at a reference temperature and not at absolute zero [118].

$$-k_{eff}\left[\frac{\partial T}{\partial r}\right]_{\text{Wick}} + \dot{m}''c_{p,l}T_{int} = -k_v\left[\frac{\partial T}{\partial r}\right]_{Vapor} + \dot{m}''c_{p,v}T_{int} + \dot{m}''h_{fg} \tag{2.22}$$

The local mass flux at the Wick-Vapor interface is calculated as follow (Eq. (2.23)) and also Ref.s [21, 31, 60, 61, 63]) based on the kinetic theory [34].

$$\dot{m}'' = \left(\frac{2\sigma}{2-\sigma}\right)\frac{1}{(2\pi R)^{1/2}}\left(\frac{P_v}{(T_v)^{1/2}} - \frac{P_{int}}{(T_{int})^{1/2}}\right) \tag{2.23}$$

Where R, σ and P_{int} are gas constant, accommodation coefficient and interface pressure, respectively. The accommodation coefficient is set to be 0.03 (σ =0.03) in this study however, it will be thoroughly investigated later on in this work. The pressure at the interface (P_{int}) can be calculated from the Clausius-Clapeyron (Eq. (2.24)) equation and based on the interface temperature (T_{int}) calculated from Eq. (2.21).

$$\frac{R}{h_{fg}} ln\left(\frac{P_{int}}{P_0}\right) = \frac{1}{T_0} - \frac{1}{T_{int}} \qquad (2.24)$$

Where P_0 and T_0 are the reference values.

2.4.4 Axisymmetric Line

Because of the symmetry line, all the derivative normal o the symmetry line is zero but also, because this is an axisymmetric cylindrical model, the radial component of the velocity is also zero. Therefore, the boundary conditions on the axisymmetric line are written as:

$$\frac{\partial \mathrm{T}}{\partial r} = \frac{\partial u_x}{\partial r} = u_r = 0 \qquad r = 0, 0 \leq x \leq L_E + L_A + L_C \qquad (2.25)$$

2.4.5 Lateral Walls

All the lateral walls are assumed adiabatic, thus the temperature gradients normal to the walls are zero. Also, all the velocity components are zero based on the no-slip boundary condition. The boundary conditions on all the left walls (Eq. (2.26)) and right walls (Eq. (2.27)) are the same and as listed below.

$$\frac{\partial \mathrm{T}}{\partial x} = u_x = u_r = 0 \qquad x = 0, 0 \leq r \leq r_o \qquad (2.26)$$

$$\frac{\partial \mathrm{T}}{\partial x} = u_x = u_r = 0 \qquad x = L_E + L_A + L_C, 0 \leq r \leq r_o \qquad (2.27)$$

2.5 System Parameters

In transient operation, the system pressure in the heat pipes changes as vaporization and condensation occur at the liquid-vapor interface in the wick structure, as mentioned previously. The system pressure also changes the interface pressure, and consequently, the saturation temperature through the Clausius-Clapeyron equation. System level parameters and their correspondents are discussed in this section.

2.5.1 Mass of Vapor and Liquid

There is both evaporation and condensation mass transfer in a heat pipes, either in transient or steady-state, however, their amounts are not equal if the steady-state is not reached. For instance, the amount of mass transferred through evaporation is more than the amount of mass transferred through condensation if the heat pipe is heating up (or less if the heat pipe is cooling down). This mass difference is added\depleted to\from the Vapor\Wick domain during the process of heating\cooling of the heat pipe. Thus, the amount of the mass in each domain is changing during the process which can be calculated (Eq. (2.28)) by summing the mass flow rate on the Wick-Vapor interface. Since $\dot{m}$<0 denotes evaporation and the heat pipe is heating up (more evaporation than condensation) in this study, the mass difference ($\dot{m}_{balance}$) is always positive and can be written as:

$$\dot{m}_{balance} = \sum_{W-V} -\dot{m}'' \times \Delta A \tag{2.28}$$

Where "W-V" refers to the Wick-Vapor interface. The mass of fluid can be calculated in both Vapor (Eq. (2.29)) and Wick (Eq. (2.30)) domains by integrating the mass change over time as follow:

$$M_v = M_v^0 + \Delta t \left(\sum_{W-V} -\dot{m}'' \times \Delta A \right) \tag{2.29}$$

$$M_l = M_l^0 - \Delta t \left(\sum_{W-V} -\dot{m}'' \times \Delta A \right) \tag{2.30}$$

WhereM_v^0, M_l^0 and Δt are initial mass of vapor, initial mass of liquid and the numerical time step. Since the heat pipe is heating up (more evaporation than condensation) in this study, the mass of vapor in increasing and the mass of the liquid is decreasing which cause changes in both system pressure in the vapor core and the densities in both *Wick* and *vapor* domains.

2.5.2 System Pressure

The hydrodynamic pressure differences are relatively small compared to the absolute operating pressure assuming incompressible flow. However, the hydrodynamic pressure term is not neglected. The pressure term is expressed in two separate components:

$$P = \hat{P} + P_{op} \tag{2.31}$$

Where P_{op} and $\hat{P}$ are the system operation pressure and local hydrodynamic pressure of the Vapor domain. Note, P_{op} is a function of time and overall mass balance (mass addition\depletion) as explained previously. The system pressure (P_{op}) does not change locally and is a system level parameter. Moreover, the hydrodynamic pressure ($\hat{P}$) is calculated locally and from the pressure term in the Navier-Stokes equations. Based on the continuity equation and pressure correction procedure by Patankar [103], the pressure gradients in the momentum equation are calculated, however, there is need to be a reference point to calculate the $\hat{P}$ from Navier-Stokes equations. This reference point is chosen to be the very end of condensation section on the Wick-Vapor interface line ($\hat{P}(x = L_E + L_A + L_C, r = r_v) = 0$).

Based on the ideal gas law ($M = PV/(RT)$), the mass of the vapor can be written as:

$$M_v = \frac{P_{op}}{R} \sum_{V} \frac{\Delta V}{T_v} \tag{2.32}$$

Where ΔV is the volume of the cell and "V" means the summation is done over all the cells in the *Vapor* domain. Including Eq. (2.29) into Eq. (2.32), the system pressure can be calculated as:

$$P_{op} = \frac{M_v^0 + \Delta t(\sum_{W-V} - \dot{m}'' \times \Delta A)}{\frac{1}{R}\sum_V \frac{\Delta V}{T_v}} \tag{2.33}$$

2.5.3 Density of Vapor and Liquid

In keeping with the incompressible flow assumptions, the local vapor density is calculated based on the system pressure and ideal gas law as:

$$\rho_v = \frac{P_{op}}{RT_v} \tag{2.34}$$

Also, in order to take into account the mass depletion from the Wick domain, the mean liquid density is computed as:

$$\rho_l = \frac{M_l}{\varphi V_{wick}} \tag{2.35}$$

Where V_{Wick} is the total volume of the Wick domain.

2.6 Initial Conditions

It is assumed that the both *Wick* and *Vapor* domains are at equilibrium and saturated state at their corresponding initial pressure and temperature. Thus, the *Wick* domain is assumed to be filled only by saturated liquid and the *Vapor* domain only by saturated vapor. The heat pipe is assumed to start working from the cooling temperature (T_∞) (which is close to the room temperature), therefore, the initial temperature for all three domains are the temperature of the coolant Eq. (2.36). Also, the reference temperature (T_0) for Clausius-Clapeyron equation is chosen to be the coolant temperature. The system pressure (P_{op}), reference pressure (P_0) and the pressure term at the *Vapor* domain ($P_v(x,r)$) are set to be the corresponding saturation pressure at the initial temperature which is the very coolant temperature (Eq. (2.37)). Since there is no heat applied at the initial condition, there is no phase change and there is no velocity and consequently, hydrodynamic pressure at both *Wick* ($P_l(x,r)$) and *Vapor* ($\hat{P}(x,r)$) domains are set zero (Eq. (2.38)). The density of the *Vapor* domain is set to be density of the vapor at the saturation temperature of the coolant (Eq. (2.39)). All the initial conditions can be summarized as follow:

$$T(x,r) = T_0 = T_\infty \qquad t = 0 \tag{2.36}$$

$$P_v(x,r) = P_{op} = P_0 = P_{sat}(T = T_\infty) \qquad t = 0 \tag{2.37}$$

$$u_r(x,r) = u_x(x,r) = P_l(x,r) = \hat{P}(x,r) = \dot{m}(x) = \dot{m}''(\mathrm{x}) = 0 \qquad t = 0 \tag{2.38}$$

$$\rho_v(x,r) = \rho_{sat}(T = T_\infty) \qquad t = 0 \tag{2.39}$$

2.7 Effective Thermal and Viscous Properties of the Wick

Parameters such as effective thermal conductivity, effective permeability of the porous media, effective Ergun's coefficient and even the porosity are often unknown for complex structures in the wick which are crucial to be addressed. In heat pipes for instance, the largest transverse temperature gradients happen within the wick domain compared to other domains which is proportional to the effective thermal conductivity of the wick. The calculation of these effective parameters based on different models are included and discussed in this section.

2.7.1 Porosity

Porosity which is the ratio of the fluid volume over the total volume in the unit cell is purely a function of the geometry of the wick structure.

2.7.1.1 Grooves

The details geometry of triangular helical grooves are shown in the Figure 2.3. The porosity of grooves (*φ*) can be calculate as the area ration of fluid over the total. The areas can be calculated mathematically based on the radiuses and the angles of the pipe and grooves. They can also be calculated by making the geometry in a software and use the software tools to obtain the areas. As listed in Eq. (2.40), the porosity is computed based on the total and fluid areas within one cell of grooves as follow:

$$\varphi = \frac{A_{fluid}}{A_{totall}} = \frac{9.048 \times 10^{-8}\ m^2}{1.269 \times 10^{-7}\ m^2} = 0.713 \qquad (2.40)$$

2.7.1.2 Mesh

The details geometry of screen mesh is shown Figure 2.4. The porosity (*φ*) of the screen mesh is function of wire diameter (*d*), the opening width of mesh (*w*) and compression factor (c_f). The mesh number (*M*) of the mesh can be calculated as:

$$M = \frac{1}{d + w} \qquad (2.41)$$

A comprehensive study of different models to calculate the porosity of the screen mesh can be found in Ref.s [113, 119-122]. Li and Petereson [113] also suggested the porosity of the multilayer screen mesh can be calculated (based on Figure 2.4 (b)) as:

$$\varphi = 1 - \pi \frac{Md\sqrt{1 + (Md)^2}}{4c_f} = 0.707 \qquad (2.42)$$

Where d =56 μm, M =5709 m^{-1} and C_f=0.9 as mentioned previously.

2.7.2 Thermal Conductivity

The effective thermal conductivity of each wick structure is a function of geometry and material properties of solid and liquid involved.

2.7.2.1 Grooves

The most basic model to estimate the effective thermal conductivity of the grooves wick structure is the volume average of the fluid conductivity and the solid conductivity as:

$$k_{eff} = \varphi k_f + (1-\varphi)k_s \tag{2.43}$$

Where k_f and k_s are thermal conductivities of fluid and solid, respectively.

The most frequently used correlation for predicting the effective thermal conductivity of a porous media was first proposed by Rayleigh [123] which is sued by many researchers in the field of heat pipe (Ref.s [49, 54, 67, 80, 90, 118, 124]) as:

$$k_{eff} = \frac{k_f\left(k_f + k_s - (1-\varphi)(k_f - k_s)\right)}{k_f + k_s + (1-\varphi)(k_f - k_s)} \tag{2.44}$$

However, since the geometry of the grooves is not complex, one can built a model for conduction heat transfer and estimate the effective thermal conductivity. As described in Figure 2.10 (a) and Figure 2.10 (b), the combination of solid and liquid can be model as a series of resistances where the effective resistance can be formulated as:

$$\frac{1}{R_{eff}} = \frac{1}{R_{f,a}} + \frac{2}{R_s + R_{f,b}} \tag{2.45}$$

Where the resistance of each element can be calculated based on their corresponding widths, heights and thermal conductivity as:

$$R_{f,a} = \frac{H}{k_f(L-L_s)}, R_s = \frac{\frac{H}{2}}{k_s\frac{L_s}{2}}, R_{f,b} = \frac{\frac{H}{2}}{k_f\frac{L_s}{2}} \tag{2.46}$$

Where the H, L, L_s are the height of the grooves, width of the groove and width of the solid part of the grooves, respectively. Combining the Eq. (2.46) and Eq. (2.45), the effective thermal resistance can be formulated as:

$$\frac{1}{R_{eff}} = \frac{1}{H}\left(k_f(L - L_s) + \frac{2k_s k_f L_s}{k_f + k_s}\right) \tag{2.47}$$

And the effective thermal conductivity of the grooves can be predicated as:

$$k_{eff} = k_f\left(1 - \frac{L_s}{L}\right) + \frac{2k_s k_f}{k_f + k_s}\frac{L_s}{L} \tag{2.48}$$

On the other hand, as shown in Figure 2.10 (c) and Figure 2.10 (d), the combination of solid and liquid can be model as parallel resistances where the effective resistance can be formulated as:

$$\frac{1}{R_{eff}} = \frac{1}{R_{f,a}} + \frac{2}{R_{f,b}} + \frac{2}{R_s} \tag{2.49}$$

Where the resistance of each element can be calculated based on their corresponding widths, heights and thermal conductivity as:

$$R_{f,a} = \frac{H}{k_f(L - L_s)}, R_s = \frac{H}{k_s\frac{L_s}{4}}, R_{f,b} = \frac{H}{k_f\frac{L_s}{4}} \tag{2.50}$$

Combining the Eq. (2.49) and Eq. (2.50), the effective thermal resistance can be formulated as:

$$\frac{1}{R_{eff}} = \frac{1}{H}\left(k_f(L - L_s) + \frac{k_s L_s}{2} + \frac{k_f L_s}{2}\right) \tag{2.51}$$

And the effective thermal conductivity of the grooves can be predicated as:

$$k_{eff} = k_f\left(1 - \frac{L_s}{L}\right) + \frac{k_s + k_f}{2}\frac{L_s}{L} \tag{2.52}$$

From an ideal and purely physical perspective a parallel arrangement offers the least thermal resistance to heat flow, while a series arrangement results in the greatest resistance, and the upper (Eq. (2.53)) and lower (Eq. (2.54)) limits can be defined by the equations for perfect parallel and series cases, respectively.

$$k_{eff} = \varphi k_f + (1-\varphi)k_s \tag{2.53}$$

$$k_{eff} = \left(\frac{\varphi}{k_f} + \frac{1-\varphi}{k_s}\right)^{-1} \tag{2.54}$$

Note, the upper limit effective thermal conductivity is the very volume average of the fluid conductivity and the solid conductivity.

Also, as formulated by Bhattacharya et al. [125] and used by Carbajal et al. [59] in a heat pipe modeling (Λ =0.35), the effective thermal conductivity can be calculated as a linear interpolation of upper and lower level based a correlated constant (Λ) as:

$$k_{eff} = \Lambda\big(\varphi k_f + (1-\varphi)k_s\big) + (1-\Lambda)\left(\frac{\varphi}{k_f} + \frac{1-\varphi}{k_s}\right)^{-1} \tag{2.55}$$

More information on different models and methods can be found in Ref.s [113, 125-130] however not directly related to the effective conductivity of the grooves.

Moreover, a heat conduction model can be made and solved to predict the effective thermal conductivity of grooves since the geometry is not complex. A pure heat conduction model as shown in Figure 2.11 is defined with the real dimensions containing the fluid, grooves and heat pipe wall. The side walls are assumed adiabatic (symmetry) and different heat transfer boundary conditions are implemented to apply different types and values of heat input and output.

The model is developed and solved along with the boundary conditions based on the corresponding material properties with ANSYS Fluent. A temperature distribution showcased in Figure 2.12 with a heat flux of 10^4 W/m^2 applied to the right wall (BC1: q =10^4 W/m^2) and convective heat transfer boundary condition on the left wall with the ambient temperature of 50 K and heat transfer coefficient of 500 W/(m^{2}K) (BC2: T_∞ =50 K, h_∞ =500 W/(m^{2}K)).

If the heat transfer assumed one dimensional (in r direction) throughout the groove (combination of solid and liquid), one can rewrite the Fourier's law as:

$$Q = k_{eff} A_{mid} \frac{\Delta T}{\Delta r} \tag{2.56}$$

Where Q is the heat being transfer and A_{mid} is the plain area in the middle of grooves (between the "top" and "bot" plains). In order to calculate the effective thermal conductivity of the model in r direction, the weighted-average temperature of top (T_{top}) and bottom (T_{bot}) of the grooves have to be calculated as shown in Figure 2.11. The effective thermal conductivity can be formulated as:

$$k_{eff} = \frac{\dfrac{Q}{\dfrac{A_{top} + A_{bot}}{2}}}{\dfrac{\mathrm{T_{bot}} - T_{top}}{\Delta \mathrm{r}}} \tag{2.57}$$

Where Δr =0.28×10^{-3} m, A_{top} =0.465×10^{-3} m^2 and A_{bot} =0.441×10^{-3} m^2. The T_{top} and T_{bot} are calculated using ANSYS Fluent "Reports" tools based on weighted-average temperature on the "top" and "bot" surfaces. The model is run for various boundary conditions (constant temperature, heat flux and convection heat transfer) on the both right (BC1) and left (BC2) walls of the model and the results are listed in Table 2.3 along with the heat input\output (Q) and the effective thermal conductivity of the grooves (k_{eff}). The effective thermal conductivities, calculated based on the model introduced in this study, changes from 1.6801 W/(m.K) to 1.7925 W/(m.K) which is relatively only 6% of total change. The average of effective thermal conductivity of all the models is calculated to be 1.72 W/(m.K) as listed in Table 2.3. Also, same procedure based on the same model is followed for ethanol as the fluid and the effective thermal conductivity of the grooves with ethanol is calculated to be 0.54 W/(m.K). After all, the effective thermal conductivity of the grooves based on different models is calculated for water and ethanol as the fluid and summarized in Table 2.4. The results from numerical modeling are sued in this study to represent the effective thermal conductivity of the grooves.

2.7.2.2 Mesh

The most frequently used correlation to predict the effective thermal conductivity of a single layer of screen mesh was first proposed by Rayleigh [123] Eq. (2.44) however, Hsu et al. [131] demonstrated this correlation is not accurate to predict the effective thermal conductivity of layers of screen mesh. Also, more models are introduced by Ref.s [132-135]. It is studied that the contact conditions between the wires and also the individual layers have a crucial impact in the effective thermal conductivity of the wire screen, and understanding of the contact conditions is very important to accurately predict the effective thermal conductivity [113]. More detailed models and discussions can be found in the Ref [113]. They also suggested that the effective thermal conductivity of the screen mesh can be simplified to Eq. (2.58) if the ratio of thermal conductivities of fluid to solid is less than 0.01 (k_l/k_s <0.01) as:

$$k_{eff} = 1.42 k_s \frac{(Md)^2}{c_f} = 62.50 \tag{2.58}$$

Note, the thermal conductivity of the fluid is not present in this equation, therefore, the same effective thermal conductivity is used for ethanol.

2.7.3 Permeability

Permeability is constant that proportionally relates pressure drop across porous media to fluid flow based on Darcy’s Law (Eq. (2.59)). The lower the permeability, the more pressure drop occurs for the same fluid flow in porous media. The permeability is independent of the nature of the fluid but it depends on the geometry of the medium [136]. For example, Darcy's Law based on permeability in x direction can be written as:

$$u = -\frac{K}{\mu}\frac{\partial P}{\partial x} \tag{2.59}$$

Where K is the permeability.

2.7.3.1 Grooves

In order to calculate the permeability of the grooves, a three-dimensional model (open channel) as long as 0.2 m (L =0.2 m) but the same cross section as the grooves is used. The model is solved for different inlet velocities and the corresponding pressure drops along the channel are calculated based on Eq. (2.60).

$$K = \frac{L\mu U}{\Delta P} \tag{2.60}$$

Where L, U, ΔP are the channel length, inlet velocity and pressure drop respectively. The results based on the numerical model are presented in Table 2.5. As shown, the permeability is calculated to be 3.00×10^{-9} m^2. More information and discussion on effective permeability of the grooves can be found in Ref.s [137-139].

2.7.3.2 Mesh

The permeability of wire screen mesh as suggested by [30] and used by [21, 35, 40, 118] can be calculated as:

$$K = \frac{d^2\varphi^3}{122(1-\varphi)^2} = 1.06\ \times 10^{-10} \tag{2.61}$$

According to Joseph et al. [140], the appropriate modification to Darcy's equation is to be replaced:

$$\nabla P = -\frac{\mu}{K}\vec{u} - c_f K^{-\frac{1}{2}}\rho|\vec{u}|\vec{u} \tag{2.62}$$

Where c_f is a dimensionless form-drag constant. This equation is known as Forchheimer equation and last term is known as the Forchheimer term. Irmay [141] derived an alternate equation in one direction as:

$$\frac{\partial P}{\partial x} = -\frac{\beta\mu(1-\varphi)u}{d^2\varphi^3} - \frac{\alpha\rho(1-\varphi)u^2}{d\varphi^3} \tag{2.63}$$

Where α and β are shape factors that must be determined empirically [136]. With α = 1.75 and β = 150 this equation is known as Ergun's equation [142]. Making the linear terms of Eq. (2.62) and Eq. (2.63) identical [136], the permeability can be calculated as:

$$\mathrm{K} = \frac{d^2\varphi^3}{\beta(1-\varphi)^2} \tag{2.64}$$

By making the quadratic terms of Eq. (2.62) and Eq. (2.63) identical, drag constant in Eq. (2.62) can be written as [136]:

$$c_f = \alpha\beta^{-1/2}\varphi^{-3/2} \tag{2.65}$$

Since the drag constant is calculated based on Ergun's equation later on, the permeability of the screen mesh in this study should be calculated based Eq. (2.64) as:

$$K = \frac{d^2\varphi^3}{150(1-\varphi)^2} = 8.62 \times 10^{-11} \tag{2.66}$$

More insight can be found through Ref.s [143-145].

2.7.4 Ergun's Coefficient

The Ergun coefficient (C_E) is the very drag constant (c_f) in Eq. (2.62) when it is calculated using the shape factors (α and β) as introduced by [142] and discussed earlier. The Ergun coefficient is strongly dependent on the flow regime. For slow flows, C_E is very small. Thus, the second term on the right hand side of Equation Eq. (2.62) is very small and can be neglected. This reduces the Forchheimer equation to the Darcy equation. As the flow velocity increases, inertial effects also increase and the flow adapts to the Forchheimer flow regime. These inertial effects are accounted for by the Ergun coefficient (C_E) and the kinetic energy of the fluid ($\rho|u|u$). However, according to [146-148], a constant Ergun coefficient C_E is valid as long as the fluid flow is laminar.

The Ergun coefficient is set to be 0.5 in heat pipe simulation by Ref.s [21, 22, 31, 58, 60, 61, 63, 93, 118] however no explanation found. The Ergun coefficient (C_E) in this study and as well as Ref.s [40, 98] is calculated as [136]:

$$C_E = \alpha\beta^{-1/2}\varphi^{-3/2} \tag{2.67}$$

With α = 1.75 and β = 150. C_E is calculated as 0.237 and 0.240 for grooves and screen mesh respectively.

Table 2.1 Applied heat inputs, heat losses, real heat inputs and heat fluxes.

Q (W)	Q_{loss}(W)	Q_{real} (W)	q'' (W/m^2)
30	0.87	29.13	6636.97
60	2.49	57.51	13104.19
90	3.91	86.09	19615.52
120	5.70	114.30	26043.15
150	9.49	140.51	32014.84

Table 2.2 Average condensation temperatures and heat transfer coefficients for each heat input for Groove, Fully Hybrid and Partially Hybrid heat pipe.

Q (W)	Q_{real} (W)	Condensation Temperature (°C)			h_∞ (W/m^2.K)		
		Type A	Type B	Type C	Type A	Type B	Type C
30	29.13	24.88	25.63	28.09	1175.87	985.21	643.27
60	57.51	30.72	28.81	32.48	927.25	1153.97	784.61
90	86.09	35.90	32.59	36.75	905.09	1163.47	856.45
120	114.3	40.48	36.51	43.25	919.03	1154.64	804.67
150	140.51	44.70	39.08	48.49	928.83	1217.54	800.65

Table 2.3 Different boundary conditions and the corresponding effective thermal conductivities

BC1 K, W/m^2	BC2 K, W/m^2, W/(m^{2}K)	T_{bot} (K)	T_{top} (K)	Q (W)	k_{eff} (W/(m.K))
T =500	T_∞ =300, h_∞ =2000	499.44	452.22	134.41	1.7582
T =500	T_∞ =100, h_∞ =2000	498.89	404.43	268.81	1.7582
T =500	T_∞ =10, h_∞ =2000	498.63	382.93	329.29	1.7582
T =500	T_∞ =10, h_∞ =200	499.83	484.50	41.90	1.6886
T =500	T_∞ =10, h_∞ =350	499.70	473.59	71.64	1.6948
T =500	T_∞=10, h_∞=500	499.59	463.25	100.05	1.7010
q =10^6	$q = -10^6$	299.37	103.76	531.98	1.6801
q =10^5	$q = -10^5$	999.94	980.38	53.20	1.6801
q =10^4	$q = -10^4$	999.99	998.04	5.32	1.6801
q =10^5	T_∞ =10, h_∞ =1000	149.59	130.49	53.20	1.7209
q =10^5	T_∞ =10, h_∞ =3000	68.50	50.16	53.20	1.7925
q =10^4	T_∞ =50, h_∞ =500	76.03	74.10	5.32	1.7010
				Average	1.72

Table 2.4 Summary of different models of effective thermal conductivity of the grooves for water and ethanol

Model	k_{eff}	
	Water	Ethanol
Upper Limit (Eq. (2.53))	111.67	111.37
Volume Average (Eq. (2.43))	111.67	111.37
Parallel Resistance (Eq. (2.52))	109.28	108.97
Numerical Model (Table 2.3)	1.72	0.54
Rayleigh [123] (Eq. (2.44))	1.08	0.32
Series Resistances (Eq. (2.48))	0.94	0.28
Lower Limit (Eq. (2.54))	0.84	0.25

Table 2.5 Inlet velocities, pressure drop and the corresponding permeability

u_{avg} (m/s)	Δp (Pascal)	K (m^2)
0.001	66.80199	3.00×10^{-9}
0.01	668.1113	3.00×10^{-9}
0.1	6689.025	3.00×10^{-9}
1.0	67578.45	2.97×10^{-9}

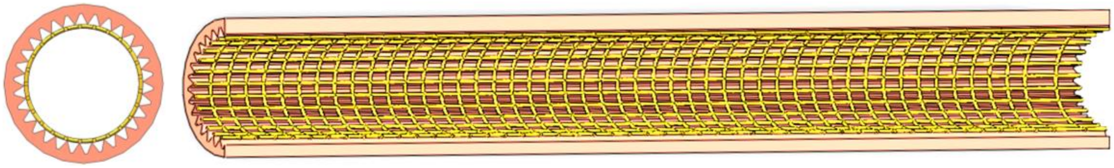

(a) (b)

Figure 2.1 Schematic radial (a) and axial (b) cross sections of the cylindrical heat pipe.

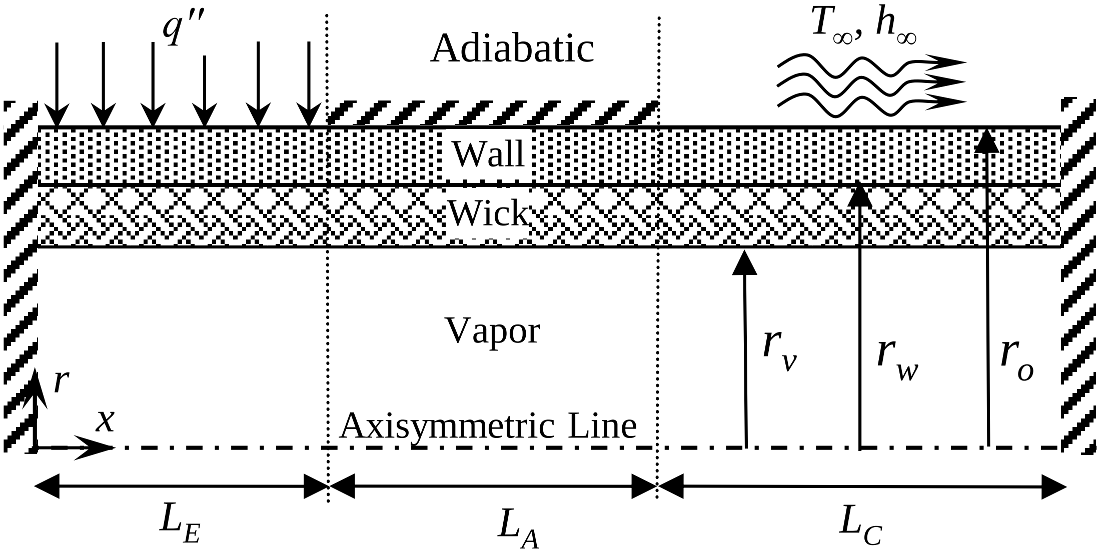

Figure 2.2 Schematic view of the cylindrical heat pipe (not-to-scale).

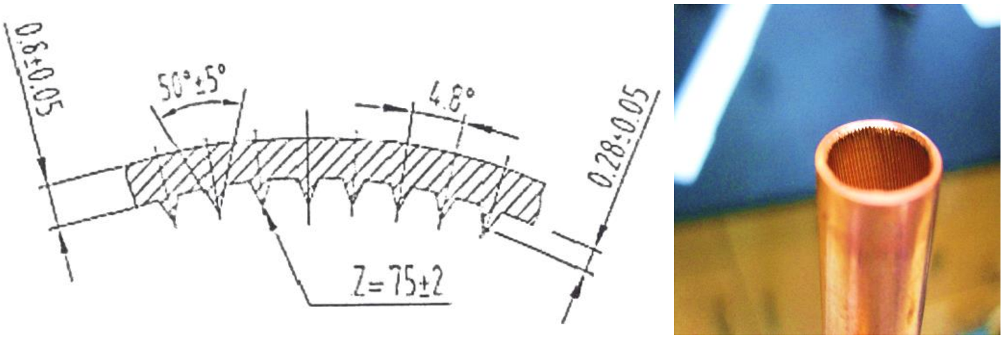

(a) (b)

Figure 2.3 (a) Details of the triangular grooves (b) A real photo of the heat pipe with the triangular helical grooves.

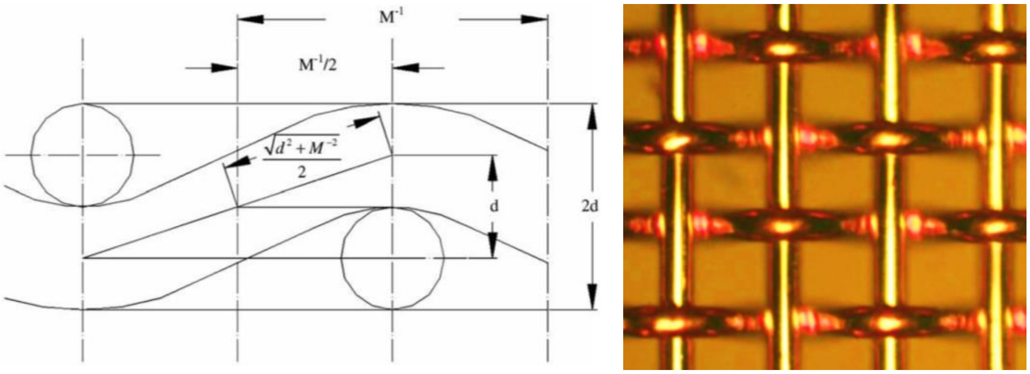

(a) (b)

Figure 2.4 (a) Geometric relationship of unit cell [113] (b) Woven copper screen mesh [116]

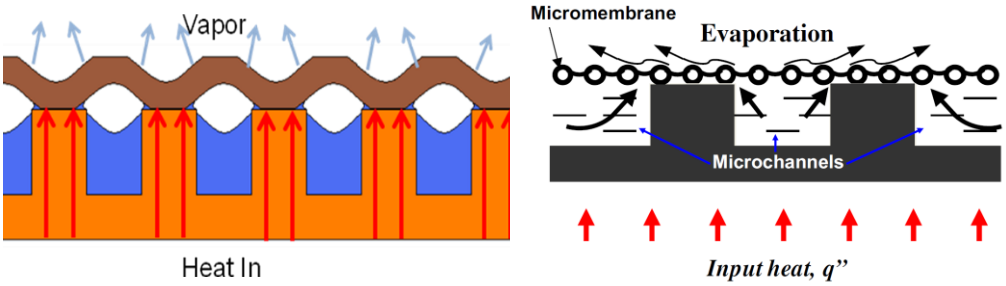

(a) (b)

Figure 2.5 Schematic of hybrid wick concept (a) Woven copper mesh on top of the copper pillars [116] (b) Micromembrane-enhanced evaporating surfaces [70]

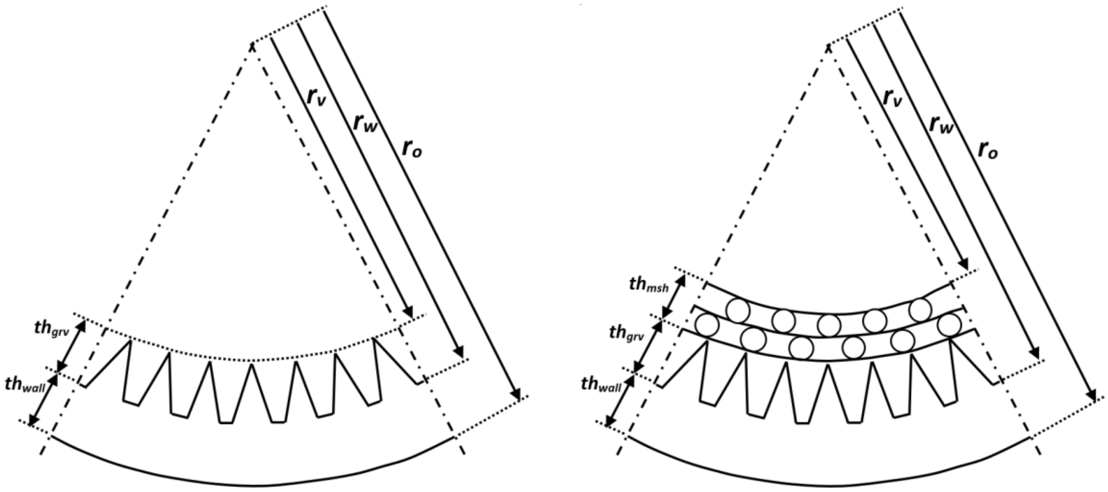

(a) (b)

Figure 2.6 Schematic view of the cross sector of the cylindrical heat pipe (th_{wall} =0.8 mm, th_{grv} =0.28 mm and th_{msh} =0.20 mm) (a) groove wick (r_v =5.27 mm) (b) hybrid wick (r_v =5.07 mm).

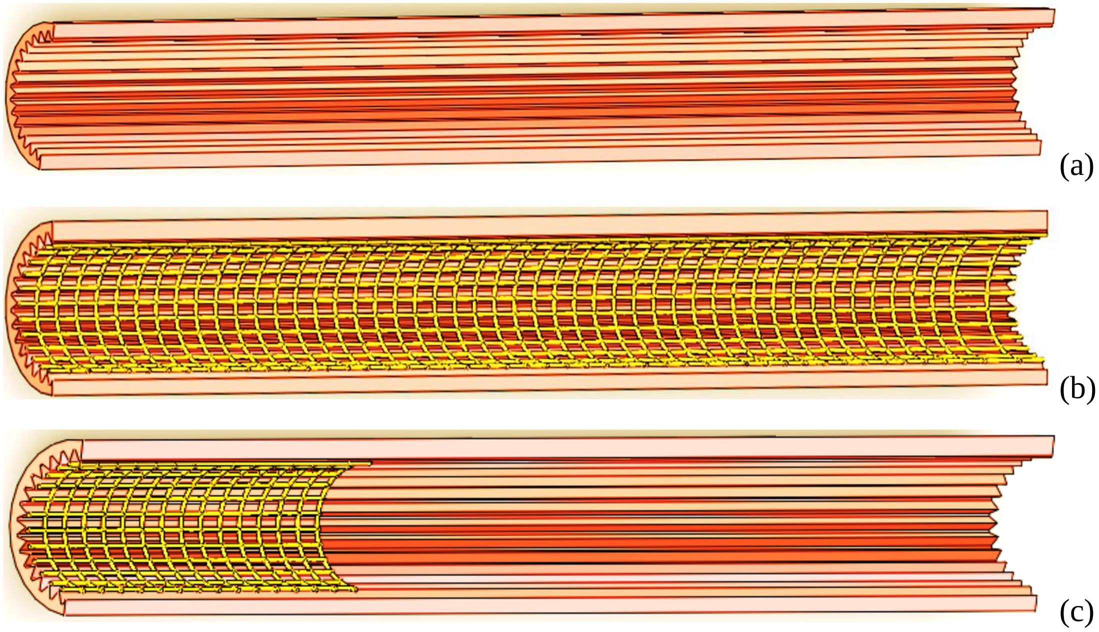

Figure 2.7 Schematics of (a) Groove heat pipe, (b) Fully Hybrid heat pipe (c) Partially Hybrid heat pipe.

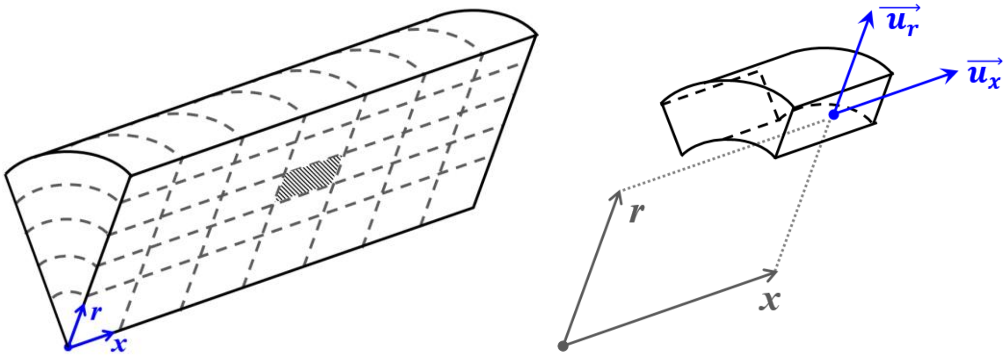

(a) (b)

Figure 2.8 Schematic view of the two-dimensional axisymmetric model (a) Showcase of the grid (b) Showcase of a cell and the velocity components

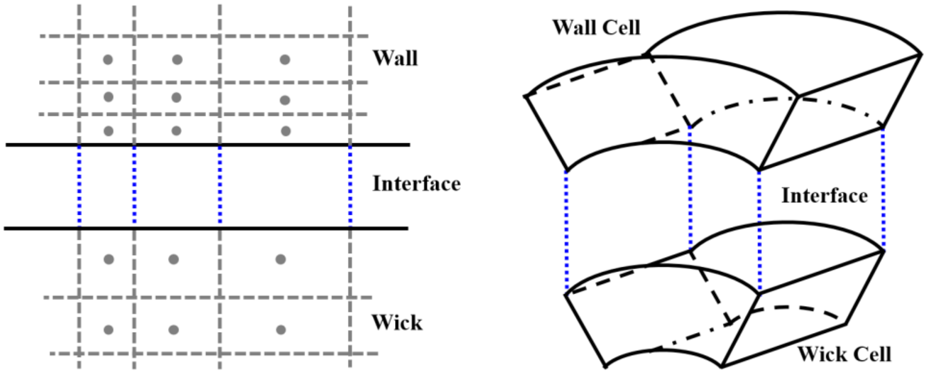

(a) (b)

Figure 2.9 Identical contact area between the cells from different domains (a) axial grid in two different domains (b) cells from two different domains

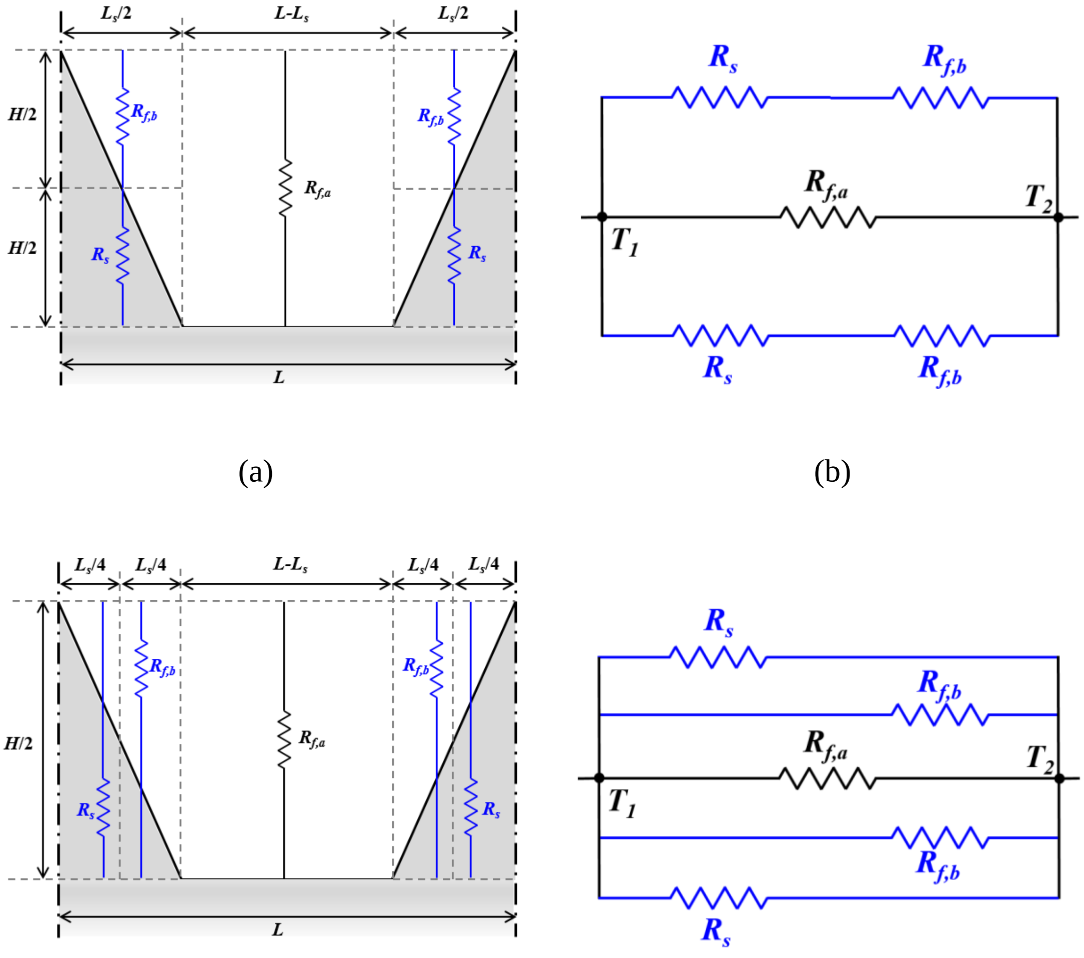

(a) (b)

(c) (d)

Figure 2.10 Thermal resistance modeling of grooves (a) series geometry model, (b) series resistance circuit, (c) parallel resistance geometry model, (d) parallel resistance circuit

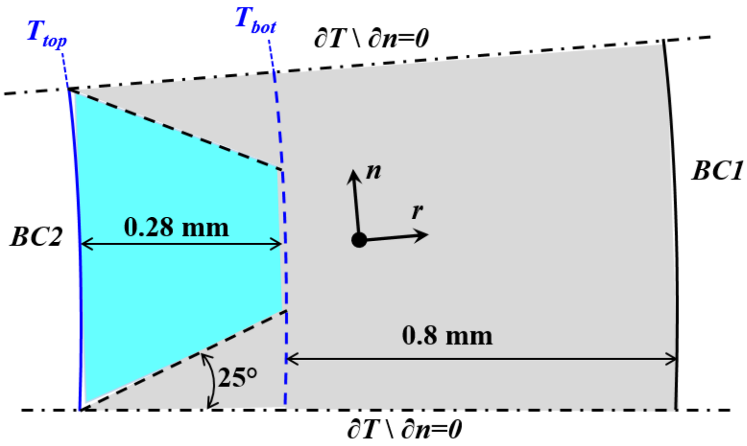

Figure 2.11 Pure heat conduction model to predict the effective thermal conductivity of the grooves.

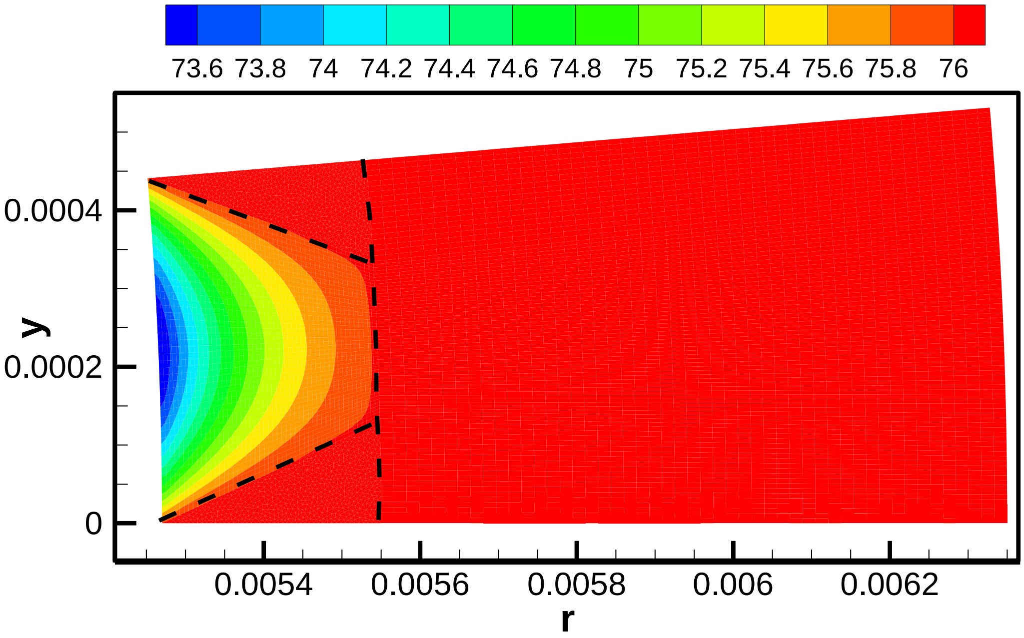

Figure 2.12 Temperature distribution showcase of model with BC1: $q = 10^4$ W/m^2 and BC2: $T_\infty = 50$ K, $h_\infty = 500$ W/(m^{2}K)

CHAPTER 3:
SOLUTION PROCEDUR

The solution procedure with all he numerical details based on the aforementioned governing equations and boundary conditions are presented in this section. The governing equations are discretized based on the finite volume method by Patankar [103] using the fully-implicit, axisymmetric, two dimensional, double precision ANSYS Fluent V16.0.0 package. Since the discretization and solution procedures are standard, only critical aspects of the procedure are presented here.

3.1 Computational Domains and Grid

As shown in Figure 2.2, three computation domains of *Wall*, *Wick* and *Vapor* are needed for the solver to model the two-dimensional axisymmetric cylindrical heat pipe. All the domains are made separately in Pointwise V17.1 and then put together with no gaps between the domains. Since there is two different velocities ($u_{r,V}$ and $u_{r,W}$) at the Wick-Vapor interface, two separate walls needed on which two different velocity boundary conditions could be applied. On the other hand, since the radiuses (r) of the cells are automatically their distances from the x-axis in two-dimensional axisymmetric ANSYS Fluent, there cannot be any gap between the domains and the walls of the domains have to overlap at their interfaces. Note, there is no “interior” boundary type in the present model and all the domains are fully enclosed with “wall” boundary type and in the case of Wick-Vapor interface, “velocity-inlet” boundary type are used to apply the in and out flow.

Rectangular grid is used to generate the mesh for all three domains. The cells have different sizes in different domain and even within one domain (*Wick* domain) however, the axial grid in all the domains are identical so the interface cells have identical contact area. The final mesh with all three domains and their grid is shown in Figure 3.1 (a), however, there cannot anything be seen since the radius (*r*) scale is much smaller than the axial length. In order to show the details of the domains and grid, all the dimensions in *r* direction are magnified 10 times, which is shown in Figure 3.1 (b). Nonetheless, the *Wall* and *Wick* domains are not clear yet, thus, all the dimensions in these two domain are magnified 10 time, again, as shown in Figure 3.1 (c). Also, the interfaces between the domains are shown with a dashed line in Figure 3.1 (c). In the grid depicted in Figure 3.1, 74 nodes are used axially (*Nx* = 74) and 20, 8 and 8 nodes are used radially (in *r* direction) for *Vapor* (*Nr* = 20), *Wick* (*Nr* = 8) and *Wall* (*Nr* = 8) domains respectively (*Nr* = [20, 8, 8], *Nx* = 74). Because of the geometry of the heat pipes, the domains inherently have very high aspect ratios (as listed in Table 3.1) which make it hard for the solver. Aspect ratios of the domain and the cells within the domains for the grid showcased above (*Nr* = [20, 8, 8], *Nx* =74) are listed in Table 3.1. In order to have small cell aspect ratio within the domains, many more nodes are needed in axial direction than the radial direction. Also, to keep the cell aspect ratios the same, many more nodes are needed in axial direction to compensate one node added to the radial direction. Hence, the number of grids in radial directions have to be chosen carefully to save CPU time with minimal damage to the accuracy of the results.

3.2 Discretization

All the time gradients are discretized fully-implicated meaning only one term is read through the previous time step and all other terms are calculated on the current time which helps the solution to be more stable. The diffusion terms are discretized based on central-difference method (Least Squares Cell-Based) however the convective terms are discretized based on upwind method (Second Order). The SIMPLE algorithm has been used to couple the velocity and pressure. A typical control volume with its neighbors are depicted in Figure 3.2 (a) to show the convective terms and the cell centers. Energy equation discretization for the Wick-Vapor interface (Eq. (2.21)) can be computed as:

$$T_{int} = \frac{\frac{k_{eff}}{\Delta r_w} T_w + \frac{k_v}{\Delta r_v} T_v + \dot{m}'' h_{fg}}{\frac{k_{eff}}{\Delta r_w} + \frac{k_v}{\Delta r_v}} \tag{3.1}$$

Where Δr_w and Δr_v are the distances from *Wick* and *Vapor* cell centers to the interface respectively, as illustrated in Figure 3.2 (b).

3.3 Stability Improvement

Because of the large value of latent heat, small changes in mass transfer can cause large changes in the interfacial temperature. Therefore, this procedure is not stable, especially for high heat fluxes [21, 31, 60, 61] and needs to be improved. This improvements are discussed in this section.

3.3.1 Improved System Pressure Formulation

In order to improve the stability of the solution, dependence of system pressure (P_{op}) on mass flux ($\dot{m}''$) is taken into account [21, 31, 60, 61]. Combining the Eq. (2.23) and Eq. (2.31), we have:

$$\dot{m}'' = \left(\frac{2\sigma}{2-\sigma}\right)\frac{1}{(2\pi R)^{1/2}}\left(\frac{\hat{P}+P_{op}}{(T_v)^{1/2}} - \frac{P_{int}}{(T_{int})^{1/2}}\right) \tag{3.2}$$

Then, including Eq. (3.2) into Eq. (2.33), we have:

$$P_{op} = \frac{M_v^0 + \Delta t\left(\sum_{W-V} - \left(\frac{2\sigma}{2-\sigma}\right)\frac{1}{(2\pi R)^{1/2}}\left(\frac{\hat{P}+P_{op}}{(T_v)^{1/2}} - \frac{P_{int}}{(T_{int})^{1/2}}\right)\Delta A\right)}{\frac{1}{R}\sum_V \frac{\Delta V}{T_v}} \tag{3.3}$$

By rearranging the Eq. (3.3), a new improved equation to calculate the system pressure (P_{op}) can be derived as follow:

$$P_{op} = \frac{M_v^0 - \Delta t\left(\sum_{W-V} \ \left(\frac{2\sigma}{2-\sigma}\right)\frac{\Delta A}{(2\pi R)^{1/2}}\left(\frac{\widehat{P_v}}{(T_v)^{1/2}} - \frac{P_{int}}{(T_{int})^{1/2}}\right)\right)}{\frac{1}{R}\sum_V \frac{\Delta V}{T_v} + \Delta t \sum_{W-V} \ \left(\frac{2\sigma}{2-\sigma}\right)\frac{\Delta A}{(2\pi R)^{1/2}}\left(\frac{1}{(T_v)^{1/2}}\right)} \tag{3.4}$$

The new equation [21, 31, 60, 61] has a new term added to the denominator which can help improve the stability of the solver.

3.3.2 Improved Interface Temperature Formulation

The huge value of latent heat (h_{fg}) in the nominator of the Eq. (3.1) may cause problems in high heat flux modeling since small changes in the mass flux ($\dot{m}''$) may end up having big changes to the interface temperature (T_{int}). The denominator of the Eq. (3.1) needs to be improved to help the stability of the solver by taking into account the dependence of mass flux on interface temperature. This improvement is done by linearization of the mass flux [21, 31, 60, 61] as explained in this section.

Rearranging and renaming Eq. (3.1), we have:

$$aT_{int} = b + \dot{m}'' h_{fg} \tag{3.5}$$

Identical terms can be added to both sides of the Eq. (3.5) to have:

$$aT_{int} + \alpha\, h_{fg} T_{int} = b + \dot{m}'' h_{fg} + \alpha\, h_{fg} T_{int} \tag{3.6}$$

Rearranging Eq. (3.6), we have:

$$T_{int} = \frac{b + \dot{m}'' h_{fg} + \alpha\, h_{fg} T_{int}^{*}}{a + \alpha\, h_{fg}} \tag{3.7}$$

Where starred (*) values represent prevailing values during the iterative process. No matter what the value of α is, the interface temperature value is not any different when the solution converged. However, if the value of α is computed appropriately, can help the solution to be stable with increasing the value of the denominator.

As introduced and used by Ref.s [21, 31, 60, 61], the mass flux at the interface can be linearized with respect to interface temperature as:

$$\dot{m}'' = \dot{m}''^{*} + \left(\frac{\partial \dot{m}''}{\partial T_{int}}\right)^{*} (T_{int} - T_{int}^{*}) \tag{3.8}$$

Where $\dot{m}''$ comes from Eq. (2.23). Assuming P_{int} is only dependent on T_{int}, we have:

$$\left(\frac{\partial \dot{m}''}{\partial T_{int}}\right)^{*} = -\left(\frac{2\sigma}{2-\sigma}\right) \frac{1}{(2\pi R)^{1/2}} \frac{1}{(T_{int}^{*})^{1/2}} \left(\left(\frac{\partial P_{int}}{\partial T_{int}}\right)^{*} - \left(\frac{P_{int}}{2T_{int}}\right)^{*}\right) \tag{3.9}$$

Using the Clausius-Clapeyron equation (Eq. (2.24)), the gradient of interface pressure with respect to interface temperature ($(\partial P_{int} \backslash \partial T_{int})^{*}$) can be calculated as:

$$\left(\frac{\partial P_{int}}{\partial T_{int}}\right)^{*} = \beta = \frac{P_{int}^{*} h_{fg}}{R {T_{int}^{*}}^{2}} \tag{3.10}$$

By rewording the Eq. (3.8), we have:

$$\dot{m}'' = \dot{m}''^{*} + \alpha\, (T_{int} - T_{int}^{*}) \tag{3.11}$$

By substituting Eq. (3.10) into Eq. (3.9) and based on Eq. (3.11) and Eq. (3.8), α can be written as follow:

$$\alpha = -\left(\frac{2\sigma}{2-\sigma}\right) \frac{1}{(2\pi R)^{1/2}} \frac{1}{\sqrt{T_i^{*}}} \left(\beta - \left(\frac{P_{int}}{2T_{int}}\right)^{*}\right) \tag{3.12}$$

After all, the interface temperature calculation (Eq. (3.1)) can be improved as:

$$T_{int} = \frac{\frac{k_{eff}}{\Delta r_w} T_w + \frac{k_v}{\Delta r_v} T_v + \dot{m}''^{*} h_{fg} + \alpha\, h_{fg} T_{int}^{*}}{\frac{k_{eff}}{\Delta r_w} + \frac{k_v}{\Delta r_v} + \alpha\, h_{fg}} \tag{3.13}$$

The new equation [21, 31, 60, 61] has a new term added to the denominator which can help improve the stability of the solver. However, small values of under-relaxation is still needed to help the convergence using this method.

A new formulation is suggested in this study which is easier to apply and does not involve any assumptions. The interface temperature can be rewritten by substituting Eq. (3.2) to Eq. (3.1) as:

$$T_{int} = \frac{\frac{k_{eff}}{\Delta r_w} T_w + \frac{k_v}{\Delta r_v} T_v + \left(\frac{2\sigma}{2-\sigma}\right) \frac{1}{(2\pi R)^{1/2}} \left(\frac{\hat{P} + P_{op}}{(T_v)^{1/2}} - \frac{P_{int}}{(T_{int})^{1/2}}\right) h_{fg}}{\frac{k_{eff}}{\Delta r_w} + \frac{k_v}{\Delta r_v}} \tag{3.14}$$

By rearranging, all the terms including interface temperature (T_{in}) can be moved to left side as:

$$\begin{aligned} &\left(\frac{k_{eff}}{\Delta r_w} + \frac{k_v}{\Delta r_v}\right) T_{int} + \left(\frac{2\sigma}{2-\sigma}\right) \frac{1}{(2\pi R)^{1/2}} \left(\frac{P_{int}}{(T_{int})^{1/2}}\right) h_{fg} \\ &\qquad = \frac{k_{eff}}{\Delta r_w} T_w + \frac{k_v}{\Delta r_v} T_v + \left(\frac{2\sigma}{2-\sigma}\right) \frac{1}{(2\pi R)^{1/2}} \left(\frac{\hat{P} + P_{op}}{(T_v)^{1/2}}\right) h_{fg} \end{aligned} \tag{3.15}$$

By multiplying the second term on the left hand side by interface temperature (T_{in}), we have:

$$\begin{aligned} &\left(\frac{k_{eff}}{\Delta r_w} + \frac{k_v}{\Delta r_v}\right) T_{int} + \left(\frac{2\sigma}{2-\sigma}\right) \frac{1}{(2\pi R)^{1/2}} \left(\frac{P_{int}}{T_{int}(T_{int})^{1/2}}\right) h_{fg} T_{int} \\ &\qquad = \frac{k_{eff}}{\Delta r_w} T_w + \frac{k_v}{\Delta r_v} T_v + \left(\frac{2\sigma}{2-\sigma}\right) \frac{1}{(2\pi R)^{1/2}} \left(\frac{\hat{P} + P_{op}}{(T_v)^{1/2}}\right) h_{fg} \end{aligned} \tag{3.16}$$

And finally, interface temperature (T_{in}) can be rewritten as:

$$T_{int} = \frac{\frac{k_{eff}}{\Delta r_w} T_w + \frac{k_v}{\Delta r_v} T_v + \left(\frac{2\sigma}{2-\sigma}\right) \frac{1}{(2\pi R)^{1/2}} \left(\frac{\hat{P} + P_{op}}{(T_v)^{1/2}}\right) h_{fg}}{\frac{k_{eff}}{\Delta r_w} + \frac{k_v}{\Delta r_v} + \left(\frac{2\sigma}{2-\sigma}\right) \frac{1}{(2\pi R)^{1/2}} \left(\frac{P_{int}}{T^*_{int}(T^*_{int})^{1/2}}\right) h_{fg}} \tag{3.17}$$

This new formulation is used in this study which helps the convergence and also is easier to apply.

3.3.3 Under-Relaxation Factor

Under-relaxation method was also applied to damp the sharp gradients and help the convergence. Based on experience with the model and the case study, different values of under-relaxation factors (*Ω*) were applied to the variables as listed in Table 3.2 to have a robust solver after all. The under-relaxation method on how it affects the variable calculation is illustrated as:

$$\mathrm{z} = \Omega \mathrm{z}^{p+1} + (1-\Omega)\mathrm{z}^{p} \tag{3.18}$$

Where *z* is the variable being computed. Superscript *p* and *p*+1 refer to current (predicted, current iteration) and previous (assigned, previous iteration) values of the variable during an iterative solution.

As seen in Table 3.2, relatively small under-relaxation factors are used for the Wick-Vapor interface temperature and mass flux since this is where the sharpest gradients and big changes happen.

3.4 User Define Scalars (UDSs)

ANSYS Fluent can solve the transport equation for an arbitrary, user-defined scalar (UDS) in the same way that it solves the transport equation for a scalar such as species mass fraction [149, 150]. Extra scalar transport equations may be needed in certain types of combustion applications or for example in plasma-enhanced surface reaction modeling.

ANSYS Fluent allows you to define additional scalar transport equations in your model in the User-Defined Scalars panel. All the energy equations (Eq. (2.8), Eq. (2.9), Eq. (2.10), Eq. (2.12), Eq. (2.13), Eq. (2.14), Eq. (2.16) and Eq. (2.21)) are defined as new transport equation and boundary conditions and solved instead of using the prepared temperature equation by ANSYS Fluent. The reasoning behind this and the details on how is explained in this section.

As previously mentioned, the computational domains are separate with their own walls. At the Wick-Vapor interface, the walls are defined as “velocity-inlet” boundary type where we can have flow in and out. However, the prepared temperature solver of the ANSYS Fluent does not listen to UDF commands assigning temperature to that part of boundary where the fluid is flowing out of domain, rather, the solver assigns its own computed values to that part of the boundary. This is crucially important in the model described in this study since the temperature of that boundary (interface temperature) is computed using the temperatures and velocities from the boundary cells from both domains of *Wick* and *Vapor* and then assign one interface temperature to both walls of the domains.

This problem is illustrated using a very simple test model as described in Figure 3.3. Assume a steady-state two dimensional laminar incompressible fluid flow and heat transfer problem in 1.5 m × 0.3 m rectangular domain with thermal and velocity boundary conditions described in Figure 3.3. This sample problem is solved with both UDS and prepared temperature to compare the results. The bottom wall is defined as a “velocity-inlet” boundary type and the velocity, temperature and UDS values are assigned using three *DEFINE_PROFILE* UDFs. The bottom wall has three different sections and the area of interest is the first 0.5 m of the bottom wall where the fluid (water) flow out of the domain.

The UDS and Temperature values are assigned using UDFs to be 330 K, 300 K and 270 K on the first, second and third 0.5 m sections of the bottom wall, respectively. Also, the fluid flows in through the third section of the bottom wall and flows out through the first section of bottom wall, once with an average inlet velocity of 10^{-5} m/s ($U_0 = 10^{-5}$ m/s) and once average inlet velocity of 10^{-6} m/s ($U_0 = 10^{-6}$ m/s). The top wall UDS and temperature values are set to be 400 K with no-slip boundary condition for the velocity. The side walls are adiabatic and have zero velocity in both directions. The solution of velocity, UDS and Temperature fields are totally separate and there is not coupling between them.

The test model is solved with ANSYS Fluent for both UDS and temperature with high degree of accuracy for two different velocity profile ($U_0 = 10^{-5}$ m/s and $U_0 = 10^{-6}$ m/s). The velocity distribution within the domain and on boundaries is showcased in Figure 3.4 (a). Note, the velocity field is not coupled with temperature, nor with UDS. The Temperature and UDS distributions are shown for $U_0 = 10^{-6}$ m/s in Figure 3.4 (b) and Figure 3.4 (c) respectively. It is obvious the results near the outlet are different, one can see the Temperature results (Figure 3.4 (b)) is not compatible with the boundary condition commanded with a UDF and the values on the first 0.5 m of the bottom wall are not 330 K. On the other hand, the UDS results (Figure 3.4 (c)) are shown compatibility with the assigned boundary conditions (330 K). As mentioned earlier in this section, the prepared temperature solver of the ANSYS Fluent does not listen to UDF commands assigning temperature to that part of boundary where the fluid is flowing out of domain, and that can be clearly seen in Figure 3.4 (b). The Temperature and UDS distributions are shown for $U_0 = 10^{-5}$ m/s in Figure 3.4 (d) and Figure 3.4 (e) respectively. In this case, the convective terms are larger than diffusive terms, however, the UDS results are still compatible with the boundary conditions assigned and the Temperature results are not. Note, the contour legend shown in Figure 3.4 (b) is fitting all the other contours shown in Figure 3.4.

Moreover, the Temperature and UDS profiles on the bottom wall are depicted in Figure 3.5 for two different velocity profiles ($U_0 = 10^{-5}$ m/s and $U_0 = 10^{-6}$ m/s) for a better comparison. As shown, the UDS results are identical to the applied boundary conditions for both cases of inlet velocities: the first, second and third (last) 0.5 m section have a value of 330 K, 300 K and the 270 K respectively. But the Temperature profiles have a different story as it is evident in Figure 3.5. The second and third (last) 0.5 m section of the bottom wall respectively have a value of 300 K and 270 K which is the correct values while the first 0.5 m section, where the fluid is flowing out, is far away from the value it should have had based on the boundary conditions. Note, for the second and third section of the bottom wall, all the lines are identical and overlapped and only one line is visible.

In this study, UDS is used instead of the temperature menu in ANSYS Fluent, as explained above, however, it brings its own challenges. All the terms in governing energy equations (Eq. (2.8), Eq. (2.9) and Eq. (2.10)) need to be reconsidered to be suitable for a UDS solver since the UDS solver does not understand the physics behind the variable (temperature here).

Dividing the energy equation for the *Wall* domain (Eq. (2.8)) by the $c_{p,s}$, the new equation for UDS solver is derived for the *Wall* domain as follow:

$$\rho_s \frac{\partial T}{\partial t} = \frac{k_s}{c_{p,s}} \left(\frac{1}{r} \frac{\partial}{\partial r} \left(r \frac{\partial T}{\partial r} \right) + \frac{\partial^2 T}{\partial x^2} \right) \tag{3.19}$$

Where $k_s / c_{p,s}$ is the diffusivity ($D_s = k_s / c_{p,s}$) for the *Wall* domain which is defined through the material properties used in *Wall* domain, which is copper. Dividing the energy equation for the *Wick* domain (Eq. (2.9)) by the $c_{p,l}$, the new equation for UDS solver is derived for the *Wick* domain as follow:

$$\left((1-\varphi)\frac{[\rho c_p]_s}{c_{p,l}}+\varphi\rho_l\right)\frac{\partial T}{\partial t}+\frac{1}{r}\frac{\partial}{\partial r}(\rho_l r u_r T)+\frac{\partial}{\partial x}(\rho_l u_x T) = \frac{k_{eff}}{c_{p,l}}\left(\frac{1}{r}\frac{\partial}{\partial r}\left(r\frac{\partial T}{\partial r}\right)+\frac{\partial^2 T}{\partial x^2}\right) \tag{3.20}$$

Where $k_{eff}/\, c_{p,l}$ is the diffusivity ($D_l = k_{eff}/\, c_{p,l}$) for the *Wick* domain which is defined through the material properties used in *Wick* domain, which is liquid water. Moreover, the transient term is not the same as the trainset term ANSYS Fluent automatically calculate for the UDS solver and needs to be recalculate thorough a *DEFINE_UDS_UNSTEADY UDF*.

Dividing the energy equation for the *Vapor* domain (Eq. (2.10)) by the $c_{p,v}$, the new equation for UDS solver is derived for the *Vapor* domain as follow:

$$\rho_v\frac{\partial T}{\partial t}+\frac{1}{r}\frac{\partial}{\partial r}(\rho_v r u_r T)+\frac{\partial}{\partial x}(\rho_v u_x T) = \frac{k_v}{c_{p,v}}\left(\frac{1}{r}\frac{\partial}{\partial r}\left(r\frac{\partial T}{\partial r}\right)+\frac{\partial^2 T}{\partial x^2}\right)+\emptyset \tag{3.21}$$

Where $k_v/\, c_{p,v}$ is the diffusivity ($D_v = k_{eff}/\, c_{p,l}$) for the *Vapor* domain which is defined through the material properties used in *Vapor* domain, which is vapor water.

Note, the UDS convective terms automatically calculated by ANSYS Fluent is compatible with the convective terms in Eq. (3.19), Eq. (3.20) and Eq. (3.21). As a matter of fact, the new forms of the energy equations are intentionally redefined in a way that there is no need to recalculate the convective terms.

3.5 User Define Functions (UDFs)

User Defined Functions (UDFs) allow the user to customize ANSYS Fluent and can significantly enhance its capabilities. A UDF is a routine (programmed by the user) written in C which can be dynamically linked with the solver. It is a combination of Standard C functions such as: trigonometric, exponential, control blocks, do-loops, files inputs and outputs, etc; And Pre-Defined Macros which Allow access to field variable, material property, and cell geometry data. The standard interface of ANSYS Fluent cannot be programmed to anticipate all needs such as: customization of boundary conditions, source terms, reaction rates, material properties, adjust functions (once per iteration), Execute on Demand functions, solution initialization etc [151].

Since the presented numerical solution of heat pipes involves variables and parameters from both system level and standard level as well as from different computational domains, it is impossible without UDFs to perform such a numerical simulation. All the UDFs used in this study are listed in Table 3.3 with their type and names. In this section, these UDFs and their roles are explained briefly.

3.5.1 Initial UDFs

“DEFINE_INIT” type UDFs are the first UDF called before the solver is started, before any other UDFs however, after “Declarations” is loaded. Two “DEFINE_INIT” type UDFs are used in this study which are mentioned in this section along with what they do.

- *INITIAL_SETTINGS*

All the parameters used in the simulation are set in this UDF such as: heat flux, heat transfer coefficient, reference temperature and pressure, latent heat, porosity, effective conductivity, under relaxation factor, operation pressure etc. Also, the UDS and interface variables are initialize in this UDF. Moreover, the volume of wick and vapor domains, the mass of wick and vapor domains are set and initialize in this UDF.

- *SHADOW_READING*

As mentioned earlier, the domains are made separately and do not have any connection. Now imagine the pointer is on a cell on a boundary of a domain (boundary#1, Figure 3.6) and information from the neighbor cell from the other domain (boundary#2, Figure 3.6) is needed. ANSYS Fluent does not have any predefined macro to access the neighbor cell in neighbor domains, therefore, one has to loop through all the cells within the neighboring boundary (boundary#2, Figure 3.6) and compare a geometry parameter (x in this case) to find the neighboring cell on the main boundary (boundary#1, Figure 3.6).

This procedure has to be repeated for all the cells on the boundary from the first domain (loop in loop) and for all other interface boundaries in all the domains. This would take a lot processing time if repeated for each iteration and each time step. In this UDF, at the initial stage before the solution is started, for once this process of finding neighbor cells is done and the faces and threats of neighbor cells are saved in arrays that can be called and used later in the rest of solver without any loop which saves CPU time.

3.5.2 Define Adjust UDFs

“DEFINE_ADJUST” type UDFs are called at the beginning of each iteration. Two “DEFINE_ADJUST” type UDFs are used in this study which are mentioned in this section along with what they do.

- *PARAMETERS_UPDATE*

Pressure operation (Eq. (3.4)) is updated every iteration in this UDF based on information from the vapor domain and liquid-wick interface. Also, based on the mass transfer balance (Eq. (2.28)) at the liquid-vapor interface, the mass of vapor (Eq. (2.29)) and mas of wick (Eq. (2.30)) domain is updated every iteration.

- *WICK_VAPOR_INTERFACE*

In this UDF, the interface temperature (Eq. (3.17)), interface mass transfer (Eq. (3.2)), and as well as the interface velocities at the wick (Eq. (2.18)) and interface velocities at the vapor (Eq. (2.19)) domains. Note, the interface temperature and velocities are only calculated here in this UDF and they are applied in other UDFs.

3.5.3 Define Profile UDS

"DEFINE_PROFILE" type UDFs could be used at any part of the solver such: defining a boundray condition, defninting a properties or any other customized profiles not provided by ANSYS Fluent. All the "DEFINE_PROFILE" type UDFs are used in this study which are mentioned in this section along with what they do

- *VELOCITY_VAPOR_WICK*

This UDF assigns the velocity boundary values, already calculated in "DEFINE_ADJUST, WICK_VAPOR_INTERFACE," to the vapor-wick interface boundary but at the vapor side.

- *VELOCITY_WICK_VAPOR*

This UDF assigns the velocity boundary values, already calculated in "DEFINE_ADJUST (WICK_VAPOR_INTERFACE)," to the vapor-wick interface boundary but at the wick side.

- *TEMPERATURE_VAPOR_WICK*

This UDF assigns the temperature boundary values, already calculated in "DEFINE_ADJUST, WICK_VAPOR_INTERFACE," to the vapor-wick interface boundary but at the vapor side.

- *TEMPERATURE_WICK_VAPOR*

This UDF assigns the temperature boundary values, already calculated in "DEFINE_ADJUST, WICK_VAPOR_INTERFACE," to the vapor-wick interface boundary but at the wick side.

- *TEMPERATURE_WICK_WALL*

This UDF calculates and assigns the temperature boundary values based on Eq. (2.16) to the wick-wall interface boundary but at the wick side

- *TEMPERATURE_WALL_WICK*

This UDF calculates and assigns the temperature boundary values based on Eq. (2.16) to the wick-wall interface boundary but at the wall side

- *TEMPERATURE_COOLING*

This UDF calculates and assigns the temperature boundary values based on Eq. (2.14) to the boundary of condensation s.

- *WALL_HEAT_FLUX*

This UDF assigns the temperature boundary values based on Eq. (2.12) to the boundary of condensation section.

- *VAPOR_DENSITY*

This UDF calculates and assigns the local density of vapor based on Eq. (2.34).

- *LIQUID_DENSITY*

This UDF calculates and assigns the density of wick based on Eq. (2.35).

- *WICK_CONDUCTIVITY*

This UDF assigns the effective thermal conductivity of the wick domain based on the location of pointer, whether it is in groove or screen mesh area.

- *WICK_POROSITY*

This UDF assigns the porosity of the wick domain based on the location of pointer, whether it is in groove or screen mesh area.

- *VISCOUS_RESISTANCE*

This UDF assigns the porous media viscous resistance of the wick domain based on the location of pointer, whether it is in groove or screen mesh area.

- *INERTIAL_RESISTANCE*

This UDF assigns the porous media inertial resistance of the wick domain based on the location of pointer, whether it is in groove or screen mesh area.

3.5.6 Other UDFs

There are other types of UDFs used in this study as listed and explained in this section.

- Declarations

This part is used to declare all the public variables and once declared in this part, would be accessible in all other UDFs. Despite local variables, any variable defined in this section is global. All the faces, threads, domains, integer variable, real variables and arrays are defined in this section. When ANSYS Fluent loads the C file, declares all the variables in this section. This section of the UDFs is the only section called before "DEFINE_INIT" type UDFs.

- *DEFINE_UDS_UNSTEADY: UDS_UNSTEADY_REVISION*

As explained earlier, the transient term normally calculated by ANSYS Fluent for the UDS transport equation has to be modified in the wick region because of the porous media. This UDF calculates and assigns the unsteady terms based on Eq. (3.20), Eq. (3.21) and Eq. (3.19).

- *DEFINE_DIFFUSIVITY: WICK_DIFFUSIVITY*

This UDF assigns the diffusivity of the wick domain based on the location of pointer, whether it is in groove or screen mesh area.

- *DEFINE_DELTAT: TIME_STEP*

This UDF is in charge of dynamic time step. Each time step value is calculated and assign in this section.

3.6 Overall Solution Algorithm

The overall solution algorithm along with all the UDFs and where they stand during this numerical procedure are illustrated in Figure 3.7.

Table 3.1 Domain and cell aspect ratios for the *Nr* =[20, 8, 8], *Nx* =74 grid.

Domains	Aspect Ratios	
	Domain	Cell
Wall	≈ 463	≈ 50
Wick	≈ 768	≈ 83
Vapor	≈ 73	≈ 20

Table 3.2 List of under-relaxation factors applied to different variables

Equation	Ω
Pressure	0.3-0.5
Momentum	0.5-0.7
Energy	0.8-0.9
Source terms	0.8
Density	0.8
System pressure	1.0
Wick-Vapor interface temperature	0.3-0.1
Wick-Vapor interface mass flux	0.3-0.1

Table 3.3 List of types and names of the UDFs used in this study

Type and Name	
DEFINE_PROFILE:	**DEFINE_INIT**:
VELOCITY_VAPOR_WICK	INITIAL_SETTINGS
VELOCITY_WICK_VAPOR	SHADOW_READING
WICK_POROSITY	**DEFINE_ADJUST**:
VISCOUS_RESISTANCE	PARAMETERS_UPDATE
INERTIAL_RESISTANCE	WICK_VAPOR_INTERFACE
WALL_HEAT_FLUX	**DEFINE_EXECUTE_AT_END**:
TEMPERATURE_COOLING	TRANSIENT
VAPOR_DENSITY	WICK_VAPOR_INTERFACE_PRINTOUT
LIQUID_DENSITY	WICK_VAPOR_DOMAINS_PRINTOUT
WICK_CONDUCTIVITY	WALL_PRINTOUT
TEMPERATURE_VAPOR_WICK	**DEFINE_UDS_UNSTEADY**:
	UDS_UNSTEADY_REVISION
TEMPERATURE_WICK_VAPOR	**DEFINE_DIFFUSIVITY**:
	WICK_DIFFUSIVITY
TEMPERATURE_WICK_WALL	**DEFINE_DELTAT**: TIME_STEP
TEMPERATURE_WALL_WICK	**Declarations**: No Name

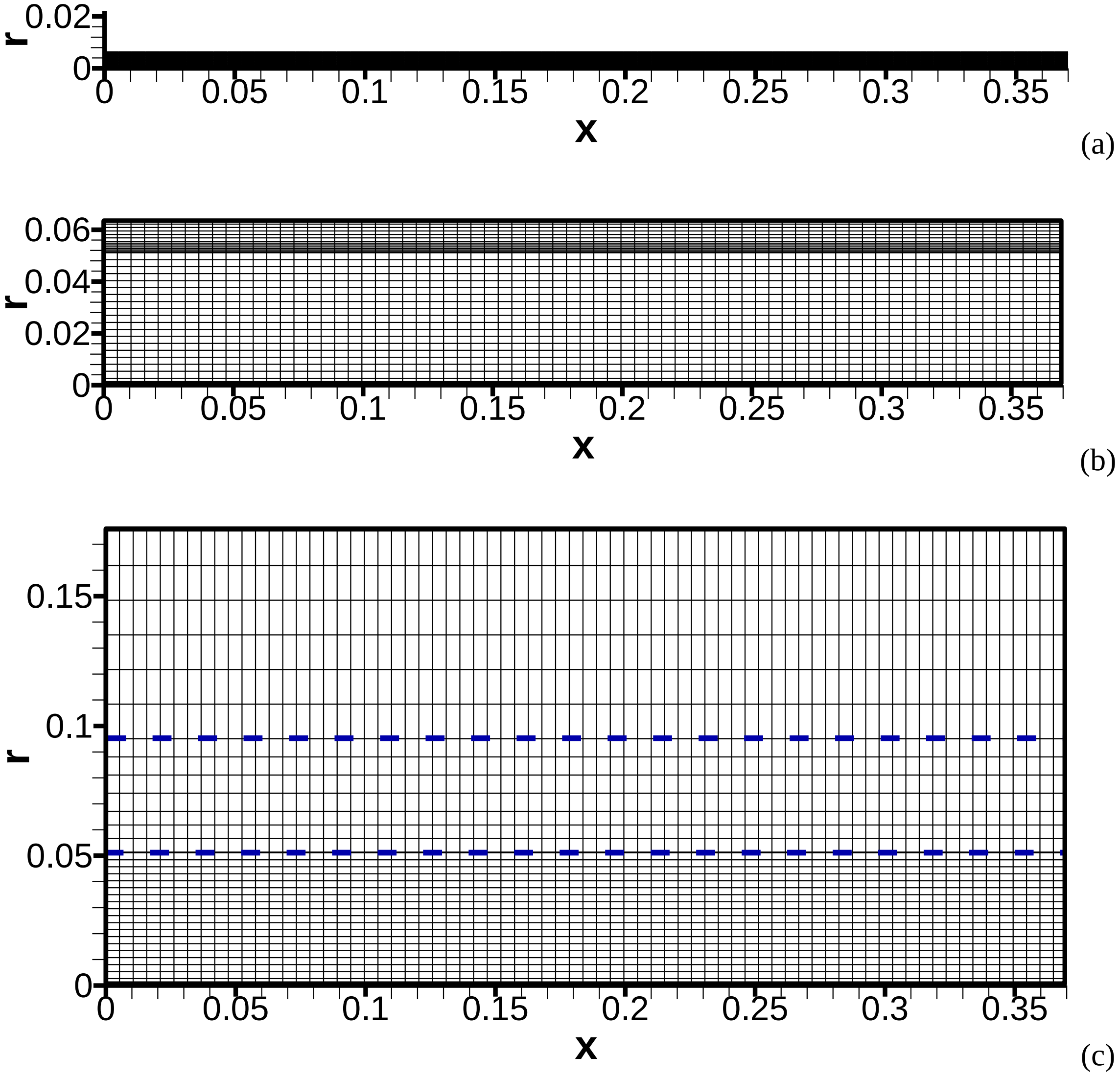

Figure 3.1 Three computational domains with their grid (a) actual dimensions (b) dimensions in r direction are magnified 10 times (c) dimensions in r direction in the Vapor domain are magnified 10 times and in the Wick and Wall domains 100 times.

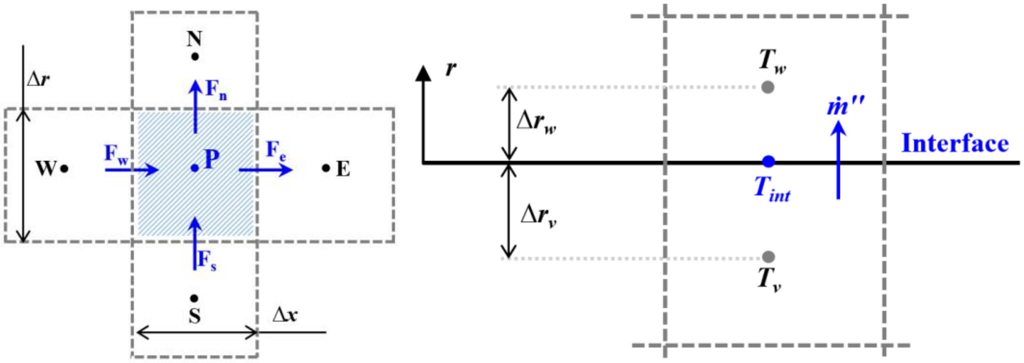

(a) (b)

Figure 3.2 (a) A typical control volume with its neighbors (b) A typical control volumes from Wick and Vapor domain at their interface

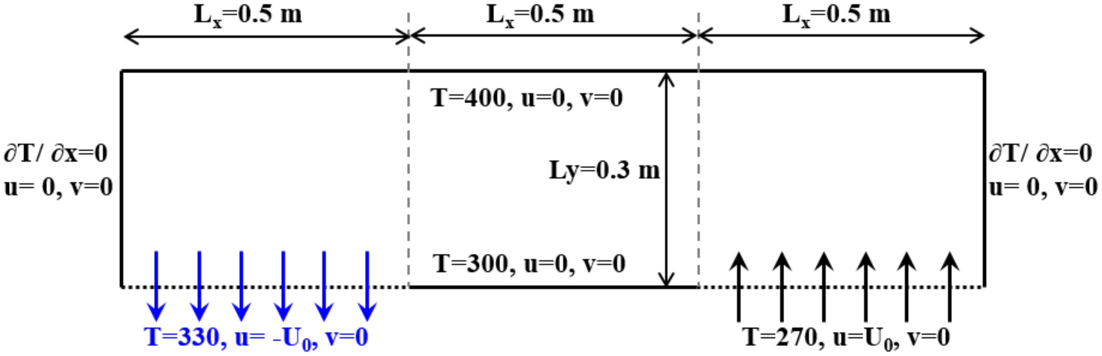

Figure 3.3 A steady-state two dimensional laminar incompressible test model to compare UDS vs. Temperature at the outflow boundray.

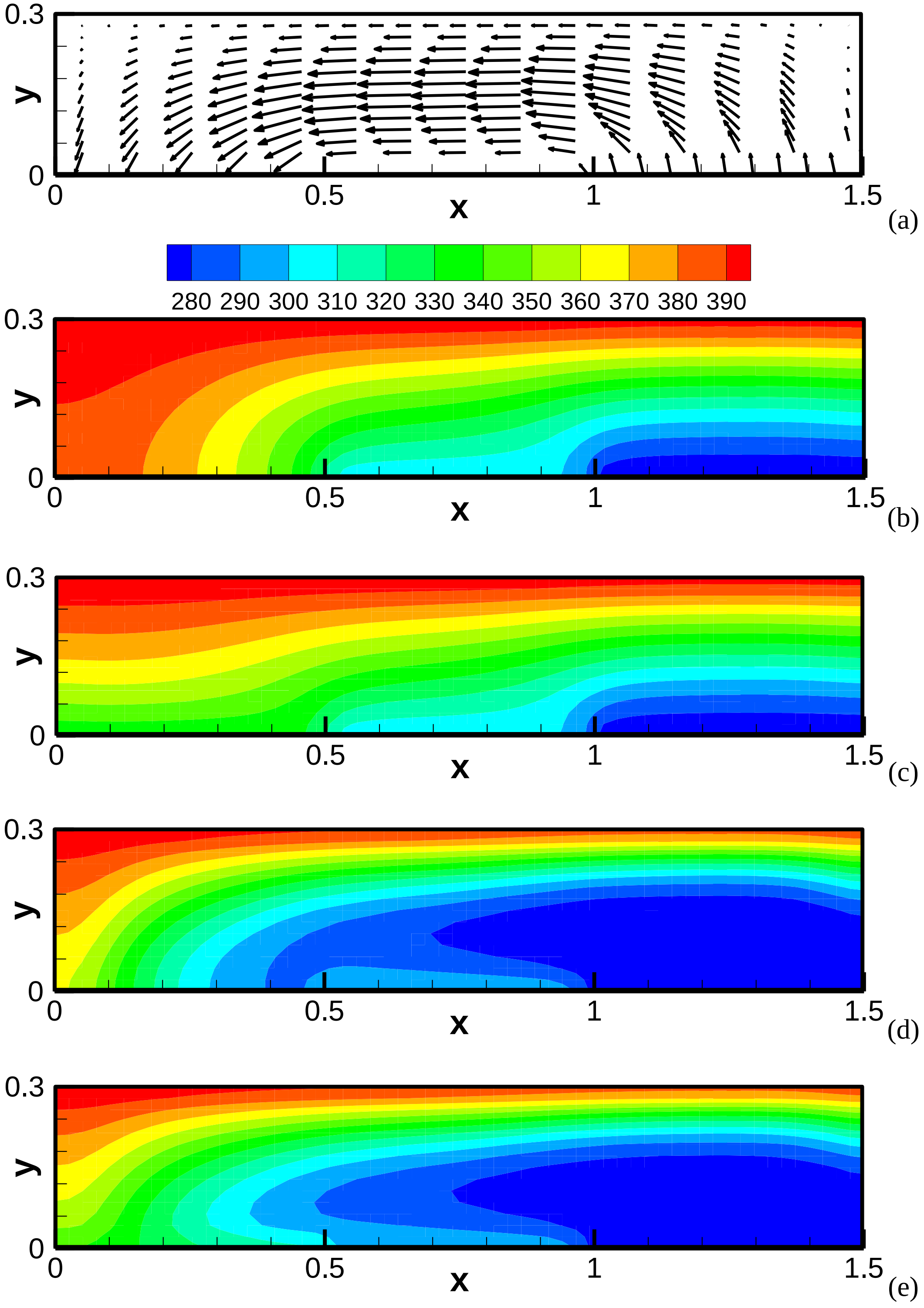

Figure 3.4 Test model to compare the UDS vs. Temperature Results (a) velocity distribution (b) Temperature distribution with $U_0 = 10^{-6}$, (c) UDS distribution with $U_0 = 10^{-6}$, (d) Temperature distribution with $U_0 = 10^{-5}$ (e) UDS distribution with $U_0 = 10^{-5}$

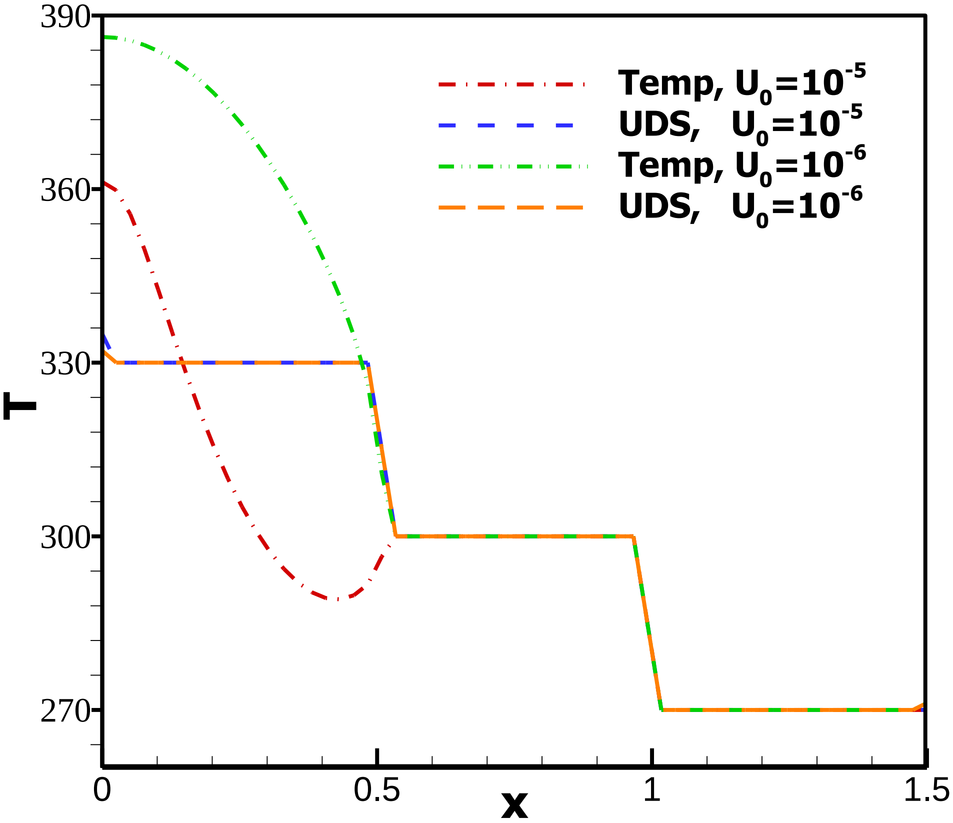

Figure 3.5 Bottom wall Temperature and UDS profiles for different inlet velocities.

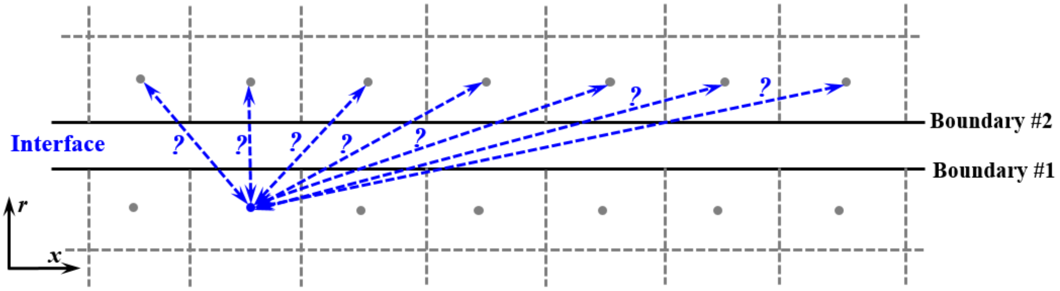

Figure 3.6 Finding neighboring cells on boundaries at the interface from different domains

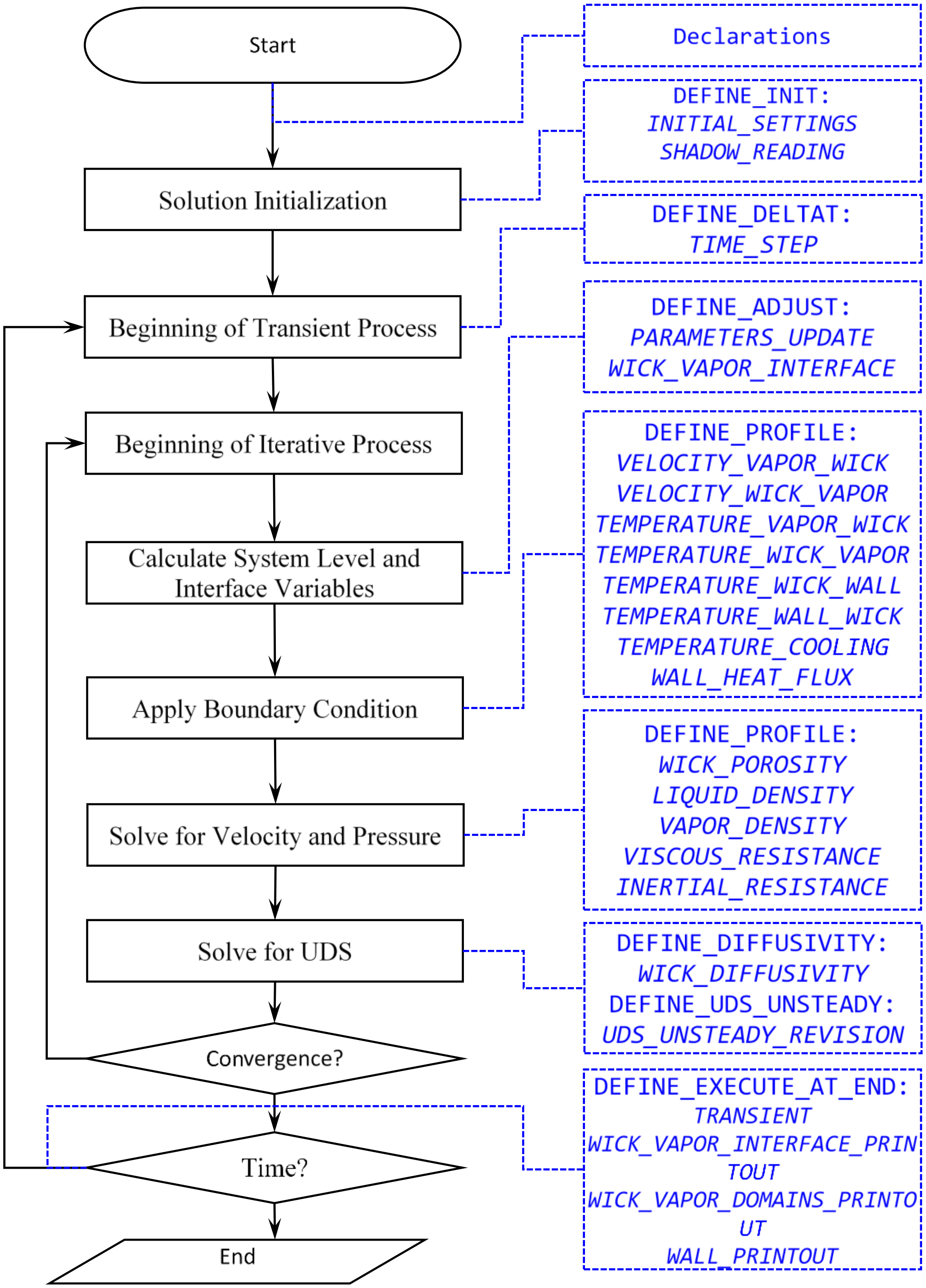

Figure 3.7 Overall Solution Algorithm

CHAPTER 4:
RESULTS AND DISCUSSION

The models, numerical method and procedure described in previous chapters are used to carry out simulation of cylindrical heat pipes with hybrid wick structure. First, the devised methodology are tested with different time steps, different computational grids. Second, it is validated against existing experimental and numerical flat and cylindrical heat pipes publications. Also, the results of the present method are compared with the corresponding experimental results. Third, the transient and steady-state performance of cylindrical heat pipe are presented. And forth, a comprehensive parameter study is accomplished using the proposed numerical scheme.

4.1 Grid and Time Step Independency

In order to see the consistency of the proposed scheme and also find the optimum time step and computational grid, the described cylindrical heat pipe is solved using the proposed numerical method and the results are presented in this section.

4.1.1 Time Step Independency

The fully hybrid cylindrical heat pipe with the highest heat input (Q =150 W) is chosen for this part as an intense example to show the differences in the results, if any. The mechanical, thermal, viscous, porous media and phase change parameters needed for the present numerical simulation is listed in Table 4.1 while the cooling boundary conditions are previously mentioned in Table 2.2 and while the initial conditions are as Eq.s (2.36)-(2.39). The proposed method is tested with 4 different time steps of 0.001 s, 0.01 s, 0.1 s and 1.0 s and the results are shown in Figure 4.1. The system pressure and maximum wall temperature is depicted vs. time in Figure 4.1 (a) and Figure 4.1 (b) respectively. The results agree very well for all the time steps as the largest difference for maximum wall temperature is 0.15% between the cases with 0.001s and 1s while the largest difference for the operating pressure is 1.46% between the cases with 0.001s and 1s. The liquid-vapor interface mass transfer balance at the interface vs. time is shown in Figure 4.1 (c) for different time steps and the results seem to have a good agreements. However, there are different trends among the cases with 1.0 s, 0.1 s and 0.01 s, if focused to the first 10 seconds of the figure which is highlighted in Figure 4.1 (d). The obvious reason is that the cases with 1.0 s and 0.1 s cannot capture the details of what happens in the first 1 second. In order to handle this, dynamic time steps ranging from 0.001 s to 1.0 s is proposed and tested and results are depicted along with the other cases in Figure 4.1 (d). As shown, the dynamic time step case agrees well with small time steps cases and maximum difference of 3.38% is reported. The dynamic time steps designed in way that the solution is started with 0.001 s and increases 1.2 times each time step until it reaches the cap of 1.0 s.

Moreover, the maximum velocity in the vapor core is depicted vs. time in Figure 4.2 (a). As shown, all the cases expect the 1.0 s case have reasonably good agreement and while maximum difference of 2.12% is reported between dynamic time step case and 0.001 s case. Also, another comparison is made among the cases with different time steps but this time, the wall temperature of heat pipe for 3 different times of 1 s, 5 s and 15 s. Once again, the results from the case with 1.0 s is slightly different from the rest while there are only 0.05%, 0.09% and 0.13% differences between dynamic time steps and 0.001 s cases reported for wall temperature distributions after 1 s, 5 s and 15 s, respectively.

The dynamic time steps (Δt = 0.001 s – 1.0 s) method are selected in this study to perform the rest of numerical simulations with since its results agree very well with the corresponding results from the smallest time steps case (Δt = 0.001 s) while the CPU time for the dynamic time steps case (≈ 1 day) is much less than the CPU time for the smallest time steps case (≈ 3 days).

4.1.2 Grid Independency

The groove cylindrical heat pipe with the highest heat input (Q =150 W) is chosen for this part as an intense example to show the differences in the results, if any. The proposed method is tested with 6 different computational grid sizes, as listed in Table 4.2 with their names and sizes. The system pressure and maximum wall temperature is depicted vs. time in Figure 4.3 (a) and Figure 4.3 (b), respectively. As illustrated, changing the grid sizes, even 16 times finer, did not change the outcome significantly as the maximum differences of 1.6% and 0.01% are reported for system pressure and maximum wall temperature, respectively. The transient maximum axial velocity and liquid-vapor interface mass transfer balance are shown in Figure 4.3 (c) and Figure 4.3 (d), respectively. As shown, moving to a 16 times finer computational grid did not result in any significant changes to the outcome as the maximum differences of 0.25% and 0.26% are reported for maximum axial velocity and liquid-vapor interface mass transfer balance, respectively. The wall temperature distribution of groove cylindrical heat pipe (Q =150 W) after 5 seconds (*time* = 5 s) for different grid sizes (listed in Table 4.2) are shown in Figure 4.4. The results from very fine and coarse gird sizes agree well in way that the maximum difference is reported to be 0.06%. The coarsest grid (Nr =[20, 8, 8], Nx =74) is chosen to perform the rest of numerical simulations with since its results agree very well with the corresponding results from the finest grid (*Nr* =[80, 32, 32], *Nx* =296) while the coarsest grid CPU time (≈ 1 day) is much less than the CPU time for the finest grid case (≈ 36 days).

4.2 Validation

In the previous section, the consistency of the present numerical procedure is examined however, it is not enough as one can be consistent but in a wrong direction. To further investigate the validity of the presented model, cylindrical and flat heat pipes available in the literature are modeled with the present model and the results are presented in this section.

4.2.1 Cylindrical

The cylindrical heat pipe studied numerically and experimentally by Faghri and Buchko [49] is used as a benchmark by most studies on cylindrical heat pipes. Their heat pipe is also chosen here to validate the present model. As shown in Figure 4.5, their heat pipe had multiple heat sources to have different combinations however, only two combinations (single heater, four heaters) of heat input are modeled here. The details of geometry can be found in Ref. [49] while other mechanical, vicious, thermal and porous media parameters are listed in Table 4.3. Since there is no information about the cooling boundary conditions in Ref. [49], two cases of cooling boundary conditions are tested, one with an average cooling temperature based on the numerical results (Case 1) and one based on the experimental results (Case 2) presented in Ref. [49]. Moreover, the effective conductivity of the screen mesh was predicted to be 1.2 W/m.K (Case 1), however, another value of 1.7 W/m.K (Case 2) is simulated as well. All the cases simulated here and their differences are highlighted in Table 4.4. Moreover, it is unknown what the initial conditions were since only the steady-state results were presented in Ref. [49]. Therefore, first, three different initial temperatures (T_0 = 10 °C, 30 °C and 50 °C), with their corresponding saturation pressures and masses of vapor, are numerically computed for both single heater and four heaters and the results are presented in Figure 4.6 and Figure 4.7. Transient results of operation pressure are depicted in Figure 4.6 (a) and Figure 4.6 (b) for single heater and four heaters, respectively. Although the starting operating pressures are significantly different for different initial temperatures, they get closer as they reach steady-state in way that the steady-state operating pressures are only 3.10% and 9.45% different in the cases of single heater and four heaters, respectively. The difference between operating pressures are due to the fact that during evaporation and condensation, the mass of vapor also changes deepening on mass transfer balance at the liquid-vapor interface, therefore, operating pressure also changes as a function of the mass in the vapor core. Transient maximum and minimum wall temperatures of the modeled heat pipe are compared in Figure 4.7 for single heater and four heaters cases based on different initial conditions. As shown, the steady-state results are not dependent of the initial conditions, as the steady-state temperature differences are 0.02%-0.03% and 0.00% for single heater and four heaters cases, respectively. Now that it is shown the unknown initial conditions do not affect the steady-state results, comparisons can be made between the presented model and the Faghri and Buchko [49] and Vadakkan [21], as depicted in Figure 4.8. Two different cases are modeled as illustrated in Table 4.4, using the parameters listed in Table 4.3, and the steady-state wall temperatures of the present model are compared with the existing works in the case of single heather (Figure 4.8 (a)) and four heathers (Figure 4.8 (b)). Both Ref.s [21, 49] set the effective thermal conductivity of the wick to be 1.2 W/m.K which is named Case 1 here. The average cooling wall temperature is assumed to be around

73.3 °C and 65.2 °C by Ref.s [21] based on the numerical results of Ref. [49] in the case of single heater and four heaters, respectively, which again, is included in Case 1 here. The results from Case 1 in both cases of single heater and four heaters agrees well with the corresponding numerical results from Ref.s [21, 49]. However, the results from Case 2 in both cases of single heater and four heaters are closer to the corresponding experimental results which is due to the small change of the effective thermal conductivity from 1.2 W/m.K to 1.7 W/m.K. It is meant to show that present numerical model could predict a better set of results if the predicated parameters, effective thermal conductivity for instance, were more accurate and closer to the real experiment.

4.2.2 Flat Heat Pipe

The heat pipe studied numerically by Vadakkan [21] is chosen here to validate the present model. As shown in Figure 4.9, the heat pipe had wall, wick, vapor core and another wall where heating and cooling sections are applied on one wall and the other wall is considered adiabatic. The details of geometry can be found in Ref. [49] while other mechanical, vicious, thermal and porous media parameters are listed in Table 4.5. The flat heat pipe is solved for two different heat inputs of 10 W and 30 W as listed in Table 4.6 with the corresponding cooling boundary conditions. The wall temperature distributions after 20 s and 60 s are depicted in Figure 4.10 (a) and Figure 4.10 (b) for heat input of 10 W and 30 W, respectively. As shown, the numerical results of present numerical method agrees very well with the corresponding results of Ref. [49] in way that the maximum temperature differences are 0.13% and 0.09 % for 10 W and 30 W heat inputs, respectively. Heat output and wall temperature of evaporation center are depicted vs. time for different heat input and shown in Figure 4.11 (a) and Figure 4.11 (b), respectively. The results from the present study matches the corresponding results of Ref. [49] as the maximum differences of 1.45% and 0.04% are reported for output heat and evaporation center wall temperature, respectively. Liquid and vapor pressure drop as well as operating pressure are presented in Figure 4.12 (a) and Figure 4.12 (b), respectively. Pressure drops along the wick and vapor for 30 W case are shown in Figure 4.12 (a) after 20 s, 40 s and 60 s where pressure drops along the wick agree well with the corresponding results from Ref. [49] where the maximum difference of only 1.75% is reported. However, the pressure drop along the vapor core of the present method is 25% different than those of Ref. [49]. Transient pressure operation of heat pipe for heat input of 10 W and 30 W are compared with the pressure operation of 30 W from Ref. [49] and as shown in Figure 4.12 (b), no agreement is found. The operating pressure from Ref. [49] is not even close to the results of the present method based on Q=30 W, nor Q=10 W, rather it seems an incorrect case is reported by mistake. Also, the starting pint of operating pressure is he very corresponding saturation pressure at initial temperature, which is 1743 Pa for this case. However, based on the results from Ref. [49], it is obvious that the operating pressure is started in a value significantly less than 1743 Pa. Also, same trend of incorrect starting operation pressure (≈1470 Pa instead of 1585 Pa) can be found in Ref. [31].

4.2.3 Experiments

In this section, the numerical results of the present method are compared with the results from ongoing experiments in Micro/nanoscale Transport Lab at the University of South Carolina. The wall temperature distributions for groove heat pipe are compared with the corresponding experimental results in Figure 4.13. The numerical results agree very well with the experimental results for low heat input however, the numerical results start to deviate when the heat input increases in way that maximum temperature error of 8% can be seen for Q =150 W. The wall temperature distributions for fully hybrid heat pipe are compared with the corresponding experimental results in Figure 4.14. The numerical results show an over prediction of heat pipe for this case as the temperature differences can go up to 23%. The wall temperature distributions for fully hybrid heat pipe are compared with the corresponding experimental results in Figure 4.15. The numerical results show a fair prediction of heat pipe for this case as the maximum temperature differences can be 10%. Note, there are several factors which could make this deviation happen such as: the heat pipe fabrication process were not quite successful, the micro-scale effects are not included in this work, the thermal and viscous properties are not accurately predicted.

4.3 Transient and Steady-State Results

The mechanical, thermal, viscous, porous media and phase change parameters needed for the present numerical simulation is listed in Table 4.1 while the cooling boundary conditions are previously mentioned in Table 2.2 and while the initial conditions are as Eq.s (2.36) - (2.39). The grid size and time steps are chosen the way explained earlier in this chapter. The cylindrical heat pipe with grooves, fully hybrid and partially hybrid wick structure are investigated and the results are presented transient and steady-state sections here. In order to summarize these section, not all the results of different heat inputs, different wick structures and different times are not shown unless there were a need to include them.

4.3.1 Transient

Temperature contours of groove (Figure 4.16 (a, c and e)) and hybrid (Figure 4.16 (b, d and f)) heat pipes are shown in Figure 4.16 for t =1.856 s (Figure 4.16 (a and b)), *t*=5.66 s (Figure 4.16 (c and d)) and *t* =75.66 s (Figure 4.16 (e and f)) for the *Q* =150 W case. As explained earlier and shown in Figure 3.1, in order to show the details of the results in the domains, dimensions in r direction in the Vapor domain are magnified 10 times and in the Wick and Wall domains 100 times. The dashed lines are the wall-wick and wick-vapor interfaces, as depicted in Figure 4.16. As shown in Figure 4.16, the temperature gradients happen in the wick region while the temperature gradients are much relatively smaller. Also, as time goes by, the minimum and maximum temperatures increase as well as the difference between them. Moreover, in the wall domain, temperature is remained uniform within the heating and cooling sections as well as in radial direction. The results of partially hybrid cases also follow the same trends as the presented results.

Vapor core temperature contours of groove (Figure 4.17 (a, c and e)) and hybrid (Figure 4.17 (b, d and f)) heat pipes are shown in Figure 4.17 for *t* =1.856 s (Figure 4.17 (a and b)), *t*=5.66 s (Figure 4.17 (c and d)) and *t* =75.66 s (Figure 4.17 (e and f)) for the *Q* =150 W case. As shown, despite many previous works assuming constant temperature at the vapor core, the temperature changes radially and axially and the convective terms play major role in the heat transfer within the vapor core. Also, the maximum temperatures difference in the vapor core decreases with time meaning the temperature difference is minimum at steady-state conditions. The results of partially hybrid cases also follow the same trends as the presented results.

The wall (outside) temperature distributions of partially hybrid cylindrical heat pipe at different times are depicted for *Q* =30 W (Figure 4.18 (a)) and *Q* =150 W (Figure 4.18 (b)). As illustrated, the temperature distribution is uniform at the heating and cooling sections and even part of the adiabatic section at all the heat inputs and times. Also, comparing the *t* =5.66 s and *t* =75.66 cases as time goes by, the temperature differences between the two cases is much bigger than the maximum temperature difference at each time meaning the heat pipe loop is well established and the cooling section can see the heat transferred from heating sections in less than 5 seconds. The results of groove and hybrid cases also follow the same trends as the presented results.

The maximum and minimum wall temperatures versus time are depicted in Figure 4.19 for a fully hybrid cylindrical heat pipe with different heat inputs. The temperatures has a quick rise at the beginning and smoothly reaches the steady-state temperature. Same trends can be seen for both maximum and minimum wall temperature however, the minimum temperature follows with a little delay behind. In order to quantify this, time constants for minimum and maximum wall temperature are calculated based on the time needed to reach the 63.2% of steady-state corresponding values and listed in Table 4.7. As illustrated, the minimum wall temperature is only 2-3 seconds behind the maximum temperature.

Velocity vectors and contours of absolute velocity for groove (Figure 4.20 (a, c and e)) and fully hybrid (Figure 4.20 (b, d and f)) heat pipe are shown for *t* =1.856 s (Figure 4.20 (a and b)), *t*=5.66 s (Figure 4.20 (c and d)) and *t* =75.66 s (Figure 4.20 (e and f)) for the *Q* =150 W case. Note, the radial dimensions in wick and vapor regions is are 100 and 10 times magnified respectively, as mentioned previously. The radial components of the velocity in wick and vapor regions are also 100 and 10 times magnified, respectively. However, the absolute velocity values are the same as originally calculated. Moreover, the velocities in wick region are magnified 1000 and 2000 times for groove and fully hybrid heat pipes, respectively. The heat pipe circulation loop is illustrated in Figure 4.20 with velocity. The maximum velocity happen in the vapor core and at the axisymmetric line for all the case however, the location of this maximum value move away from heating side of heat pipe toward the middle of heat pipe (somewhere between heating and cooling side) as time goes by. Same trends can be found the maximum velocity in the wick for all the case. Also, the maximum velocity in the vapor domain decreases with time. Moreover, comparing Figure 4.20 (e and f), it can be noticed that the maximum velocity in the wick is moved toward the top of wick in the hybrid case and that is because the permeability of the screen mesh is less than the grooves and the liquid tends to flow through the grooves more.

To further investigate this, axial velocity profiles at wick region (at x =0.16 m) for fully hybrid (Figure 4.21 (b and d)) and groove (Figure 4.21 (a and c)) heat pipes for different heat inputs of Q = 30 W (Figure 4.21 (a and b)) and Q =150 W (Figure 4.21 (c and d)). The velocity profiles in both heat inputs are parabolic in the groove heat pipe, as reported in all the heat pipe simulation. However, the velocity profiles at the fully hybrid heat pipes have a different profiles and that is due to the existence of screen mesh with a lower permeability value. This research is the first work to report such a velocity profile since an accurate simulation of hybrid wicks does not currently exist.

The maximum axial velocity of liquid for groove heat pipe (Figure 4.22 (a)) and maximum axial velocity of vapor for groove (Figure 4.22 (b)), fully hybrid (Figure 4.22 (c)) and partially hybrid (Figure 4.22 (c)) heat pipe for different heat inputs are depicted versus time. As illustrated in Figure 4.22 (a), the maximum axial velocity in the wick increases with time since the evaporation\condensation mass transfer at the interface increases with time (up to 4 times bigger) and the density of liquid does not change significantly as illustrated in Figure 4.23 (a). At the same time, the maximum velocity of the vapor has a pick (except the low heat input of Q = 30 W) in the first 5 seconds of heat pipe operation and it gradually decreases to a lower value at the steady-state condition. To the best of author's knowledge, this is the first time such a velocity profile is reported and that is because the density of the vapor changes with time and the rate of this change is slower than the rate of mass transfer change. This is illustrated by calculating the product of average vapor density and maximum vapor velocity (for the groove heat pipe with Q =150 W as an example) as shown Figure 4.23 (b).

The mass transfer balance at the liquid-vapor interface (Eq. (2.28)) for groove heat pipe is depicted versus time in Figure 4.24 for different heat inputs. The value of mass transfer balance first decreases sharply and then increases to zero gradually with time. The reason behind this is that evaporation mass transfer is more than condensation mass transfer at the beginning ($\dot{m} < 0$ means evaporation) and they reach the save values as steady-state approaches. Also, this difference is more for high heat inputs however, they all limit to zero with time.

The interfacial mass transfer profile for groove (Figure 4.25 (a)) and partially hybrid (Figure 4.25 (b)) heat pipe are shown in Figure 4.25 versus time for heat input Q = 90 W in different times. As illustrated, the evaporation mass transfer is strong only as long as the heating length, however, the condensation mass transfer length is longer than the cooling length at the beginning of the operation of heat pipe and this length decreases to the cooling length with time. Also, the maximum absolute value of evaporation mass transfer is larger than the condensation corresponding value and this ratio ($17.08\times10^{-7}/11.43\times10^{-7}$ =1.49) is almost as equal as the ratio (0.160/0.110 =1.46) of cooling and heating lengths section. Moreover, as time goes by, the point where there is no mass transfer moves along the heat pipe till steady-state conditions is reached. This point where evaporation changes to condensation is named $x_{m=0}$ in this study or $x_{seperation}$ by [63]. The zero mass transfer point is depicted versus time for different heat inputs for hybrid heat pipe (Figure 4.26 (a)) and then compared in heat pipes with different wick structure (Figure 4.26 (b)) but only for heat input Q =90 W. As shown Figure 4.26 (a), the zero mass transfer point starts at the very end of heating length (0.11 m) and increases up to (0.16 m) for all the heat inputs when steady-state conditions is reached. The zero mass transfer point have the same behavior in heat pipe with different wick structures, as illustrated in Figure 4.26 (b).

The operating pressures for hybrid wick heat pipe are depicted in Figure 4.27 versus time for different heat inputs. Since the operating pressure strongly depends on the temperature of vapor core, it increases with heat inputs and as well as time as the temperature of vapor core increases. But also, the mass of vapor increases with time as shown in Figure 4.28 because of the mass addition to the vapor core since the evaporation mass transfer is more than condensation mass transfer at the beginning of the operation of heat pipe. Same trends for both operating pressure and mass of vapor are seen for other types of heat pipes studied in this research.

The axial hydrodynamic vapor pressure ($\hat{P}$) along the vapor core is depicted in different times for groove (Figure 4.29 (a)) and partially hybrid (Figure 4.29 (b)) heat pipes for heat input of Q =90 W. As shown in Figure 4.29, the pressure gradients are the sharpest at the heating section where the evaporation is more strong and pressure decreases significantly along the heating section (x =0.0 m – 0.11 m) going toward the middle of the heat pipe and the pressure gradients are more sharp as time passes since the evaporation mass transfer increases with time. The pressure term and gradients decrease within the adiabatic section (x = 0.11 m – 0.21 m) as the evaporation and condensation mass transfer decreases. Also, the minimum pressure point moves along the heat pipe with time as well as the zero mass transfer point moves with time however the minimum pressure point is a little ahead of zero mass transfer point. Moreover, the pressure starts to increase within the cooling section (x =0.21 m – 0.37 m) as time passes and this rise gets sharper as time passes.

The axial hydrodynamic vapor pressure along the vapor core are depicted in different times for groove (Figure 4.30 (a)) and partially hybrid (Figure 4.30 (b)) heat pipes for heat input of Q =90 W. As shown in Figure 4.30, the liquid pressure in the wick region are a few order of magnitude bigger than the corresponding values in the vapor core. The liquid pressure in different times and different cases have the similar trends and the blowing (evaporation) and suction (condensation) effects are not big enough to change the trends. Also, the liquid pressure increases with time because the mass transfer increases with time until steady-state condition is reached.

The total liquid pressure drop across the wick for different wick structures versus time are depicted and compared in Figure 4.31 for different heat inputs. As expected, the pressure drop increases with time since the mass transfer is increasing until the steady-state is reached. Also, it increases with heat input which generates more mass transfer within the vapor and wick domain. Moreover, the groove heat pipe has the highest pressure drop since the thickness of the wick through which liquid has to flow is less than other wick structures. The pressure drop for partially hybrid and fully hybrid heat pipes are close together, however, the partial hybrid has a smaller pressure drop.

The total vapor pressure drop across the vapor domain for partially hybrid heat pipe versus time are depicted and compared in Figure 4.32 for different heat inputs. As expected, the pressure drop increases with time since the mass transfer is increasing until the steady-state is reached however, optimum picks are shown for high heat inputs due to the velocity pick explained earlier as well as the density change in time.

The transient heat dissipated from the cooling section for different heat inputs is depicted in Figure 4.33 versus time. The heat input for each case is added for comparison as well. The heat dissipation increases with time and reaches the corresponding input heat around 75 seconds.

4.3.2 Steady-State

The transient results were presented up to 75 seconds in the previous section. However, the heat pipes are simulated up to 150 seconds but the maximum wall temperature for instance, only changed less than 0.01% from 75 seconds to 150 seconds. The steady-state wall temperature distributions are already shown in Figure 4.13 (grooves), Figure 4.14 (fully hybrid), and Figure 4.15 (partial hybrid).

The results presented in this section are after 150 seconds. The total temperature difference, equivalent thermal resistance and equivalent thermal conductivity of heat pipes with different wick structures and heat inputs are listed in Table 4.8. As illustrated, the groove heat pipe had the smallest temperature difference for the same heat input, followed by fully hybrid heat pipes and partial hybrid, respectively. Although the temperature differences are not significantly big, they increase as the heat input increase. The equivalent thermal resistance of heat pipe is formulated as:

$$R = \frac{\Delta T}{Q_{real}} \tag{4.1}$$

The equivalent thermal resistances are listed in Table 4.8. The thermal resistance decreases with heat input and partial hybrid heat pipe have the highest thermal resistance at the same heat inputs. The equivalent thermal conductivity of the heat pipe is calculate as:

$$k_{eq} = \frac{L_{eq}}{A_c R} \tag{4.2}$$

Where A_C and L_{eq} are the total cross area of heat pipe and distance from center of evaporation section to the center of condensation center, respectively. The equivalent thermal conductivity of the heat pipes increases with heat input meaning the heat pipe would even perform better as the heat input increase.

It is not only the thermal performance of heat pipe that is important but also the pressure drop along the wick and vapor domain are also important and play a very critical role in heat pipe operation. Liquid, vapor and total pressure drops are listed in Table 4.9 for all the heat inputs with different wick structures. Pressure drops increase with heat input for all the cases since the mass transfer has to increase to transfer the corresponding amount of heat. The liquid pressure drops are one order of magnitude bigger than those of vapor although the average liquid velocities are a few orders of magnitude smaller than those of vapor. This is due a combination of different factors as: the viscosity and density of liquid is higher than the corresponding values of vapor, the wick structure (porous media) have a much higher pressure drop, the thickness of the wick is much smaller than the vapor core. The fully hybrid wick structure has the lowest pressure drop since the thickness of its wick structure (grooves + screen mesh) is bigger than other types of wick structures, therefore, it has a lower average velocity and a lower pressure drop in results. Partial hybrid heat pipes have a smaller presser drop compared with groove heat pies for the very reason mentioned above. The fully hybrid heat pipe pressure drops are the highest among the cases and it could be because of the thickness of the vapor domain is the lowest in this case. After all, the total pressure drops which is the summation of liquid and vapor pressure drop are included.

4.4 Parametric Study

4.4.1 Accommodation Coefficient

From the kinetic theory perspective, the interface mass transfer phenomenon occurring during the condensation or evaporation process can be defined as the difference between the rate of arrival of molecules from the vapor space towards the interface and the rate of departure of molecules from the surface of the liquid into the vapor space. For the condensation process the arrival rate of molecules exceeds the departure rate; conversely during the evaporation process the departure rate exceeds the arrival rate of molecules. In an evaporation, only a fraction (σ_e) of the molecules crossing the surface in the direction of surface normal is actually due to vaporization. The remaining fraction ($1-\sigma_e$) is due to the reflection of vapor molecules that strike the interface but do not condense [34]. Likewise, the fraction of the molecules crossing the surface that condense and are not reflected is designated σ_c. Usually, σ_c and σ_c are assumed to be equal ($\sigma_c = \sigma_e = \sigma$) even for the dynamic case, although the validity of this assumption is suspected. Marek et al. [152] stated that as an interface is usually in a state of non-equilibrium, the equality of the condensation and evaporation coefficient cannot generally be assumed. In the case of water, Rubel and Gentry [153] revealed that the condensation coefficient for water is approximately 1.2 times greater than the evaporation coefficient. It was found that the condensation/evaporation coefficient is not a constant value, it changes with pressure; experimental data show that in the case of water the condensation/evaporation coefficient decreases with pressure. Eames et al. [154] also reviewed the evaporation coefficient of water. Mills [155] suggested that molecular accommodation is less than perfect only when the system in impure. Because extreme purity is unlikely in most engineering systems, a value of σ less than 1 is expected. Sukhatme and Rohsenow [156] found that their data implied σ values ranging from 0.37 to 0.61. Some of this variation was attributed to possible changes in the level of system contamination from test to test. Accommodation coefficient for vaporization of a wide variety of substances were compiled by Paul [157]. For liquid ethanol, methanol, *n*-propyl alcohol and water, the reported values of σ range from 0.02 to 0.04. On the other hand, reported values of σ for benzene and carbon tetrachloride are near 1.

To further investigate the effect of accommodation coefficient, the groove heat pipe is tested for different values of σ ranging from 0.01 to 1 and the results are presented in this section. The accommodation coefficients and how they change the $2\sigma/(2-\sigma)$ term and also how this latter term relates to the corresponding term used in this study $(2\times0.03/(2-0.03))$ are shown in Table 4.11. One can notice, the $\sigma = 1.0$, results in a 65 times higher factor (to be used in Eq. (2.23)) compared to the factor used in this study. The maximum wall temperature are depicted for Q =30 W (Figure 4.34 (a)) and Q = 150 W (Figure 4.34 (b)) versus time. As illustrated, the wall temperature decreases with increasing of σ significantly, as was expected. The vapor (Figure 4.35 (a)) and liquid (Figure 4.35 (b)) pressure drops versus time of Q =150 W case for different accommodation coefficients are shown in Figure 4.35. The vapor pressure drop does not change significantly with different σ and the small difference is due to the density change which is a function of temperature and pressure. As illustrated in Figure 4.35 (b), the liquid pressure drop is not quite dependable on the value of σ since the velocity in the wick is a function of the amount of mass transfer which itself is dependent on heat input only. This matter is well illustrated in Figure 4.36 (a) which is the steady-state interfacial mass transfer for Q =90 W. As shown, the steady-state mass transfer profiles for different σ are identical. However, the interfacial mass transfer profiles are significantly different at the beginning of heat pipe operation, as depicted in Figure 4.36 (b) for t = 0.584 s. At steady-state condition, the total temperature differences are calculated for different heat inputs and are compared in Figure 4.37 (a) for different values of σ. As mentioned earlier, increasing the σ results in a better heat transfer performance and smaller temperature difference. The equivalent thermal conductivity of heat pipe for different heat inputs and σ are computed and shown in Figure 4.37 (b). As illustrated, the equivalent thermal conductivity of the heat pipe increases significantly with σ however, this rise is sharper for the low heat inputs. Also, Figure 4.37 (b) shows there is cap for the equivalent conductivity as a function of mass transfer at the interface and that cap is no different for different heat inputs.

4.4.2 Micro-scale Effects

Modeling of heat pipes is very complicated since there are different mechanisms involved in the device level as well as micro scale effects such as: the capillarity of the porous medium, evaporation and condensation in the wick structure. Models with approximate coupling between the micro and macro scale mechanisms are developed with fair predictions of heat pipe performance. In the majority of published studies, the wick structure is assumed continuous porous medium and the implications of micro-scale phenomena such as thin-film evaporation and Marangoni convection in the wick pores were not been given much attention. Evaporation heat transfer from the thin liquid film near the solid–liquid contact line of a liquid meniscus were shown to account for more than 60% of the total heat transfer occurring from the meniscus [23, 62, 100].There are a few works [23, 62, 100, 105, 118, 158-160] which took into account some of the micro-scale effects with different model. Ranjan [23] and Ranjan et al. [62, 100] studied the influence of the wick microstructure on evaporation and condensation mass fluxes at the liquid–vapor interface by integrating a microstructure-level evaporation model (Ref. [100]) with the device-level model (Ref. [62]). They calculated the ratio of total interfacial mass transfer with and without micro-scale effect for parallel wires as the wick and formulated as (Ref. [62]):

$$f_{c-f} = \frac{m_{curved}}{m_{flat}} = \frac{m''_{curved}}{m''_{flat}} \times \frac{A_{curved}}{A_{flat}} \tag{4.3}$$

Based on the micro-scale model, the area ration is correlated as [62]:

$$\frac{A_{curved}}{A_{flat}} = 1.577\varphi^{1.7043}\theta^{-0.0693} \tag{4.4}$$

Where φ and θ are the porosity and contact angle, respectively. The mass transfer rates ratio when $\sigma = 0.03$ is correlated as [62]:

$$\frac{m''_{curved}}{m''_{flat}} = 2.21e^{-0.001\theta} \tag{4.5}$$

In order to include the micro-scale effects into the device level model, the Eq. (2.23) is modified to have an extra factor as:

$$\dot{m}'' = f_m \left(\frac{2\sigma}{2-\sigma}\right) \frac{1}{(2\pi R)^{1/2}} \left(\frac{P_v}{(T_v)^{1/2}} - \frac{P_{int}}{(T_{int})^{1/2}}\right) \tag{4.6}$$

Where the mass transfer factor is as:

$$f_m = \begin{cases} f_m = 1 & \therefore Condensation \\ f_m = f_{c-f} & \therefore Evaporation \end{cases} \tag{4.7}$$

Since the condensation site is always flooded and the contact angle is close to 90°, the curvature is almost flat and the mass transfer ratio is set to be 1 for condensation. The correlations by Ref. [62] (Eq. (4.4) and Eq. (4.5)) are adopted here with evaporative contact angle of 45° (θ =45°) the area ration, the mass flux ratio and the total ratio (f_{c-f}) are calculated to be 0.66, 5.74 and 3.79, respectively. This final factor (f_{c-f}=3.79) is used based on Eq. (4.7) to predict the thermal performance of the heat pipes investigated in this research.

The transient maximum wall temperature for different heat inputs with and without micro-scale effects are compared for fully hybrid heat pie (Figure 4.38 (a)) and partial hybrid (Figure 4.38 (b)) heat pipe. It is shown that including the micro-scale effects enhanced the thermal performance of heat pipe with both fully hybrid and partial hybrid wick structures. This thermal improvement is reported while the steady-state mass transfer is not any different compared without micro-scale effects. This is illustrated in Figure 4.39 (b) as the interfacial mass transfer with and without micro-scale effects are identical. The steady-state $x_{m=0}$ is depicted for different heat inputs with and without micro-scale effects in Figure 4.39 (a) for partial hybrid heat pipe. As shown, even the $x_{m=0}$ is not significantly influenced by the micro-scale. At steady-state condition, the total temperature differences are calculated with and without micro-scale effects and are compared for both fully hybrid and partial hybrid heat pipes in Figure 4.40 (a) for different heat inputs. As mentioned earlier, including the micro-scale effects results in a better heat transfer performance and smaller temperature difference which is shown in Figure 4.40 (a). Also, this enhancement increases as the heat input increases. The equivalent thermal conductivity of heat pipe for different heat inputs with and without micro-scale effects are computed and compared in Figure 4.40 (b) for partial hybrid and fully hybrid heat pipes. As illustrated, the equivalent thermal conductivity of the heat pipe is enhanced with the micro-scale included for fully hybrid (14.1% enhancement) and partial hybrid (11.6% enhancement) heat pipes. Also, the fully hybrid mesh has the best thermal performance among other cases. Note, the correction factor ($f_{c\text{-}f}$ =3.79) calculated based on Ref. [62] is not accurately calculated for the screen mesh rather it is calculated for parallel wire wick, however, this estimated correction factor is used to study the effects of micro-scale on the heat pipes presented in this research.

4.4.3 Permeability

In order to study the effects of permeability, 4 cases of fully hybrid heat pipes with different permeability values are considered as listed in Table 4.12. The permeability of the screen mesh is changes in a way that the K_A case is the very case studied in this study up to this point and K_D case has same permeability for both grooves and screen mesh. The liquid axial velocity profiles at 0.16 m ($x_{m=0}$ =0.16 m) are depicted in Figure 4.41 for different cases. The liquid tend to flow through the structure with the lowest permeability more than the other as obvious in K_A case. As the permeability of screen mesh decrease toward the permeability of the grooves, the liquid flow through the screen mesh increases as for the K_D case, there is no difference since the permeability values are the same. Moreover, the velocity profile are not parabolic because of the exciting of the porous media source terms. The transient liquid pressure drops for different cases of permeability values are depicted for Q = 30 W (Figure 4.42 (a)) and Q = 150 W (Figure 4.42 (b)). As expected, with decreasing the permeability of the screen mesh, the liquid pressure drops also decreases, this change may play an important role in capillary limit calculation. Figure 4.42 shows that the permeability values are crucial to pressure drop calculation and viscous properties of wick structure have to be addressed carefully.

4.4.4 Ergun's Coefficient

As mentioned earlier in this work, the Ergun coefficient is set to be 0.5 in heat pipe simulation by many studies (Ref.s [21, 22, 31, 58, 60, 61, 63, 93, 118]) however no explanation was found except Ref.s [40, 98]. The transient liquid pressure drops are depicted in Figure 4.43 for groove heat pipe with Q = 150 W to show the effects of Ergun coefficient. As expected, the pressure drop increases with increasing Ergun coefficient and this change may play an important role in capillary limit calculation.

4.4.5 Capillary Pressure and Pressure Drop

The most important limitation of heat pipe is the capillary limit since the capillary pressure head in the evaporation section is the pumping force to loop the fluid through evaporation and condensation sections and through the wick structure and vapor core. The maximum capillary pressure head should exceed the total pressure drop in the wick and vapor regions in order for the heat pipe to operate, as formulated by Chi [161] as (in the absence of gravity):

$$\Delta P_c \geq \Delta P_l + \Delta P_v \tag{4.8}$$

Where ΔP_c, ΔP_l and ΔP_v are capillary pressure head, total liquid pressure drop and total vapor pressure drop, respectively. The fluid can loop throughout the heat pipe as long this conditions is met and if not, the dry-out condition happens where not enough fluid can return to the evaporation section to evaporate and the heat pipe would failed. The capillary pressure head can be calculated as [21]:

$$\Delta P_c = 2\sigma_f \left(\frac{\cos\theta_e}{r_0} - \frac{\cos\theta_c}{r_0}\right) \tag{4.9}$$

Where σ_f, θ_e, θ_c and r_0 are surface tension, evaporation contact angle, condensation contact angle and curvature radius. The maximum capillary pressure head is obtained when the evaporation and condensation contact angle is 0° and 90°, respectively. The maximum capillary pressure head can be calculated as [21, 118]:

$$\Delta P_c = \frac{2\sigma_f}{r_0} \tag{4.10}$$

The curvature radius for screen mesh structure can be calculated as [118]

$$r_0 = \frac{1}{2M} = 8.76 \times 10^{-5}\ m \tag{4.11}$$

Where M is the mesh number. The curvature radius for groove structure can be calculated as:

$$r_0 = \frac{d_{gap}}{2} = 2.21 \times 10^{-4}\ m \tag{4.12}$$

Where d_{gap} is the gap distance between the grooves on the very tip of grooves which can be calculated based on the geometry of the grooves. The maximum capillary pressure head for groove, fully hybrid and partial hybrid heat pipes are computed as 616.08 Pa, 1552.85 Pa and 1552.85 Pa, respectively. These pressure heads are calculated assuming the average temperature of the heat pipe to be 50 °C (σ_f =0.068 N/m). In order to check the heat pipes investigated in this study, the total pressure drop of liquid and vapor (as listed in Table 4.10) are compared with the maximum capillary pressure head in Table 4.9. As illustrated, all the heat pipes satisfy the capillary limits for all the heat inputs and wick structures as the worst case scenario (groove structure with Q = 150 W) have a total pressure drop of 82.3% of capillary limits.

4.4.6 Mach Number

The sonic limitation in heat pipes comes about because of the change in the vapor velocity of the heat pipe due to the axial variation of vaporization and condensation. Similar to the effect of decreased outside pressure in a converging-diverging nozzle, a decreased condenser temperature results in a decrease in the evaporator temperature up to the point where chocked flow occurs in the evaporator, causing the sonic limit to be reached. Any further changes in condenser condition do not reduce either the evaporator temperature or the maximum heat transfer capability, due to the existence of chocked flow. The Mach number is generally higher in the cylindrical heat pipe than the flat-plate heat pipe, because the vapor core cross-sectional area per heat input is much smaller, causing higher velocities. However, as the density increases with temperature and time, the compressibility effects become negligible in the cylindrical heat pipe. Mach Number can be formulated as:

$$Mach\ Number = \frac{u}{C} \tag{4.13}$$

Where C is the he speed of sound in the medium and can be calculated based on the ideal gas law as:

$$C = \sqrt{\gamma \frac{R}{M} T} \tag{4.14}$$

Where γ is the isentropic expansion factor (γ =1.31 here). In order to check the sonic limit, the local Mach number for all the heat pipes on the axisymmetric line (where the velocity is maximum) for Q =150 W are depicted in Figure 4.44 for t =3.913 s (Figure 4.44

(a)) and *t* =75.66 s (Figure 4.44 (b)). As shown, the Mach Number for all the cases stay well below the sonic limit and the assumption of incompressible flow is well satisfied. The Mach Number for *t* =3.913 s is relatively larger than the corresponding values at *t* =75.66 s since the pick of velocity occurs at the very beginning of heat pipe operation for *Q* = 150 W cases.

Table 4.1 Mechanical, thermal, viscous properties etc.

	Parameters	Values	Units
Wall	Specific Heat ($c_{p,s}$)	381	J/kg.K
	Density (ρ_s)	8978	kg/m^3
	Thermal Conductivity (k_s)	387.6	W/m.K
Wick	Specific Heat ($c_{p,l}$)	4200	J/kg.K
	Density ($\rho_{w,l}$)	$=M_L/\varphi.V_{wick}$	kg/m^3
	Dynamic Viscosity (μ_l)	6.5×10^{-4}	N.S/m^2
	Porosity, grooves (φ_{grv})	0.713	---
	Porosity, mesh (φ_{msh})	0.707	---
	Effective Thermal Conductivity, grooves (k_{grv})	1.72	W/m.K
	Effective Thermal Conductivity, mesh (k_{msh})	62.51	W/m.K
	Permeability, grooves (K_{grv})	3.00×10^{-9}	m^2
	Permeability, mesh (K_{msh})	8.61×10^{-11}	m^2
	Ergun coefficient, grooves ($C_{E,grv}$)	0.237	---
	Ergun coefficient, mesh ($C_{E,msh}$)	0.240	---
Vapor	Specific heat ($c_{p,v}$)	1861.54	J/kg.K
	Density (ρ_v)	$=P_{op}/RT$	kg/m^3
	Thermal conductivity (k_v)	0.0189	W/m.K
	Dynamic Viscosity (μ_v)	9.6×10^{-6}	N.S/m^2
Phase Change	Latent Heat (h_{fg})	2.406×10^6	J/kg
	Accommodation Coefficient	0.03	---

Table 4.2 Names and sizes of each computational grids

Name	Size
Nr, Nx	Nr =[20, 8, 8], Nx =74
Nr, 2×Nx	Nr =[20, 8, 8], Nx =148
2×Nr, 2×Nx	Nr =[40, 16, 16], Nx =148
Nr, 4×Nx	Nr =[20, 8, 8], Nx =296
2×Nr, 4×Nx	Nr =[40, 16, 16], Nx =296
4×Nr, 4×Nx	Nr =[80, 32, 32], Nx =296

Table 4.3 Mechanical, thermal, viscous parameters etc.

	Parameters	Values	Units
Wall	Specific Heat (cp,s)	381	J/kg.K
	Density (ρs)	8978	kg/m^3
	Thermal Conductivity (ks)	387.6	W/m.K
Wick	Specific Heat (cp,l)	4200	J/kg.K
	Density (ρw,l)	$=M_L/\varphi.V_{wick}$	kg/m^3
	Dynamic Viscosity (μl)	$8.\times10^{-4}$	N.S/m^2
	Porosity, grooves (φ)	0.718	---
	Effective Thermal Conductivity (keff)	1.2 or 1.7	W/m.K
	Permeability (*K*)	1.1×10^{-9}	m^2
	Ergun coefficient (CE)	0.55	---
Vapor	Specific heat (cp,v)	1861.54	J/kg.K
	Density (ρv)	$=P_{op}/RT$	kg/m^3
	Thermal conductivity (kv)	0.0189	W/m.K
	Dynamic Viscosity (μv)	8.4×10^{-6}	N.S/m^2
Phase Change	Latent Heat (hfg)	2.33×10^6	J/kg
	Accommodation Coefficient	0.03	---

Table 4.4 Different cases of different cooling conditions and thermal conductivities

		T_{con} (°C)	T_∞ (°C)	h_∞ (W/m^2.K)	k_{eff} (W/m.K)
Single Heater	Case 1	73.3	10	64.01	1.2
	Case 2	74.8	10	62.53	1.7
Four Heaters	Case 1	65.2	10	151.36	1.2
	Case 2	67.3	10	145.80	1.7

Table 4.5 Mechanical, thermal, viscous parameters etc

	Parameters	Values	Units
Wall	Specific Heat (cp,s)	385	J/kg.K
	Density (ρs)	8933	kg/m^3
	Thermal Conductivity (ks)	401	W/m.K
Wick	Specific Heat (cp,l)	4200	J/kg.K
	Density (ρw,l)	$=M_L/\varphi.V_{wick}$	kg/m^3
	Dynamic Viscosity (μl)	$8.\times10^{-4}$	N.S/m^2
	Porosity, grooves (φ)	0.5	---
	Effective Thermal Conductivity (keff)	3	W/m.K
	Permeability (*K*)	1.43×10^{-11}	m^2
	Ergun coefficient (CE)	0.55	---
Vapor	Specific heat (cp,v)	1861.54	J/kg.K
	Density (ρv)	$=P_{op}/RT$	kg/m^3
	Thermal conductivity (kv)	0.0189	W/m.K
	Dynamic Viscosity (μv)	8.4×10^{-6}	N.S/m^2
Phase Change	Latent Heat (hfg)	2.473×10^{6}	J/kg
	Accommodation Coefficient	0.03	---

Table 4.6 Heating and cooling conditions

Q (W)	q'' (W/m^2)	$T_\infty = T_0$ (K)	h_∞ (W/m^2.K)
10	8223.68	288.8	3176
30	24671.05	288.8	1695

Table 4.7 Time constants based on $T_{wall,max}$ and $T_{wall,min}$ for fully hybrid heat pipe

Q (W)	$T_{wall,max}$ Time constant (s)	$T_{wall,min}$ Time constant (s)	Time constant difference (s)
30	9.45	12.83	3.38
60	7.92	10.88	2.95
90	7.72	10.81	3.09
120	7.70	10.80	3.10
150	7.27	9.92	2.64

Table 4.8 Total temperature difference, equivalent thermal resistance and equivalent thermal conductivity

	Wick	Q (W)				
		30	60	90	120	150
ΔT (°C)	Grooves	3.39	6.02	8.38	10.57	12.52
	Hybrid	3.40	6.25	8.77	11.04	13.14
	Partial	3.55	6.52	9.25	11.59	13.74
R (°C\W)	Grooves	0.11654	0.10470	0.09732	0.09248	0.08908
	Hybrid	0.11681	0.10874	0.10183	0.09657	0.09353
	Partial	0.12190	0.11346	0.10744	0.10138	0.09781
k_{eq} (W/m.K)	Grooves	15918	17719	19061	20059	20825
	Hybrid	15881	17060	18217	19210	19832
	Partial	15218	16351	17267	18299	18966

Table 4.9 Liquid, vapor and total pressure drop for different wick structures

	Wick	Q (W)				
		30	60	90	120	150
Liquid ΔP (Pa)	Grooves	97.26	194.98	296.23	398.94	496.88
	Hybrid	88.00	176.23	267.64	360.38	448.68
	Partial	90.51	181.30	275.35	370.90	461.97
Vapor ΔP (Pa)	Grooves	3.64	6.29	8.42	11.12	10.08
	Hybrid	4.08	8.09	11.56	14.20	16.83
	Partial	3.24	6.09	8.57	9.41	9.98
Total ΔP (Pa)	Grooves	100.90	201.27	304.65	410.07	506.96
	Hybrid	92.08	184.31	279.20	374.58	465.50
	Partial	93.75	187.38	283.92	380.31	471.94

Table 4.10 Comparison of total pressure drop vs. capillary pressure head

	Wick	Q (W)				
		30	60	90	120	150
$\Delta P_{totall} / \Delta P_c$ (%)	Grooves	16.4	32.7	49.4	66.6	82.3
	Hybrid	5.9	11.9	18.0	24.1	30.0
	Partial	6.0	12.1	18.3	24.5	30.4

Table 4.11 Accommodation coefficients and their ratios

σ	$\frac{2\sigma}{2-\sigma}$	$\left(\frac{2\sigma}{2-\sigma}\right)/\left(\frac{2\times 0.03}{2-0.03}\right)$
0.01	0.0101	0.330
0.02	0.0202	0.663
0.03	0.0305	1.000
0.04	0.0408	1.340
0.1	0.1053	3.456
1	2.0000	65.667

Table 4.12 Different cases with their permeability values

Case	Grooves Permeability (m^2)	Mesh Permeability (m^2)
K_A	3.002×10^{-9}	8.615×10^{-11}
K_B	3.002×10^{-9}	2.811×10^{-10}
K_C	3.002×10^{-9}	9.187×10^{-10}
K_D	3.002×10^{-9}	3.002×10^{-9}

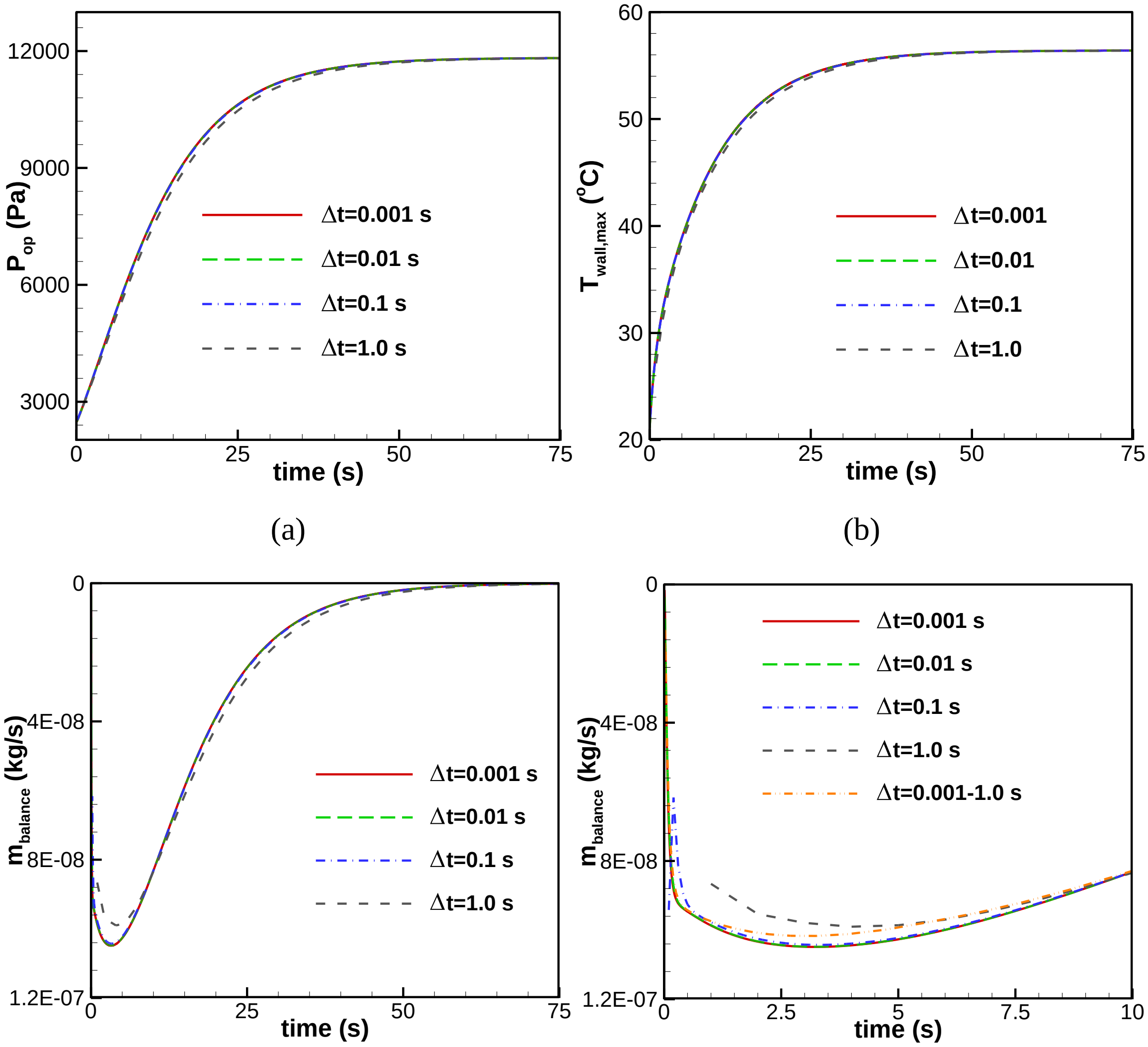

(a) (b)

(c) (d)

Figure 4.1 Fully hybrid cylindrical heat pipe (*Q* =150 W) transient results: (a) Operating pressure, (b) maximum wall temperature, (c) interface mass balance and (d) interface mass balance (first 10 second)

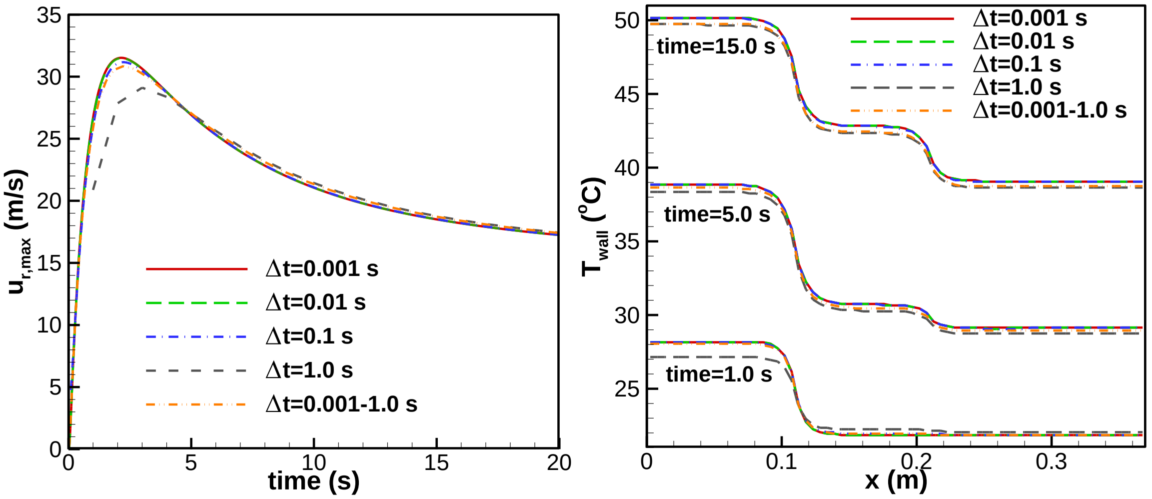

(a) (b)

Figure 4.2 (a) maximum velocity versus time for different time steps, (b) wall temperature distributions in 3 different times for different time steps

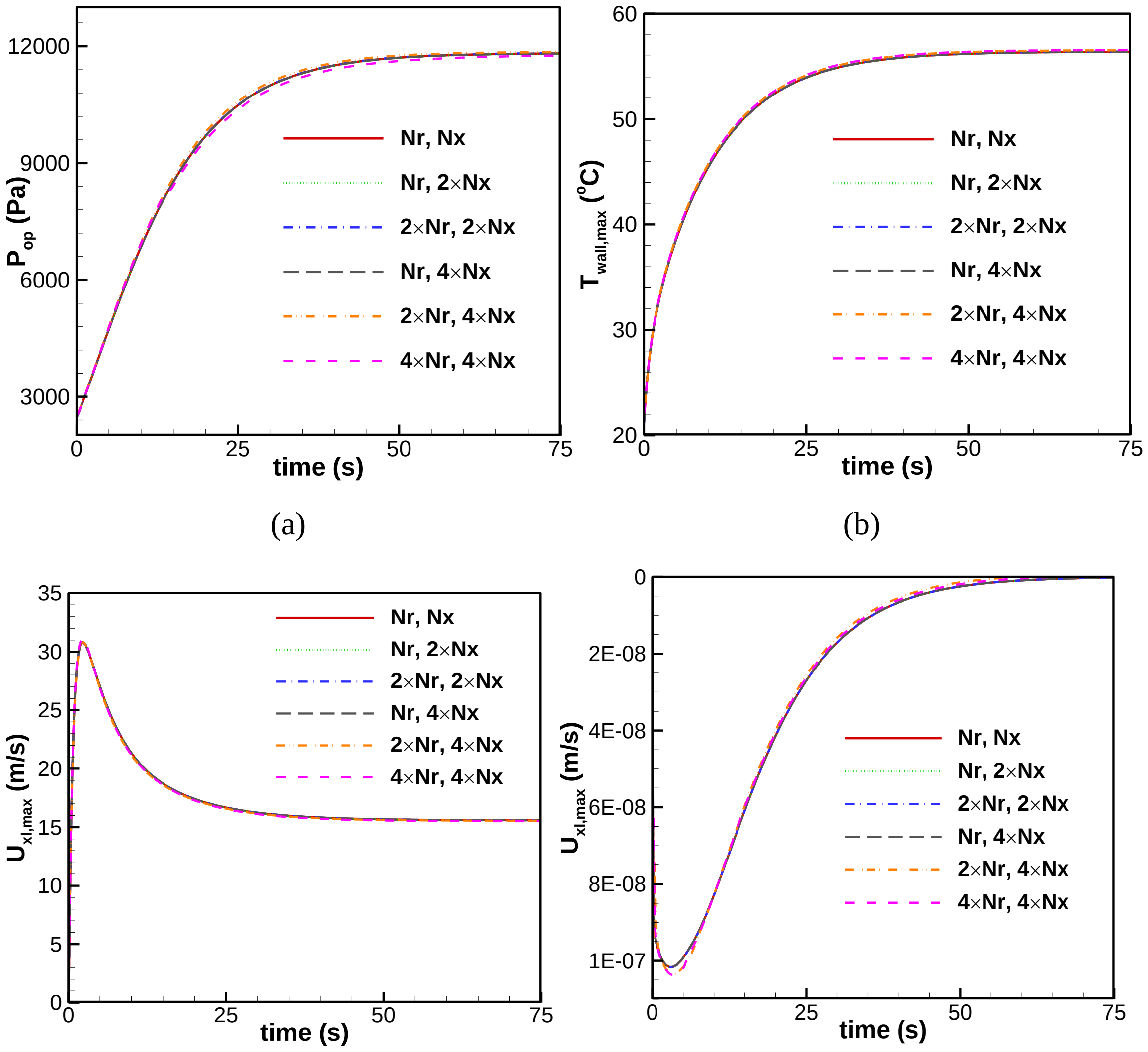

(a) (b)

(c) (d)

Figure 4.3 Groove cylindrical heat pipe (*Q* =150 W) transient results: (a) Operating pressure, (b) maximum wall temperature, (c) maximum axial velocity (d) interface mass balance for different grid sizes (listed in Table 4.2)

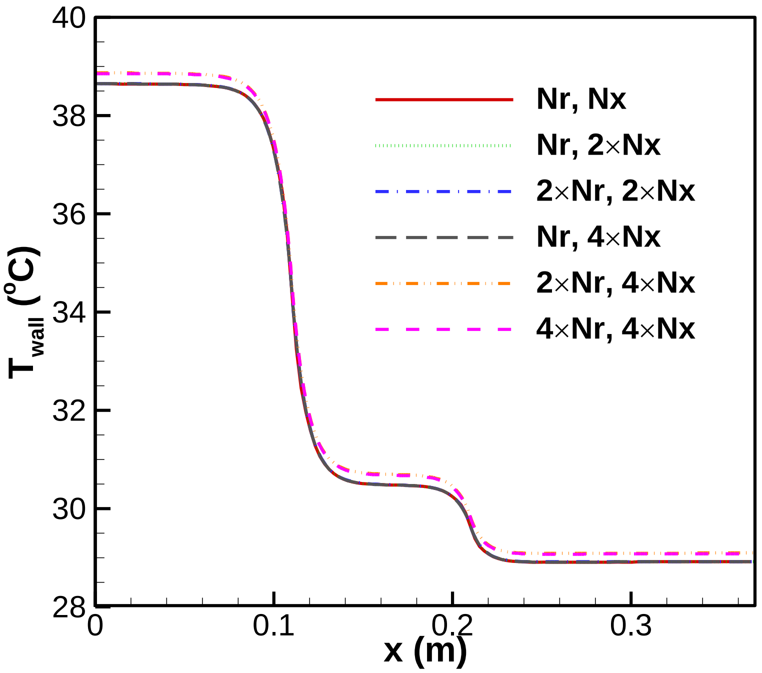

Figure 4.4 Groove cylindrical heat pipe (Q =150 W) wall temperature at *time* =5 s for different grid sizes (listed in Table 4.2)

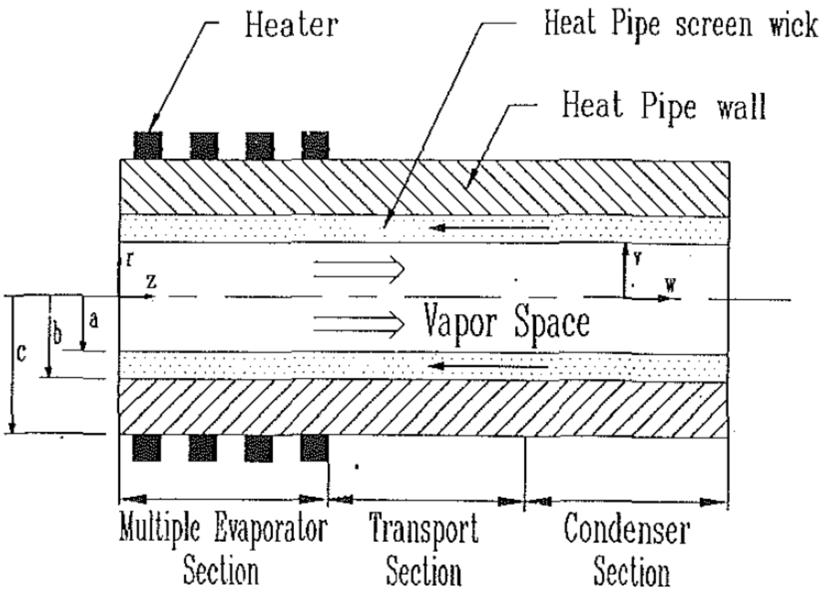

Figure 4.5 Cylindrical heat pipe studied by Faghri and Buchko [49]

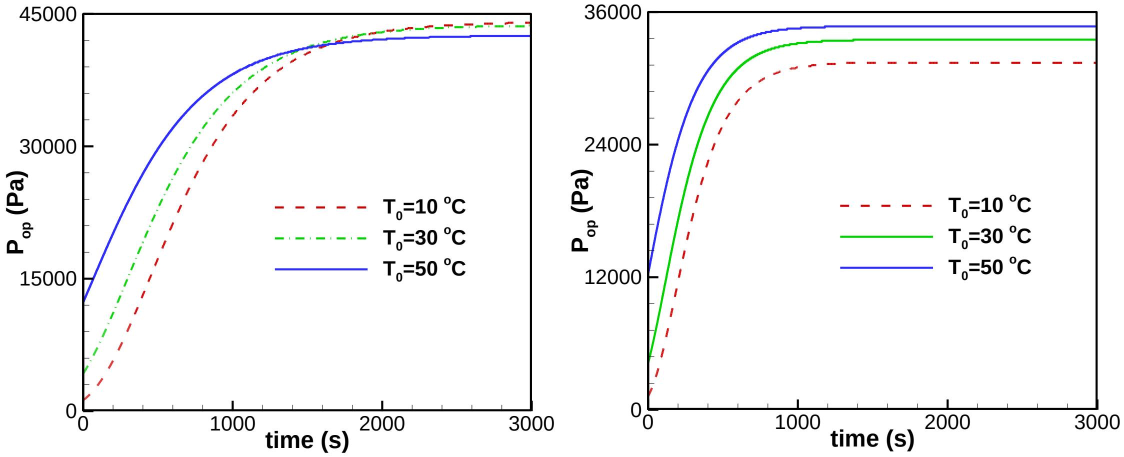

(a) (b)

Figure 4.6 Transient operating pressure for different initial conditions (a) single heater (b) four heaters

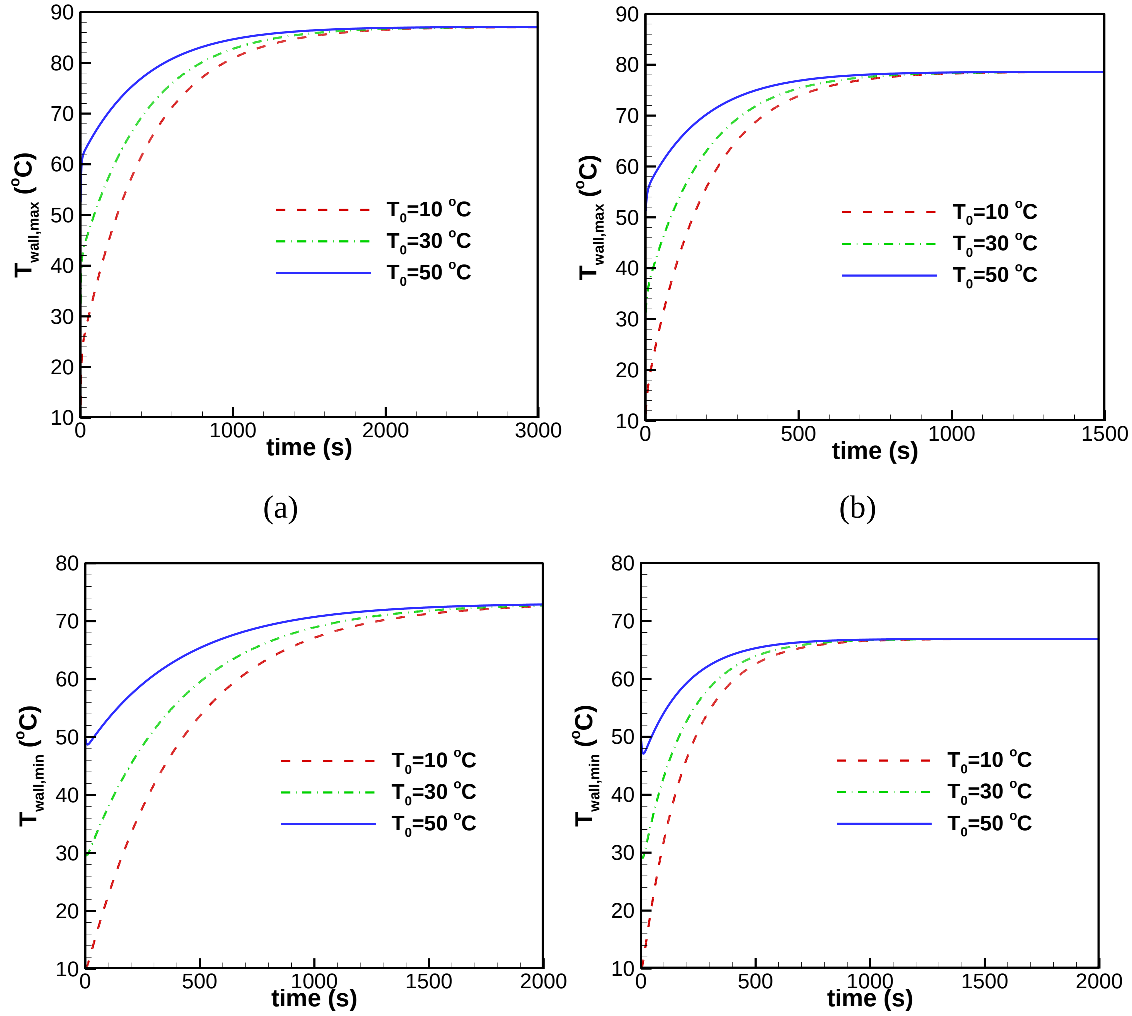

(a) (b)

(c) (d)

Figure 4.7 Transient wall maximum (a and b) and minimum (c and d) temperature for different initial conditions for single heater (a and c) and four heaters (b and d)

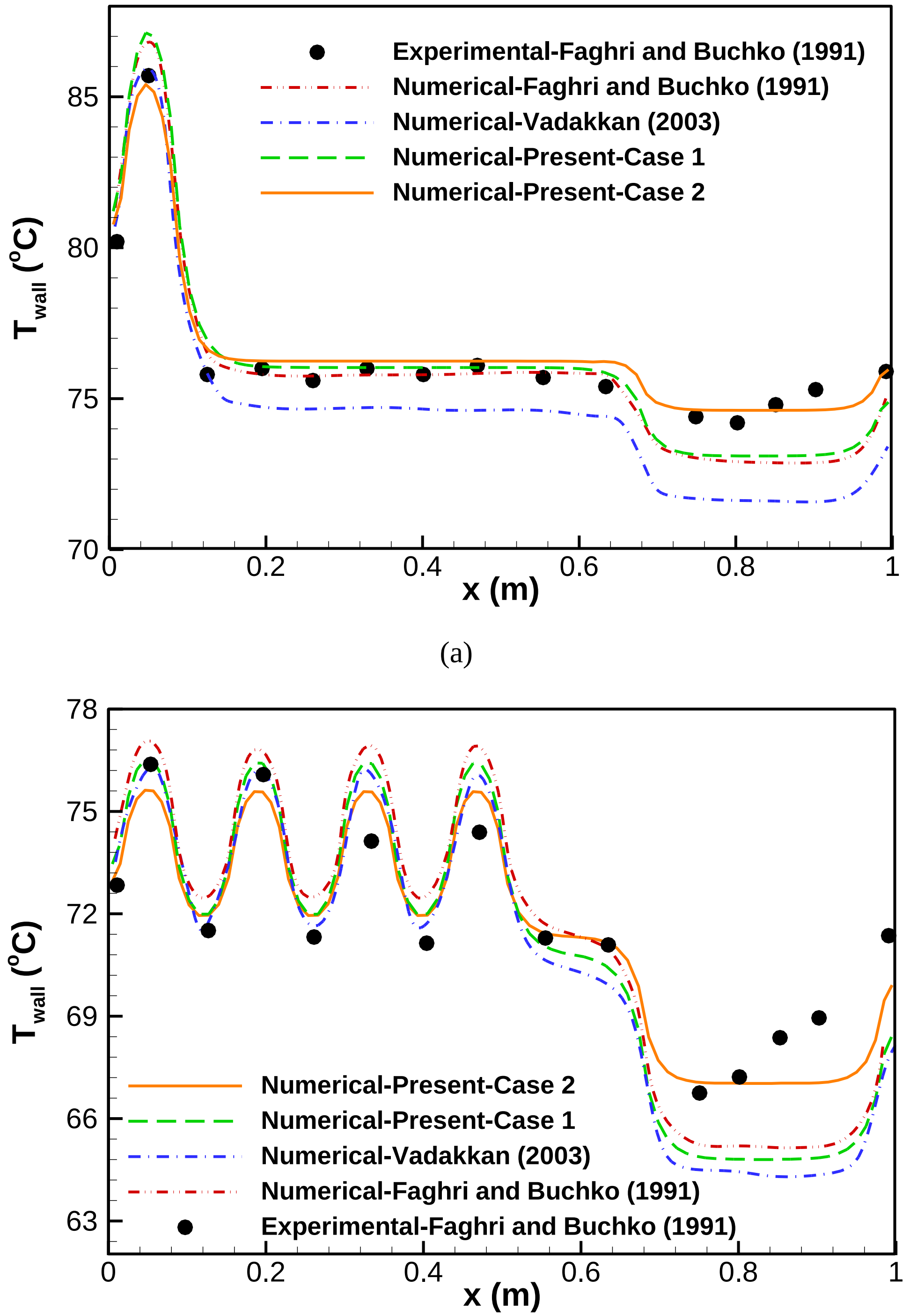

(a)

(b)

Figure 4.8 Comparison of wall temperature destitutions between the present work, Faghri and Buchko [49] and Vadakkan [21]

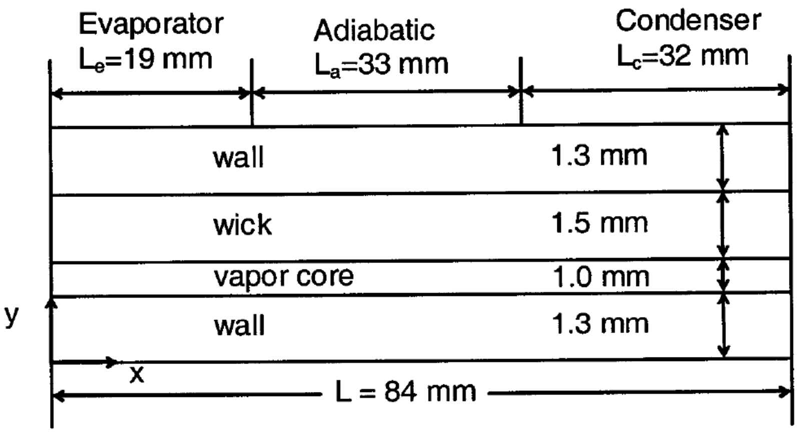

Figure 4.9 Flat heat pipe studied by Vadakkan [49]

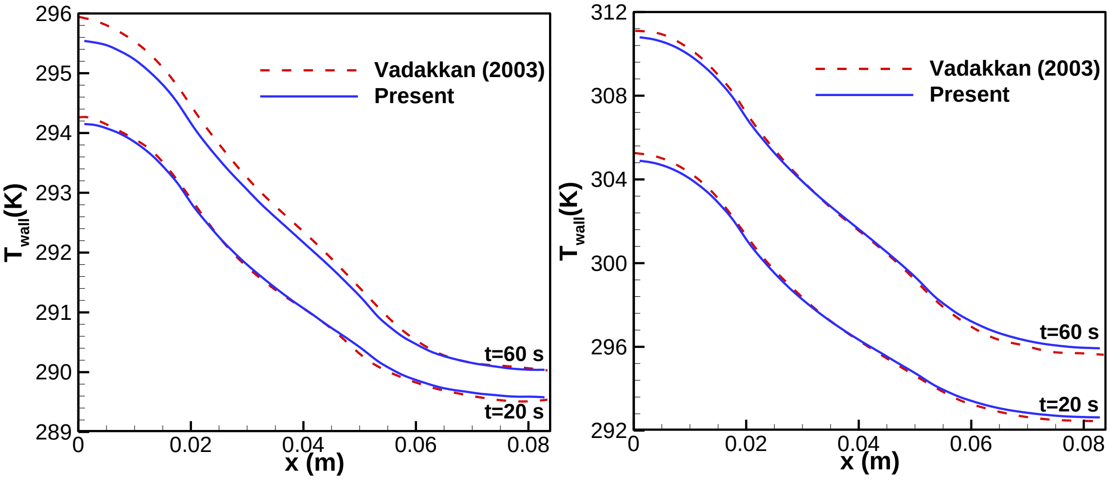

(a) (b)

Figure 4.10 Comparison of wall temperature distributions after 20 s and 60 s with Ref. [49]

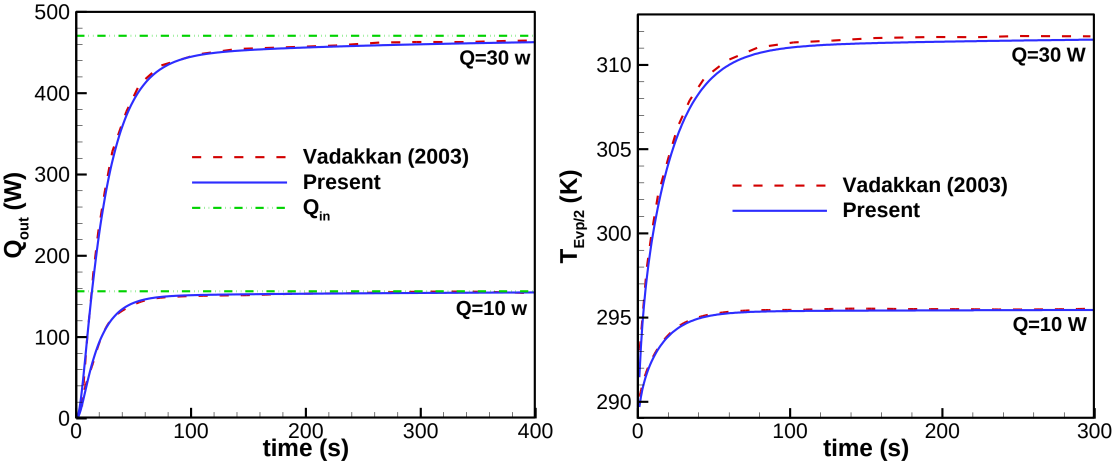

(a) (b)

Figure 4.11 Comparison of transient heat output and wall temperature of evaporation center with Ref. [49]

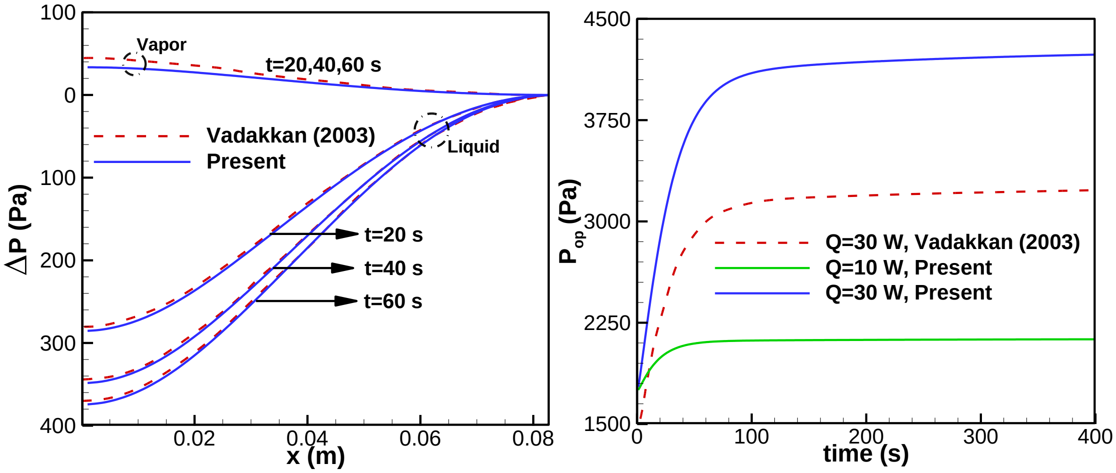

(a) (b)

Figure 4.12 Comparison of (a) Liquid and vapor pressure drop (b) Operating pressure for 30 W heat input with Ref. [49]

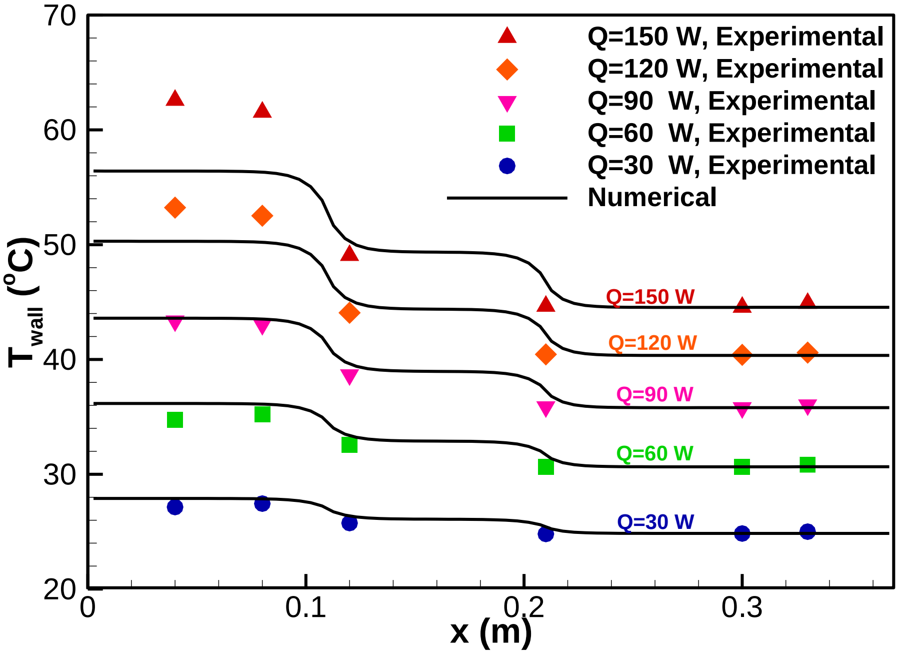

Figure 4.13 Comparison of numerical and experimental wall temperature distributions for grooves heat pipe

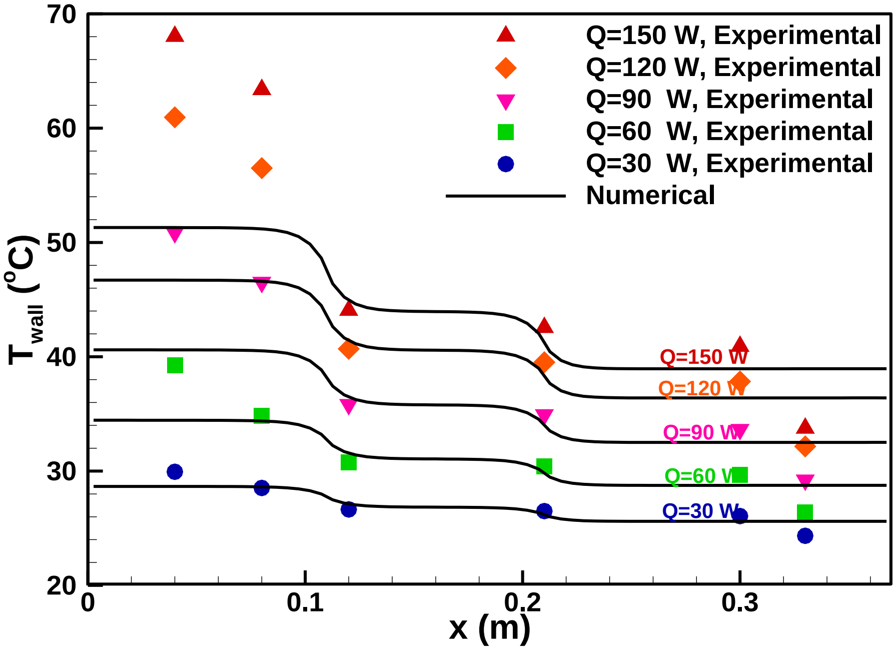

Figure 4.14 Comparison of numerical and experimental wall temperature distributions for fully hybrid heat pipe

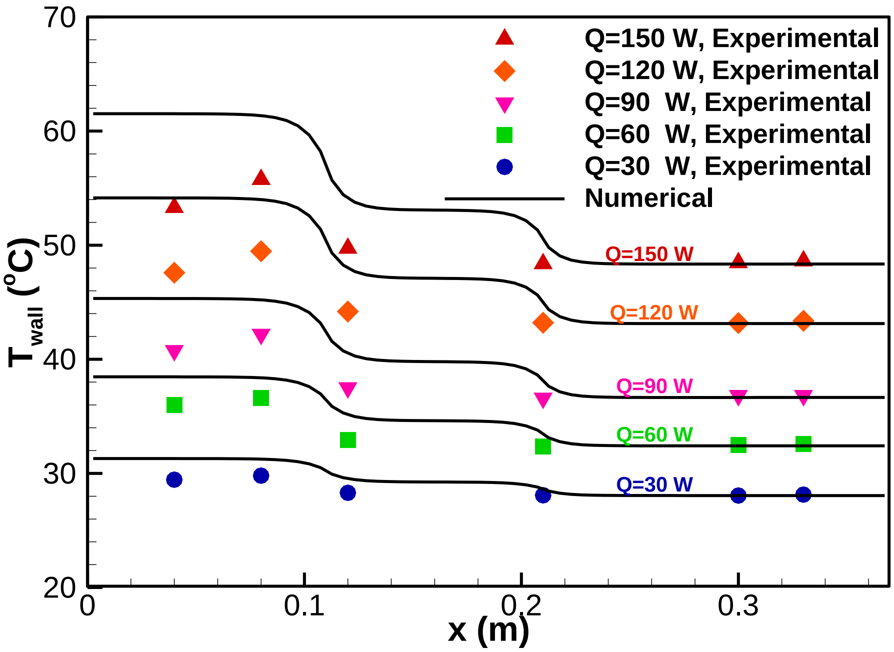

Figure 4.15 Comparison of numerical and experimental wall temperature distributions for partial hybrid heat pipe

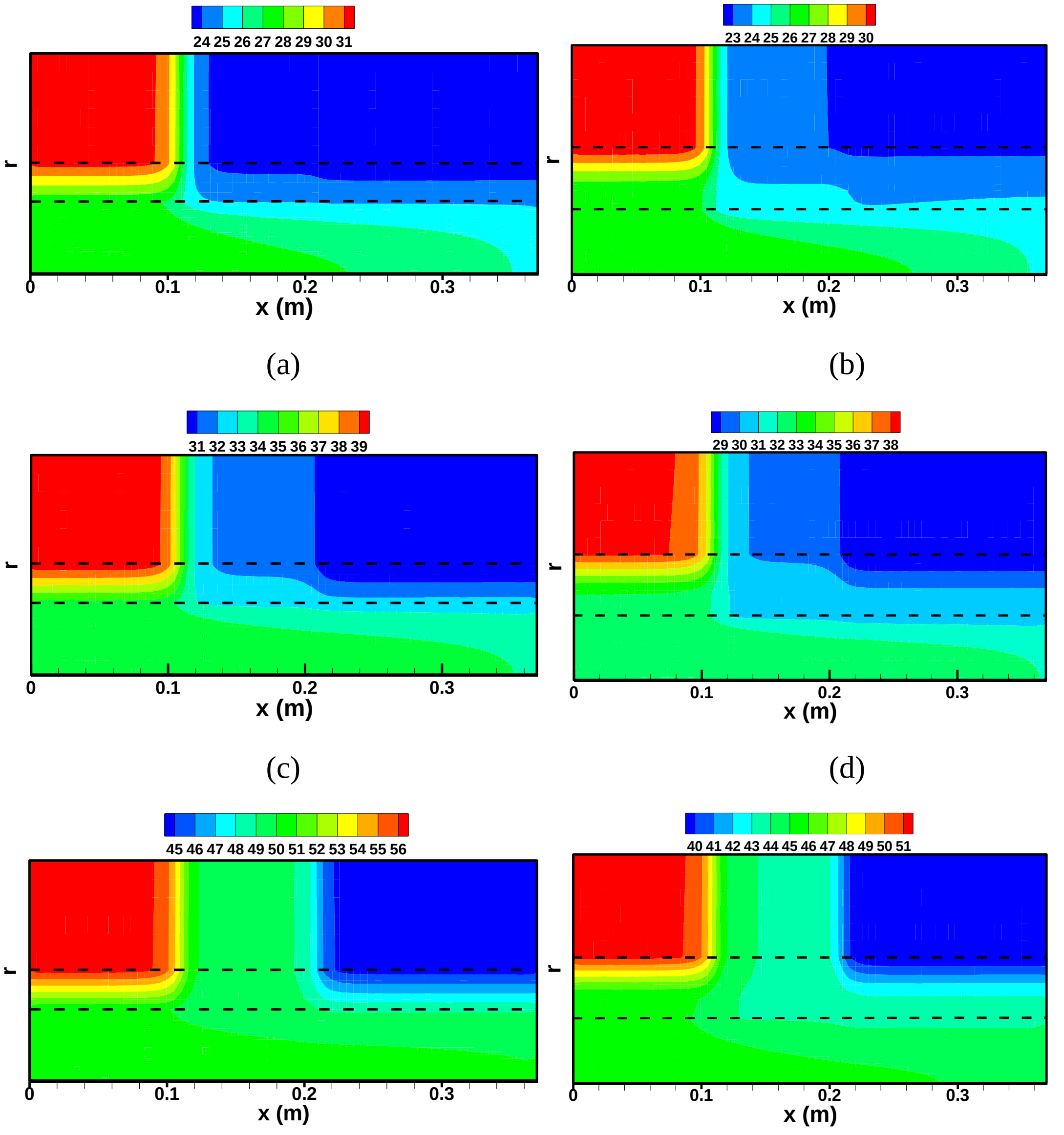

(a) (b)

(c) (d)

(e) (f)

Figure 4.16 Temperature contours of groove (a, c and e) and hybrid (b, d and f) heat pipes for *t* =1.856 s (a and b), *t* =5.66 s (c and d) and *t* =75.66 s (e and f) for the *Q* =150 W (Dimensions in r direction in the Vapor domain are magnified 10 times and in the Wick and Wall domains 100 times)

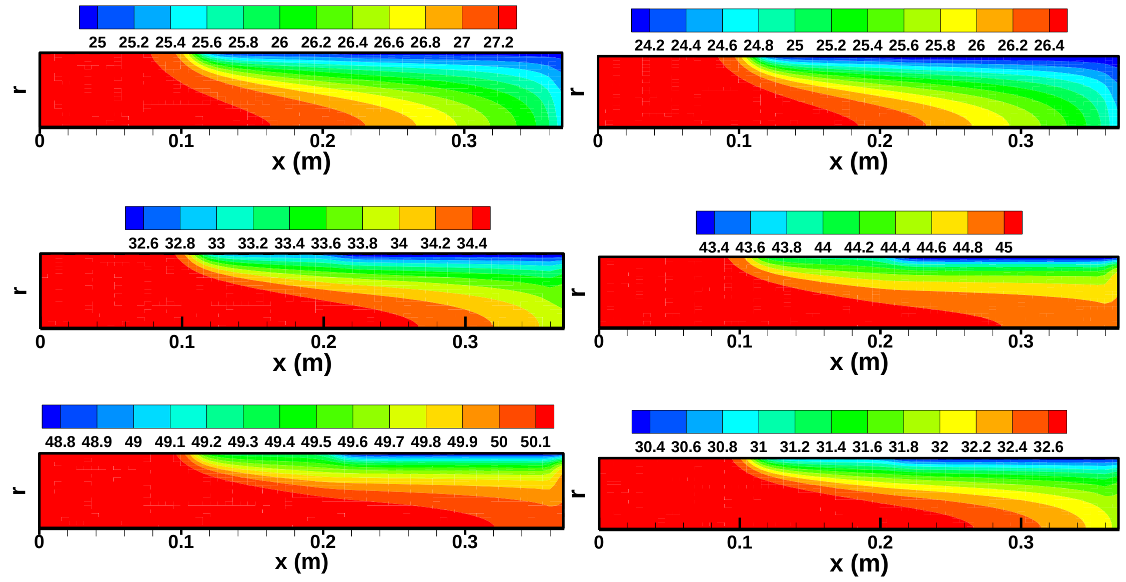

Figure 4.17 Vapor core temperature contours of groove (a, c and e) and hybrid (b, d and f) heat pipes for *t* =1.856 s (a and b), *t* =5.66 s (c and d) and *t* =75.66 s (e and f) for the *Q* =150 W.

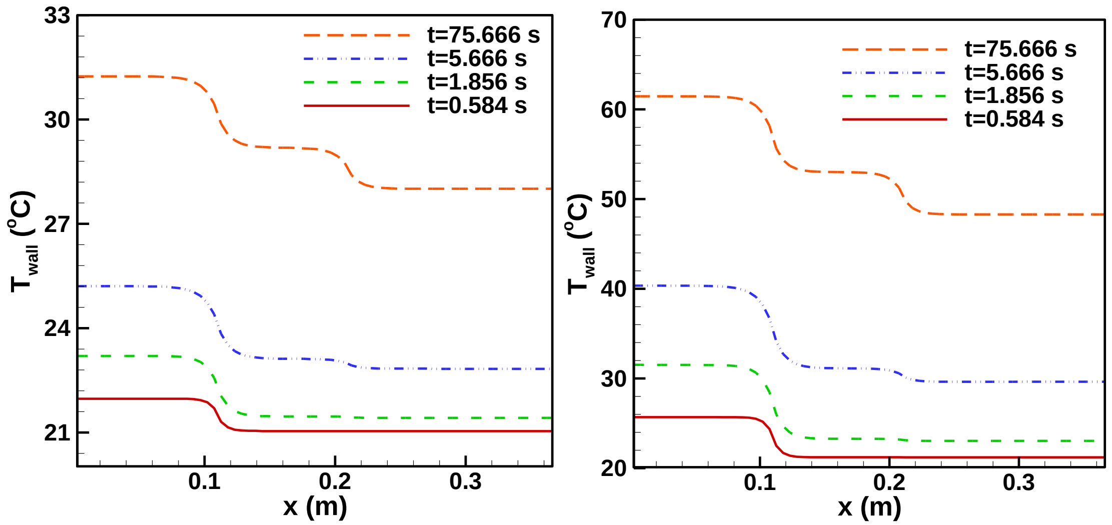

Figure 4.18 Wall temperature distributions of partially hybrid cylindrical heat pipe at different times for *Q* =30 W (a) and *Q* =150 W (b)

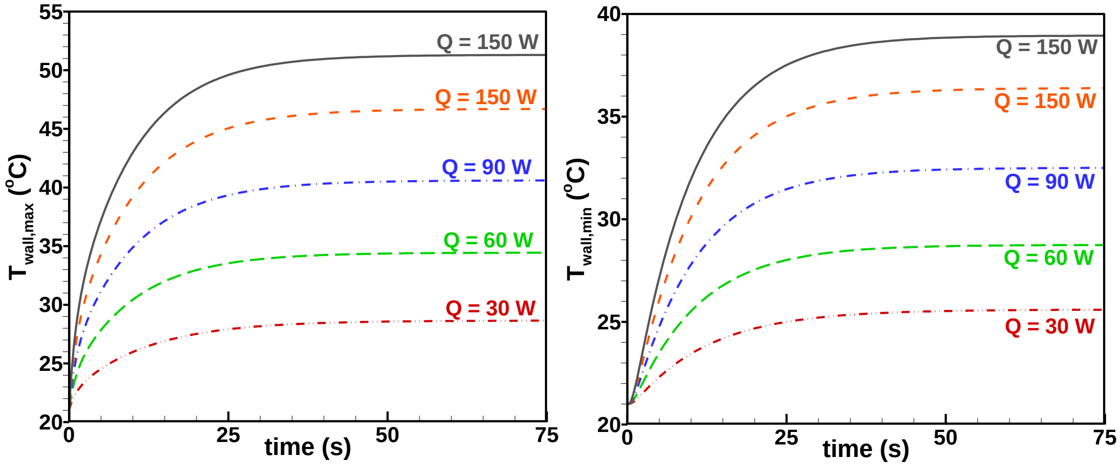

(a) (b)

Figure 4.19 Fully hybrid heat pipe maximum (a) and minimum (b) wall temperatures versus time for different heat inputs

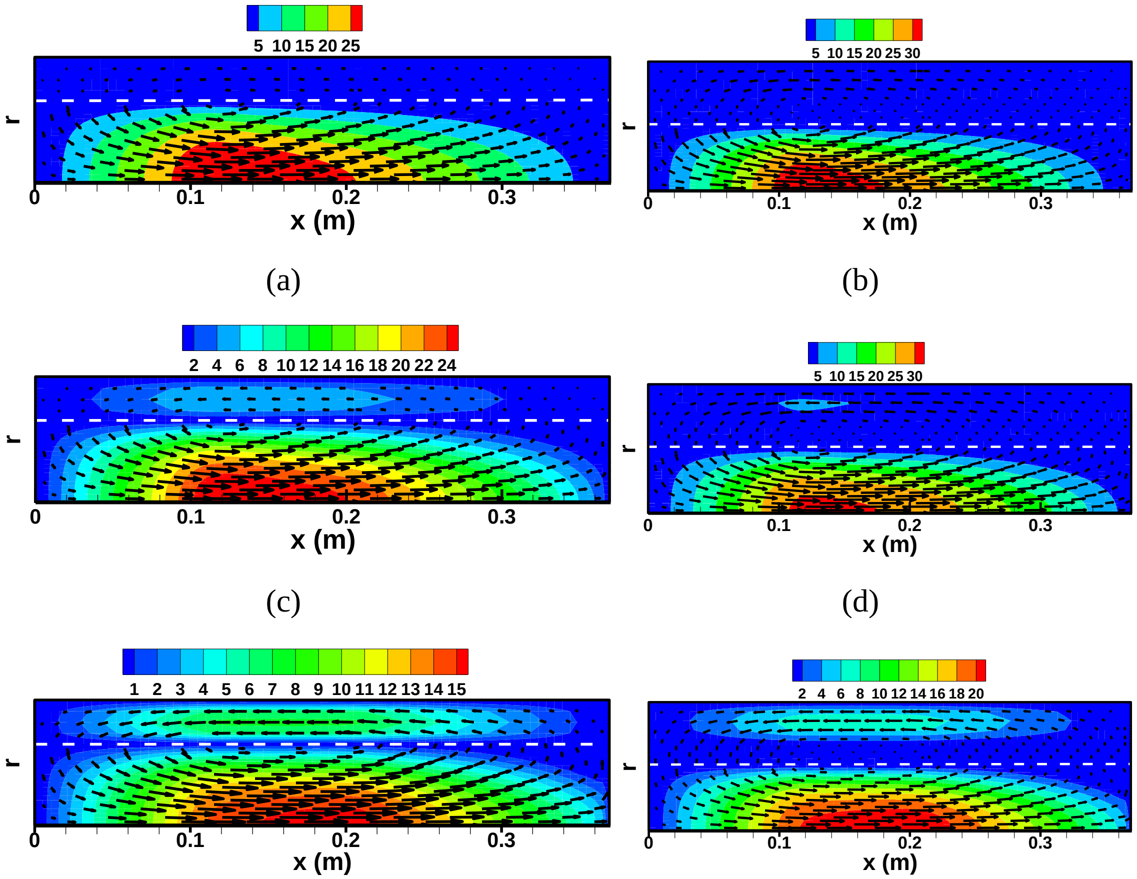

(a) (b)

(c) (d)

(e) (f)

Figure 4.20 Velocity vectors and absolute value contours of groove (a, c and e) and hybrid (b, d and f) heat pipes for t =1.856 s (a and b), t =5.66 s (c and d) and t =75.66 s (e and f) for the Q =150 W (velocities in wick region are magnified for groove (1000 times) and hybrid (2000 times) cases)

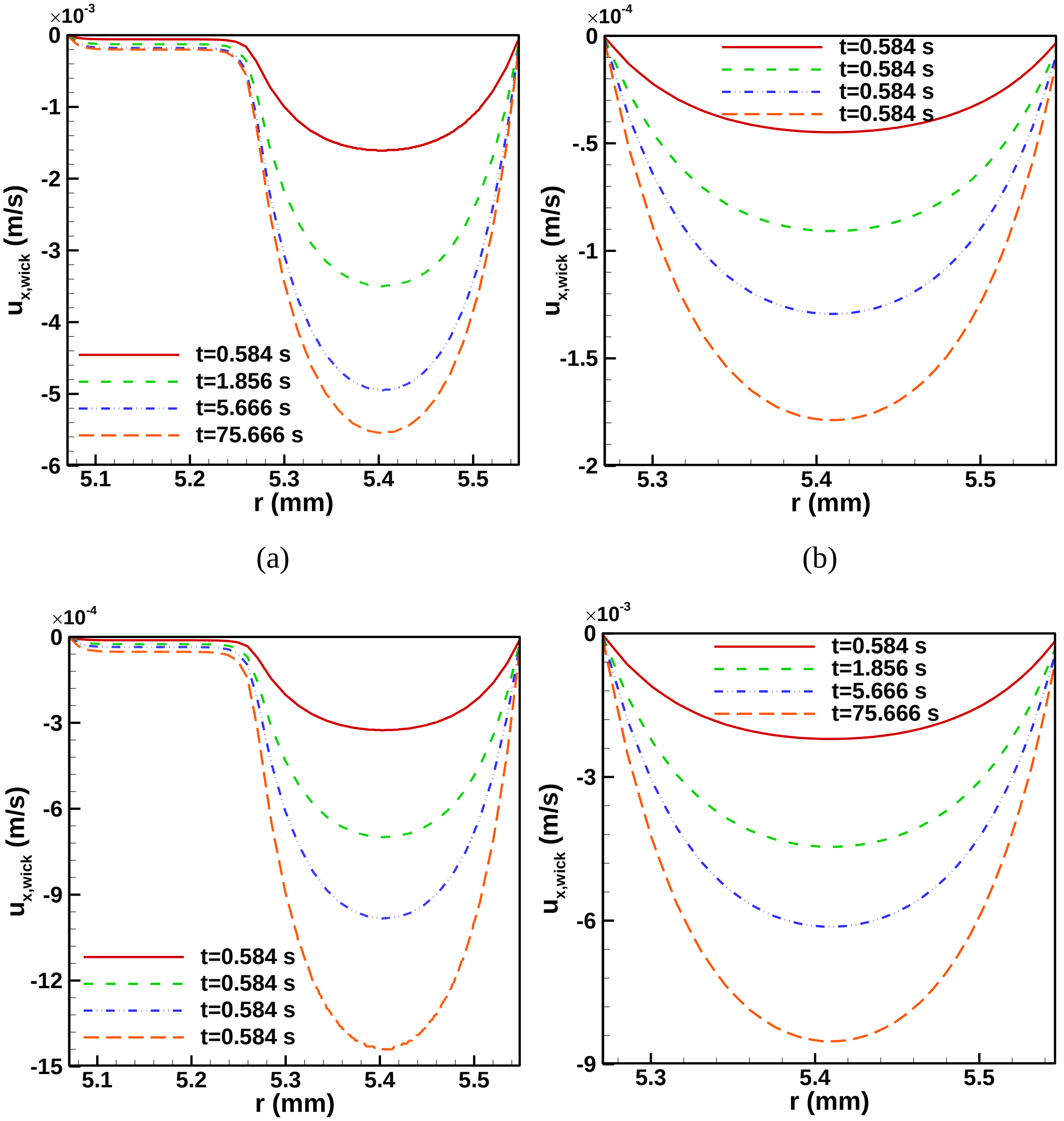

(a) (b)

(c) (d)

Figure 4.21 Axial velocity profiles at wick region (at x =0.16 m) for fully hybrid (b and d) and groove (a and c) heat pipes for Q = 30 W (a and b) and Q =150 W (c and d)

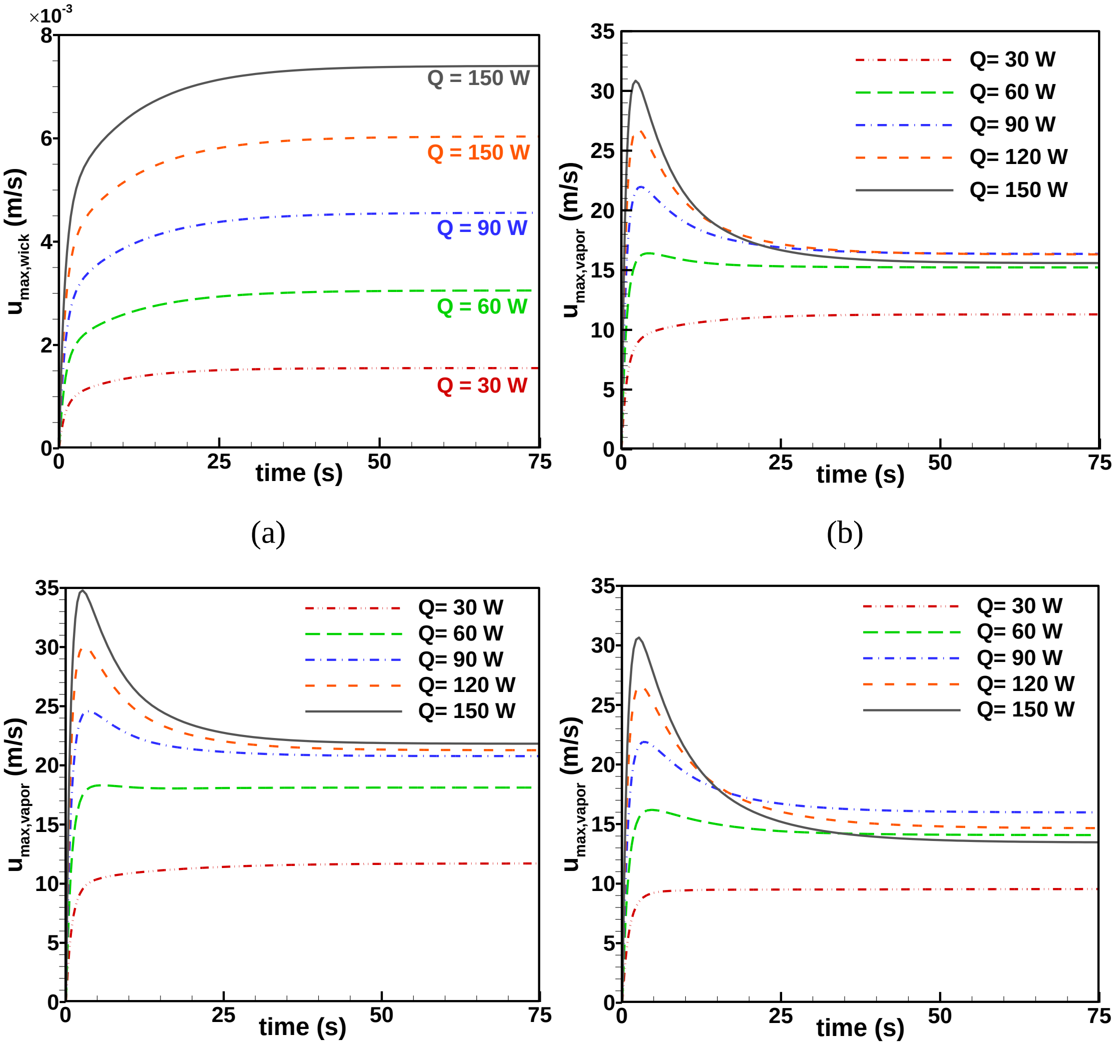

(a) (b)

(c) (d)

Figure 4.22 The maximum axial velocity of liquid for groove (a) and axial velocity of vapor for groove (b), fully hybrid (c) and partially hybrid (c) heat pipes for different heat inputs versus time

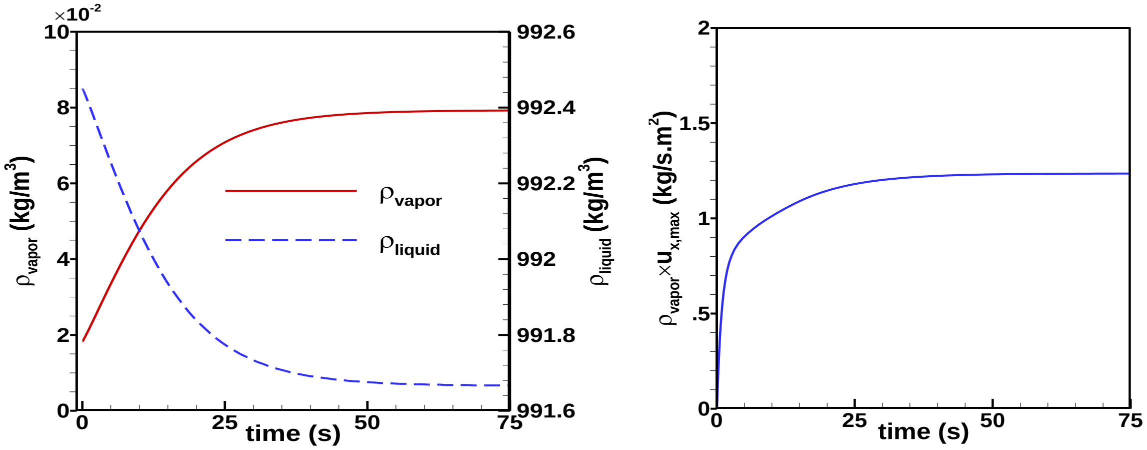

(a) (b)

Figure 4.23 (a) density of liquid and vapor vs. time (b) Product of average vapor density and maximum vapor velocity vs. time

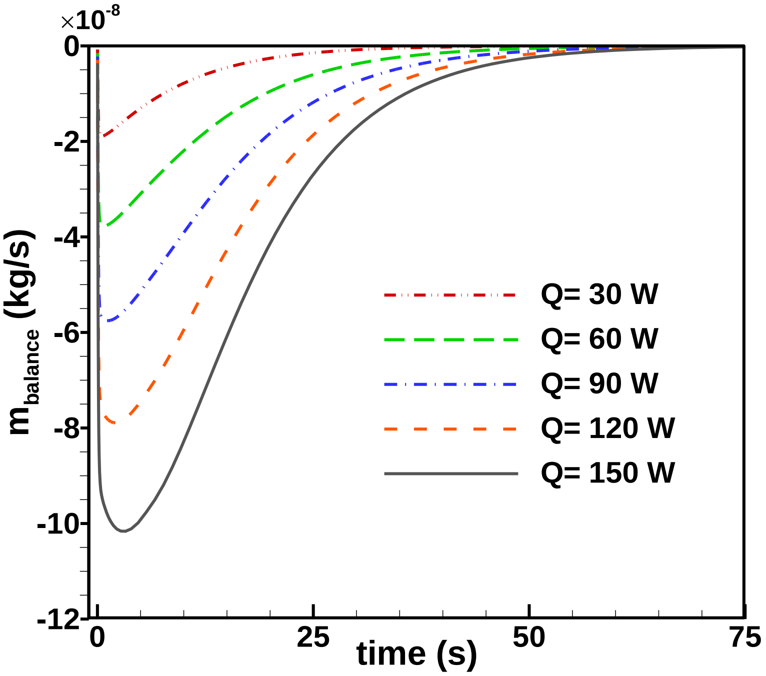

Figure 4.24 Mass transfer balance at the liquid-vapor interface (Eq. (2.28)) for groove heat pipe versus time for different heat inputs

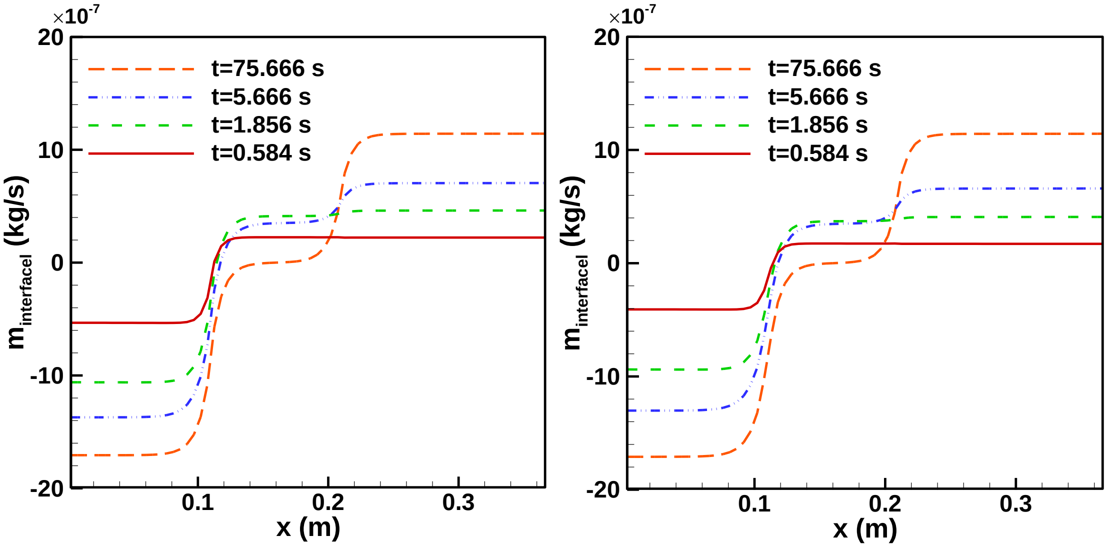

(a) (b)

Figure 4.25 Interfacial mass transfer for groove (a) and partially hybrid (b) heat pipes versus time for heat input Q = 90 W in different times

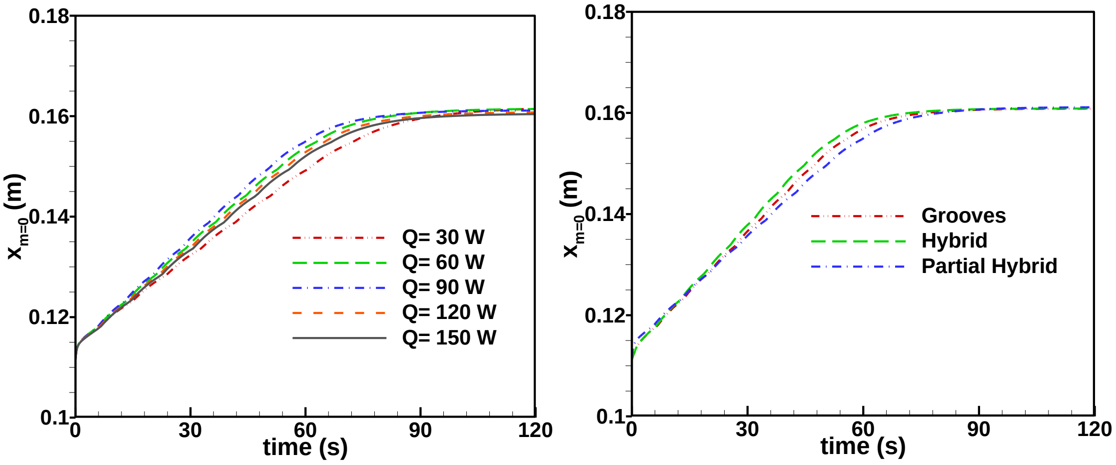

(a) (b)

Figure 4.26 The zero mass transfer point versus time for different heat inputs for hybrid heat pipe (a) and in heat pipes with different wick structure for Q =90 W (b)

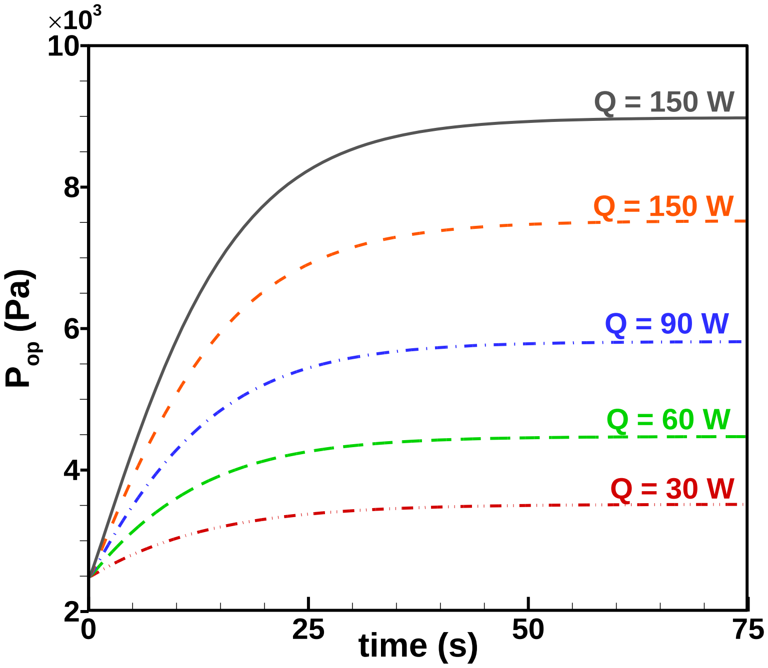

Figure 4.27 Operating pressure vs. time for different heat inputs

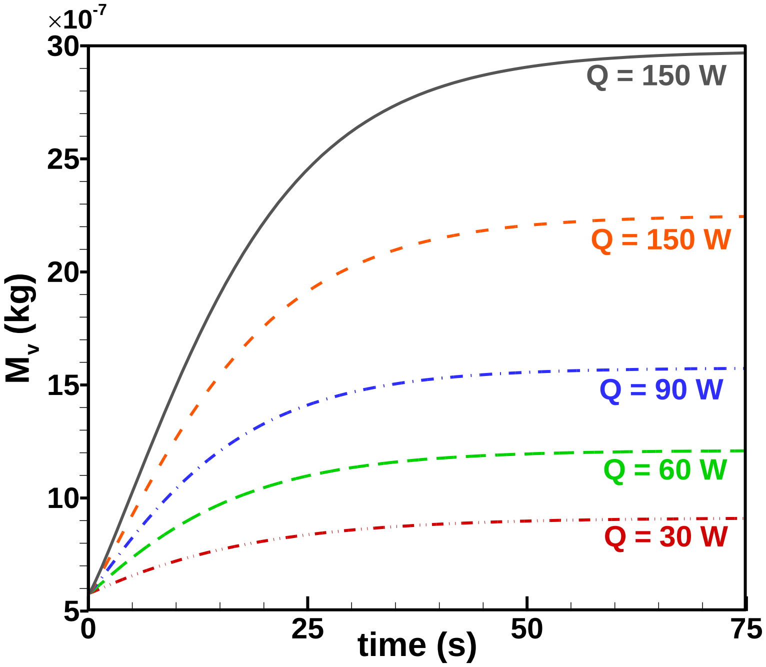

Figure 4.28 Mass of vapor vs. time for different heat inputs

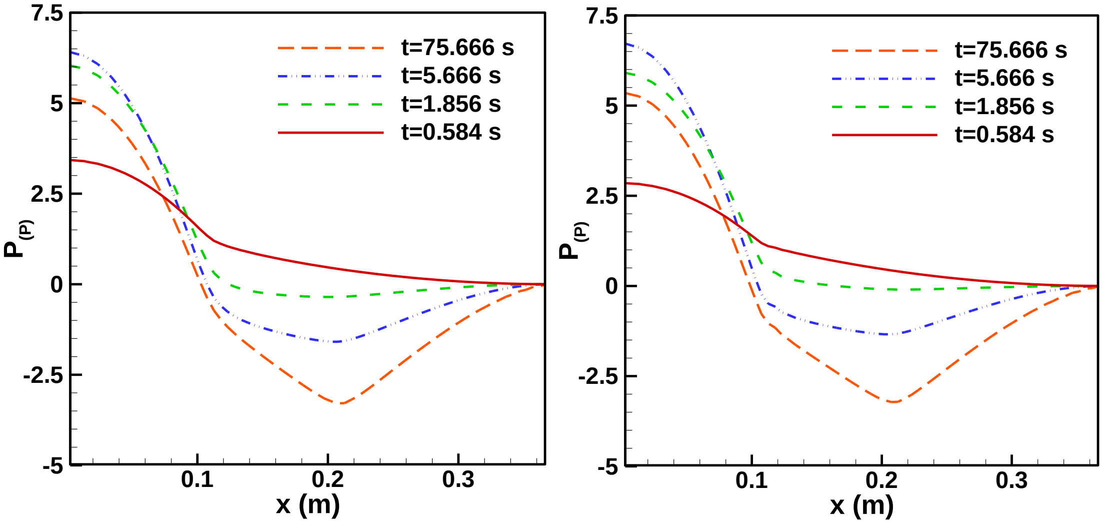

(a) (b)

Figure 4.29 Axial vapor pressure distributions along the liquid-vapor interface for groove (a) and (b) partially hybrid heat pipe in different times for *Q* =90 W

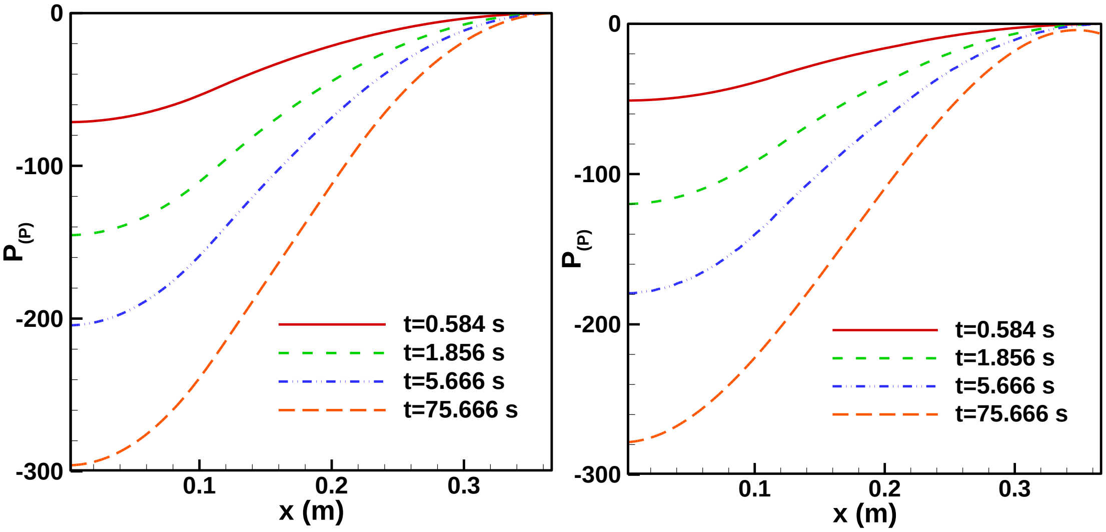

(a) (b)

Figure 4.30 Axial liquid pressure distributions along the liquid-vapor interface for groove (a) and (b) partially hybrid heat pipe in different times for *Q* =90 W

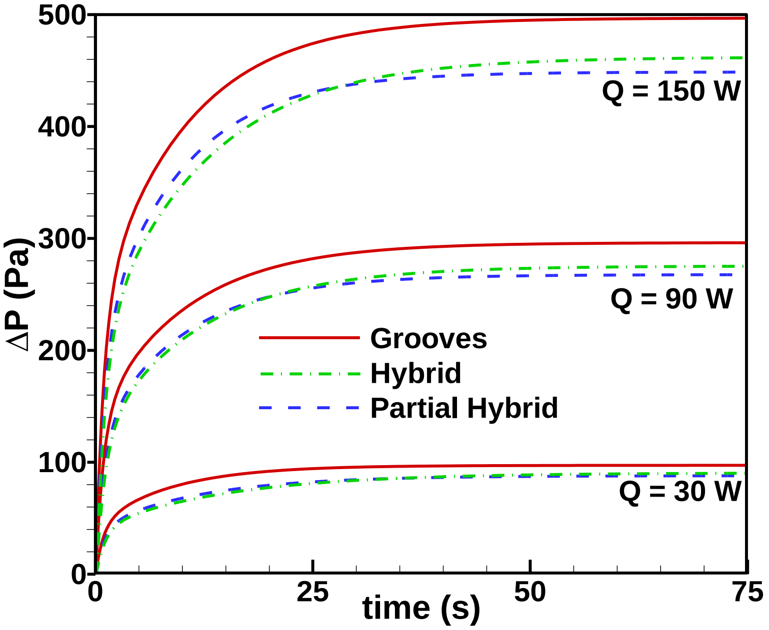

Figure 4.31 Transient liquid pressure drop for different wick structures and heat inputs

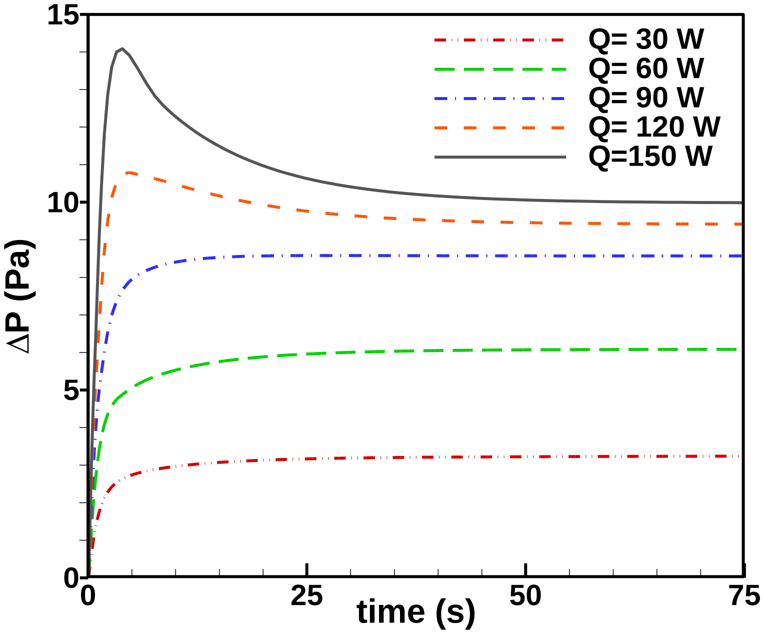

Figure 4.32 Transient vapor pressure drop for partilly haybrid heat pipe for different heat inputs

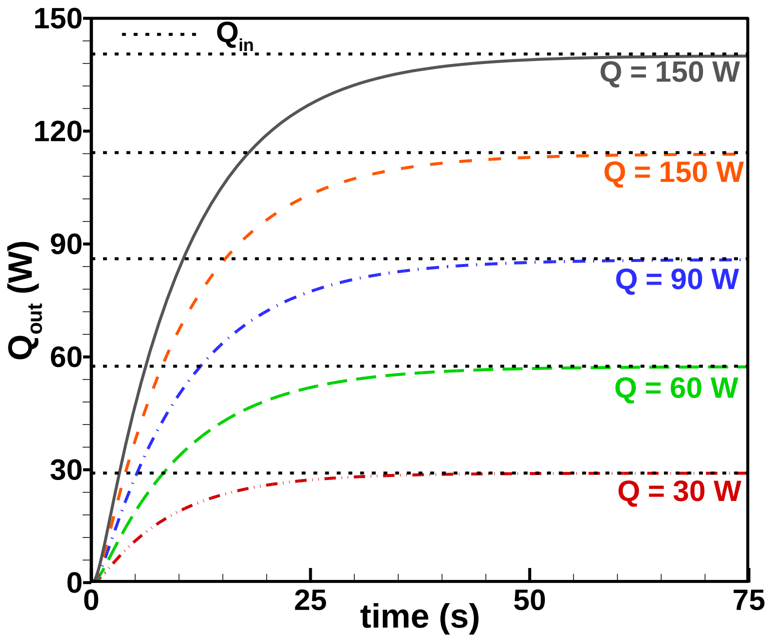

Figure 4.33 Dissipated heat from cooling section for groove heat pipe versus time for different heat inputs

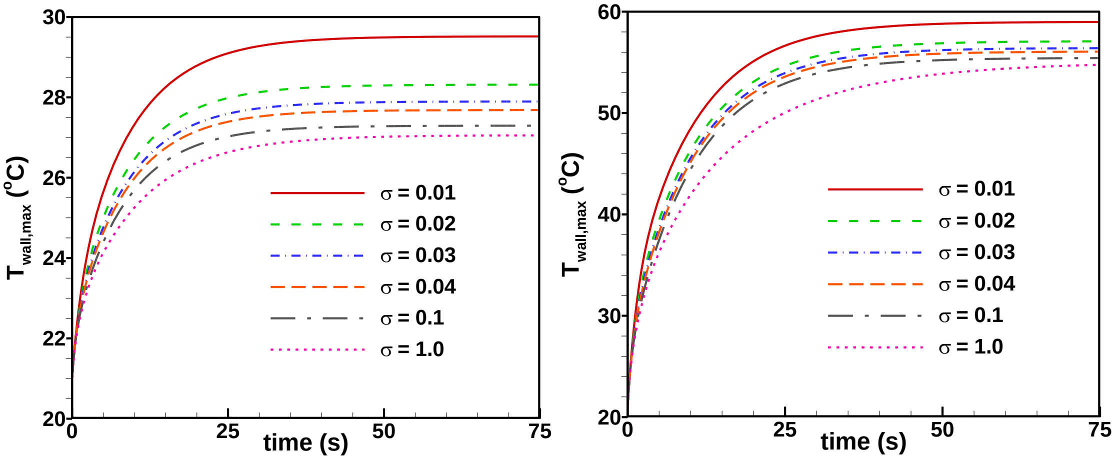

(a) (b)

Figure 4.34 Transient maximum wall temperature are depicted for *Q* =30 W (a) and *Q* = 150 W (b)

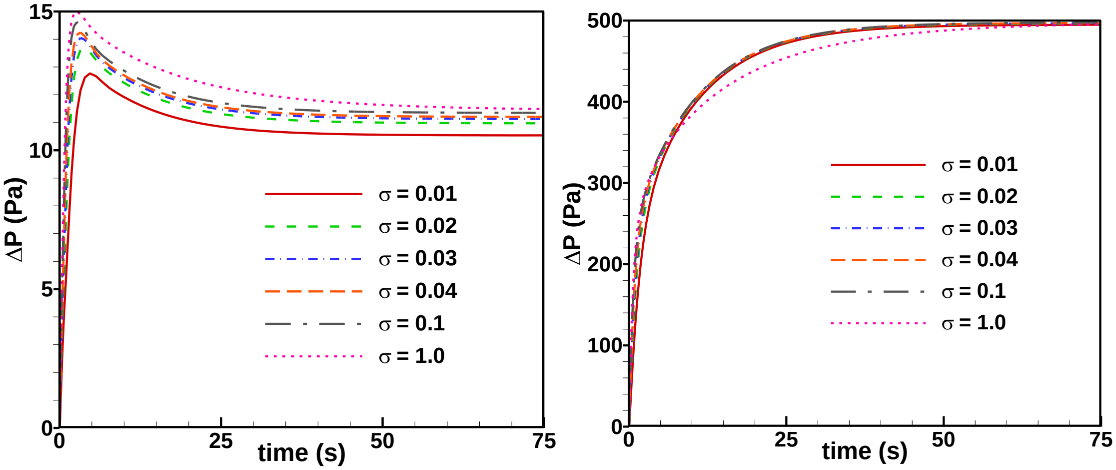

(a) (b)

Figure 4.35 Transient vapor (a) and liquid (b) pressure drops for different accommodation coefficients (*Q* =150 W)

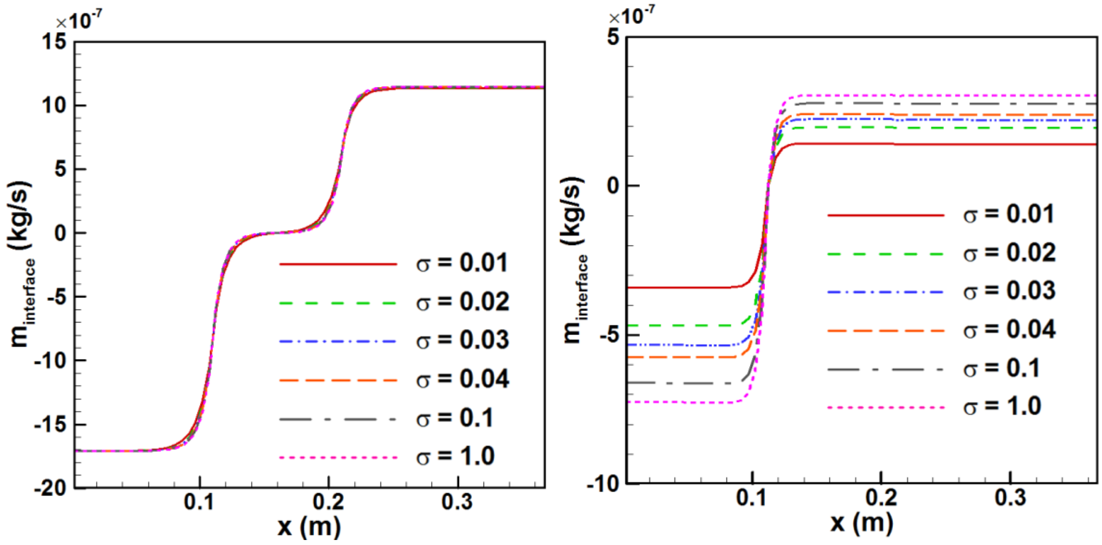

(a) (b)

Figure 4.36 Steady-state (a) and early *t* = 0.584 s (b) interfacial mass transfer profiles for *Q* =90 W.

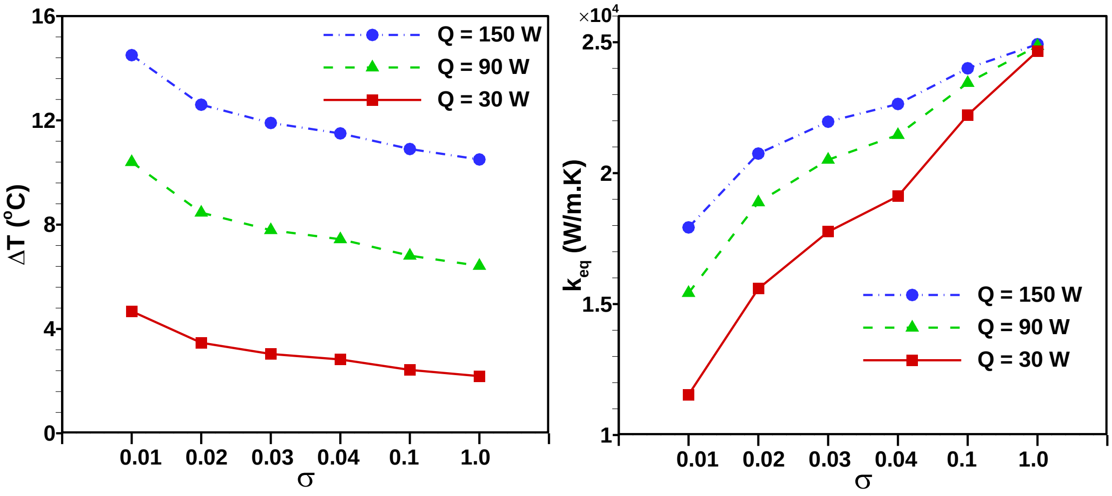

(a) (b)

Figure 4.37 Temperature difference (a) and equivalent thermal conductivity of heat pipe for different heat inputs and σ

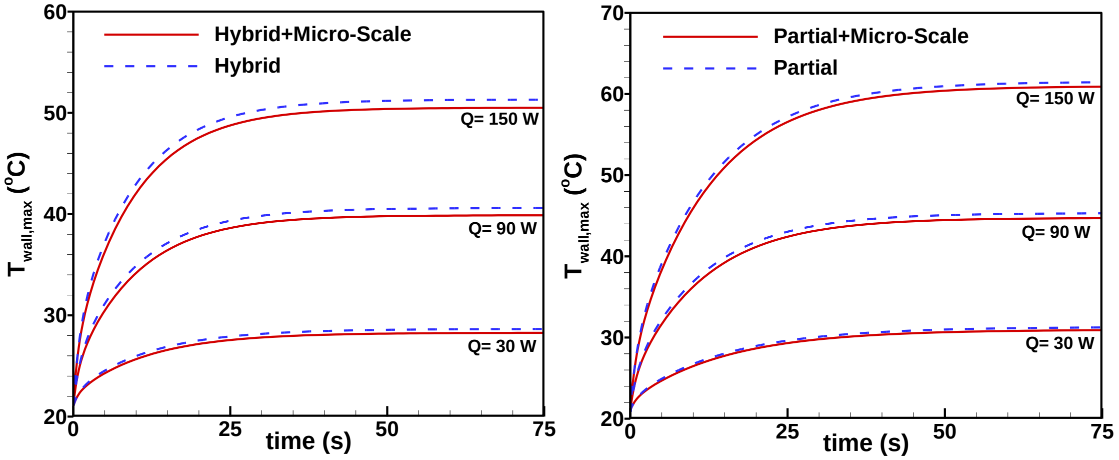

(a) (b)

Figure 4.38 Transient maximum wall temperature for different heat inputs with and without micro-scale effects for fully hybrid (a) and partial hybrid (b) heat pipe

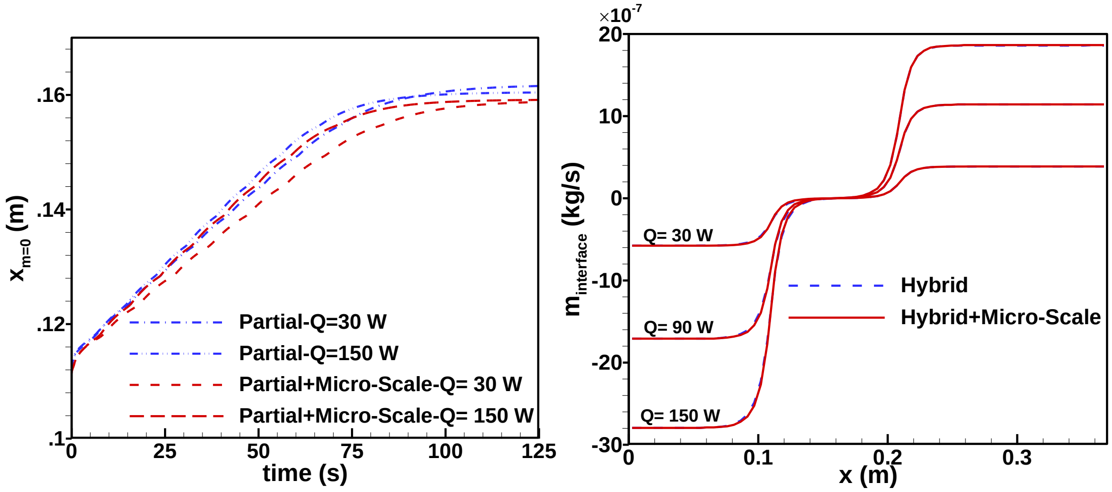

(a) (b)

Figure 4.39 Zero mass transfer point (b) and steady-state interfacial mass transfer (a) with and without micro-scale effects

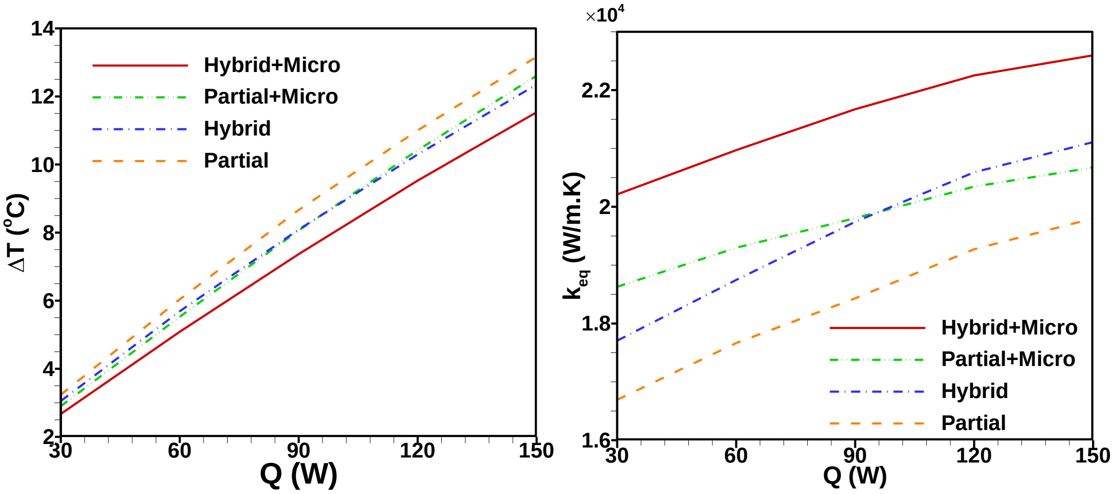

(a) (b)

Figure 4.40 Temperature difference (a) and equivalent thermal conductivity of heat pipe comparison with and without micro-scale effects

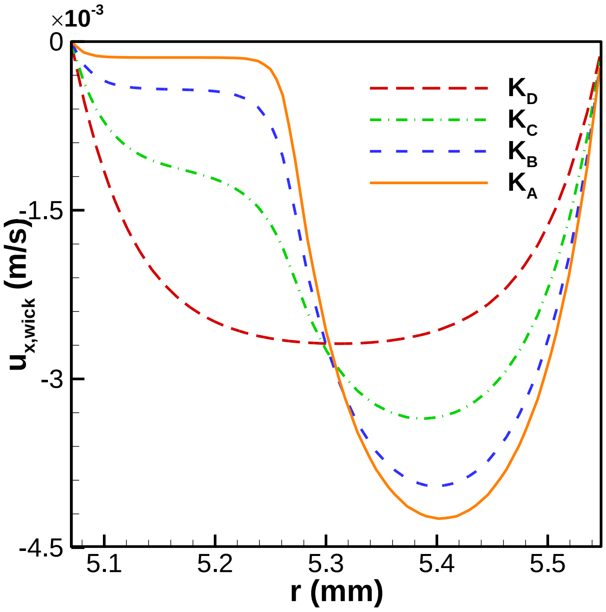

Figure 4.41 Liquid axial velocity profiles at $x_{m=0}$ =0.16 m for different cases as listed in Table 4.12

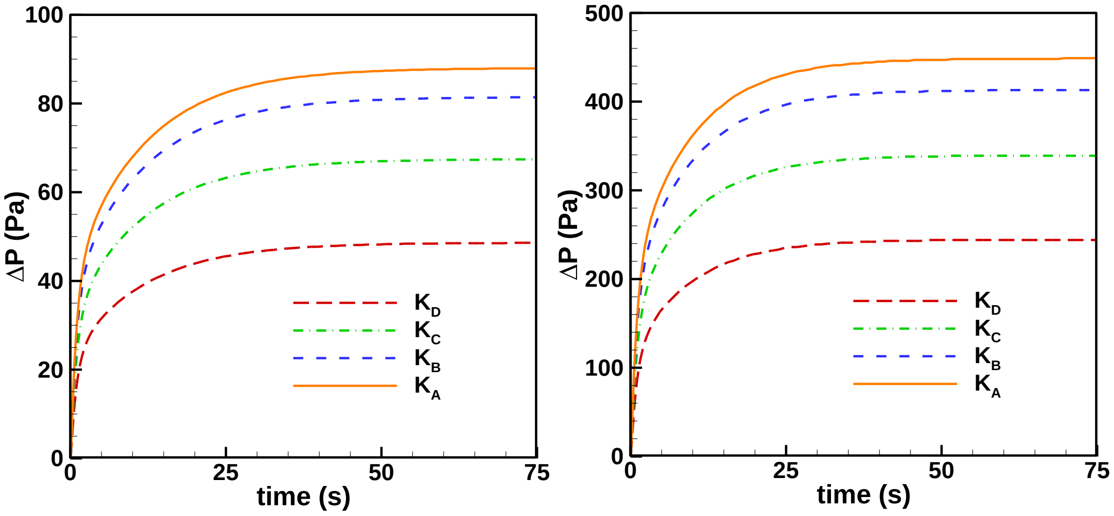

(a) (b)

Figure 4.42 Transient liquid pressure drops for different cases of permeability values for *Q* = 30 W (a) and *Q* = 150 W (b).

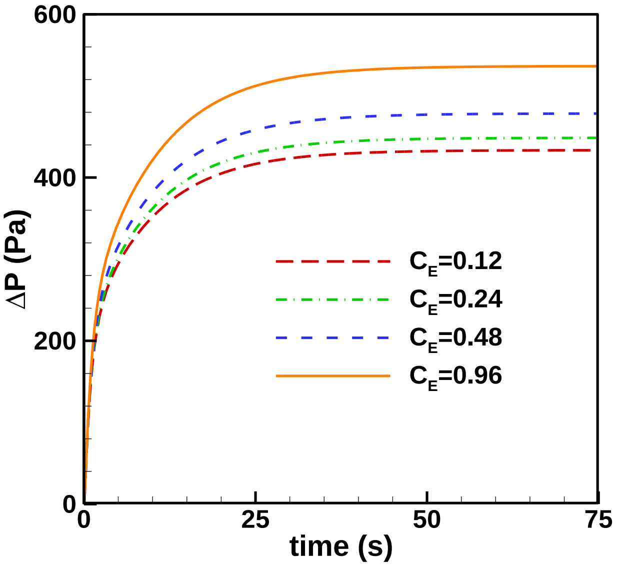

Figure 4.43 Transient liquid pressure drops for groove heat pipe with *Q* = 150 W

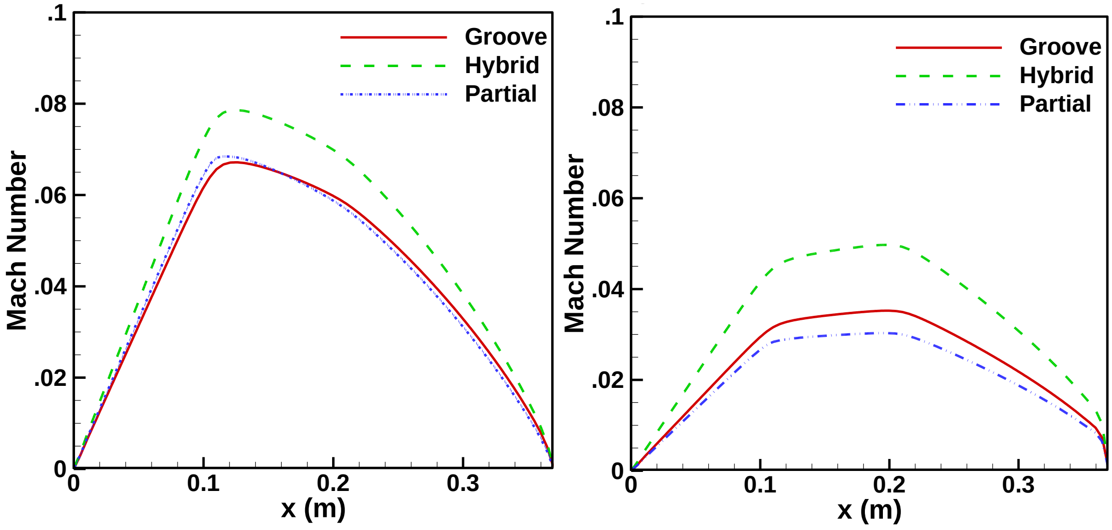

(a) (b)

Figure 4.44 Local Mach Number on the axisymmetric line for (a) *t* = 3.913 s and (b) *t* = 75.666 s

CHAPTER 5:
CONCLUSIONS AND RECOMMENDATIONS

5.1 Conclusions

A robust two-dimensional axisymmetric model is developed and used to simulate the transient and steady-state performance of cylindrical heat pipe with different wick structures. The presented model took into account the interface resistance, vapor hydrodynamic pressure, pressurization of the vapor core based on an incompressible flow assumption. The sensitivity of numerical procedure to the interfacial mass transfer is recognized and well overcome by reformulating the operating pressure and interfacial temperature. ANSYS Fluent software with the power of User Defined Functions and User Defined Scalars is used to apply the numerical procedure in coupled system and standard levels. The devised numerical method is shown to perform very well over a wide range of heat inputs, geometries, viscous and thermal properties. Also, the numerical procedure is very well validated against the previously published numerical, experimental, transient, steady-state, flat and cylindrical results.

The effective viscous and thermal properties of the groove and screen mesh wick structures are studied and computed based on different models and new models developed for permeability and thermal conductivity of the grooves. Based on these effective properties, the hybrid wick structure is molded non-homogenously for the first time in order to thoroughly investigate the unique roles of each wick structure. For the first time, non-parabolic axial velocity distributions are reported which is due to different values of permeability for grooves and screen mesh.

Three different wick structures of groove, fully hybrid and partial hybrid are studied and compared in terms of their thermal and viscous performances under a wide range of heat inputs. It is concluded that the groove heat pipe has the best thermal performance, however, the heat input cannot be increased since the dry-out is on the verge of happening based on the capillary limit comparison. On the other hand, fully and partial hybrid heat pipes stay well below the capillary limits and can handle much higher heat inputs compared to the groove heat pipe and fully hybrid heat pipes have slightly better thermal performance.

A comprehensive parameter study is carried out to illustrate effects of each parameter on thermal and viscous performance of cylindrical heat pipe with different wick structures. The capillary limits are checked based on the total pressure drop for all the heat pipes and it is concluded that dry-out would not happen in any of the case however, the groove heat pipe is getting close. It is concluded that, there is a cap for equivalent thermal conductivity of heat pipe if only the interface mass transfer is enhanced. Also, the importance of Ergun's coefficient is shown in pressure drop calculation which was previously neglected by many researchers. Moreover, the assumption of incompressible flow is checked by investigating the axial Mach Number for all the heat pipes.

5.2 Recommendations for Future Work

The present study does not include the micro-scale effects. It is assumed that liquid-vapor interface is flat with contact angle of 90°, however, the contact angle can be as small as 5° at the evaporation section. Including the liquid curvature at the liquid-vapor interface can enhance the thermal performance of the heat pipe. These micro-scale effects such as Marangoni convection, thin-film evaporation and contact angles are very important especially for a wick structure such as screen mesh.

The present model does not consider surface tension forces within the wick structure where liquid interact with the solid. With the advent of surface engineering and development of superhydrophilic and superhydrophobic surfaces, the surface tension need to be included in the heat pipe modeling for more accurate predictions.

In this study, the effective properties of each wick structure are homogenous and are not function of the direction. However, the properties of wick structure can be different in different direction. For instance, the pressure drop normal to screen mesh plane is different than the pressure drop along the plane which results in different permeability. Also, the thermal conductivity of the grooves are different in different directions. The directional properties of wick structures need to be calculated for more accurate prediction.

REFERENCES

[1] S.V. Garimella, C.B. Sobhan, Recent advances in the modeling and applications of nonconventional heat pipes, in: Advances in Heat Transfer, Elsevier, 2001, pp. 249-308.

[2] J. Rosenfeld, S. Zarembo, Final Report of Ultra-lightweight Magnesium Heat Pipes for Spacecraft Thermal Management, Thermacore International Inc, (2001).

[3] C. Hoa, B.t. Demolder, A. Alexandre, Roadmap for developing heat pipes for ALCATEL SPACE’s satellites, Applied thermal engineering, 23(9) (2003) 1099-1108.

[4] X. Chen, H. Ye, X. Fan, T. Ren, G. Zhang, A review of small heat pipes for electronics, Applied Thermal Engineering, 96 (2016) 1-17.

[5] Y. Chen, M. Groll, R. Mertz, Y.F. Maydanik, S. Vershinin, Steady-state and transient performance of a miniature loop heat pipe, in: ASME 3rd International Conference on Microchannels and Minichannels, American Society of Mechanical Engineers, 2005, pp. 183-189.

[6] X. Yang, Y. Yan, D. Mullen, Recent developments of lightweight, high performance heat pipes, Applied Thermal Engineering, 33 (2012) 1-14.

[7] S. Riffat, X. Zhao, A novel hybrid heat pipe solar collector/CHP system—Part 1: System design and construction, Renewable energy, 29(15) (2004) 2217-2233.

[8] S. Riffat, X. Zhao, A novel hybrid heat-pipe solar collector/CHP system—Part II: theoretical and experimental investigations, Renewable energy, 29(12) (2004) 1965-1990.

[9] A. Date, A. Date, C. Dixon, A. Akbarzadeh, Theoretical and experimental study on heat pipe cooled thermoelectric generators with water heating using concentrated solar thermal energy, Solar Energy, 105 (2014) 656-668.

[10] S. Riffat, X. Zhao, R. Boukhanouf, P. Doherty, Theoretical and experimental investigation of a novel hybrid heat-pipe solar collector, International journal of green energy, 1(4) (2005) 515-542.

[11] V.H. Gray, The rotating heat pipe-A wickless, hollow shaft for transferring high heat fluxes, (1969).

[12] V. Gray, Methods and apparatus for heat transfer in rotating bodies, in, Google Patents, 1974.

[13] T. Jen, G. Gutierrez, S. Eapen, G. Barber, H. Zhao, P. Szuba, J. Labataille, J. Manjunathaiah, Investigation of heat pipe cooling in drilling applications.: part I: preliminary numerical analysis and verification, International Journal of Machine Tools and Manufacture, 42(5) (2002) 643-652.

[14] L. Zhu, T.-C. Jen, C.-L. Yin, Y.-H. Yen, M. Zhu, J. Zhang, Investigation of Heat Pipe Cooling in Drilling Applications: Part 2—Thermal, Structural Static, and Dynamic Analyses, in: ASME 2009 International Mechanical Engineering Congress and Exposition, American Society of Mechanical Engineers, 2009, pp. 2027-2034.

[15] A. Faghri, Review and Advances in Heat Pipe Science and Technology, Journal of Heat Transfer-Transactions of the Asme, 134(12) (2012).

[16] T. Cotter, Principles and prospects for micro heat pipes, NASA STI/Recon Technical Report N, 84 (1984) 29149.

[17] G.P. Peterson, Overview of micro heat pipe research and development, Applied Mechanics Reviews, 45(5) (1992) 175-189.

[18] Y. Cao, A. Faghri, Micro/miniature heat pipes and operating limitations, Journal of Enhanced Heat Transfer, 1(3) (1994).

[19] R. Hopkins, A. Faghri, D. Khrustalev, Flat miniature heat pipes with micro capillary grooves, Journal of heat transfer, 121(1) (1999) 102-109.

[20] A. Faghri, Heat pipes: review, opportunities and challenges, Frontiers in Heat Pipes (FHP), 5(1) (2014).

[21] U. Vadakkan, Transient Three-Dimensional Modeling of Flat Heat Pipes with discrete Heat Sources, , PhD Dissertation, Purdue University, West Lafayette, Indiana, USA, 2004.

[22] G. Carbajal, Analysis of Passive Two-Phase Heat Dissipation Methodologies for High Heat Flux Impingement, PhD Dissertation, Rensselaer Polytechnic Institute, Troy, New York, USA, 2006.

[23] R. Ranjan, Two-Phase Heat and Mass Transfer in Capillary Porous Media, PhD Dissertation, Purdue University, West Lafayette, Indiana, USA, 2011.

[24] F. Issacci, Heat pipe vapor dynamics, University of California, Los Angeles, 1990.

[25] F. Simionescu, Considerations on Optimum Design of Micro Heat Pipe Sinks Using Water as Working Fluid, (2006).

[26] N. Sharifi, Comprehensive Numerical Modeling of Heat Pipe-Assisted Latent Heat Thermal Energy Storage Systems, (2014).

[27] A. Jiao, Modeling of thin film evaporation heat transfer and experimental investigation of miniature heat pipes, University of Missouri--Columbia, 2008.

[28] M.-M. Chen, A. Faghri, An analysis of the vapor flow and the heat conduction through the liquid-wick and pipe wall in a heat pipe with single or multiple heat sources, International journal of heat and mass transfer, 33(9) (1990) 1945-1955.

[29] S.S. Singh, Optimal micro heat pipe configuration on high performance heat spreaders, (2009).

[30] A. Faghri, Heat pipe science and technology, Heat Pipe Science and Technology, Washington, DC, 1995.

[31] J.Y.M. U. Vadakkan, S.V. Garimella, Transient analysis of flat heat pipes, in: Proceedings of the ASME Summer Heat Transfer Conference, Las Vegas, Nevada, USA, 2003, pp. 507-517.

[32] Z. Zuo, A. Faghri, A network thermodynamic analysis of the heat pipe, International Journal of Heat and Mass Transfer, 41(11) (1998) 1473-1484.

[33] H. Khalkhali, A. Faghri, Z. Zuo, Entropy generation in a heat pipe system, Applied Thermal Engineering, 19(10) (1999) 1027-1043.

[34] V.P. Carey, Liquid Vapor Phase Change Phenomena: An Introduction to the Thermophysics of Vaporization and Condensation Processes in Heat Transfer Equipment, Second Edition, Taylor & Francis, 2007.

[35] M. Aghvami, A. Faghri, Analysis of flat heat pipes with various heating and cooling configurations, Applied Thermal Engineering, 31(14-15) (2011) 2645-2655.

[36] H. Shabgard, A. Faghri, Performance characteristics of cylindrical heat pipes with multiple heat sources, Applied Thermal Engineering, 31(16) (2011) 3410-3419.

[37] K. Vafal, N. Zhu, W. Wang, Analysis of asymmetric disk-shaped and flat-plate heat pipes, Journal of heat transfer, 117(1) (1995) 209-218.

[38] N. Zhu, K. Vafai, Analysis of cylindrical heat pipes incorporating the effects of liquid–vapor coupling and non-Darcian transport—a closed form solution, International Journal of Heat and Mass Transfer, 42(18) (1999) 3405-3418.

[39] S. Harmand, R. Sonan, M. Fakes, H. Hassan, Transient cooling of electronic components by flat heat pipes, Applied Thermal Engineering, 31(11-12) (2011) 1877-1885.

[40] N. Pooyoo, S. Kumar, J. Charoensuk, A. Suksangpanomrung, Numerical simulation of cylindrical heat pipe considering non-Darcian transport for liquid flow inside wick and mass flow rate at liquid–vapor interface, International Journal of Heat and Mass Transfer, 70 (2014) 965-978.

[41] A. Nouri-Borujerdi, M. Layeghi, A numerical analysis of vapor flow in concentric annular heat pipes, Journal of fluids engineering, 126(3) (2004) 442-448.

[42] N. Thuchayapong, A. Nakano, P. Sakulchangsatjatai, P. Terdtoon, Effect of capillary pressure on performance of a heat pipe: Numerical approach with FEM, Applied Thermal Engineering, 32 (2012) 93-99.

[43] K. Vafai, W. Wang, Analysis of flow and heat transfer characteristics of an asymmetrical flat plate heat pipe, International Journal of Heat and Mass Transfer, 35(9) (1992) 2087-2099.

[44] M. Shafahi, V. Bianco, K. Vafai, O. Manca, An investigation of the thermal performance of cylindrical heat pipes using nanofluids, International journal of heat and mass transfer, 53(1) (2010) 376-383.

[45] M. Shafahi, V. Bianco, K. Vafai, O. Manca, Thermal performance of flat-shaped heat pipes using nanofluids, International Journal of Heat and Mass Transfer, 53(7) (2010) 1438-1445.

[46] L. Lu, H. Liao, X. Liu, Y. Tang, Numerical analysis on thermal hydraulic performance of a flat plate heat pipe with wick column, Heat and Mass Transfer, 51(8) (2015) 1051-1059.

[47] J. Legierski, B. Wie, G. De Mey, Measurements and simulations of transient characteristics of heat pipes, Microelectronics reliability, 46(1) (2006) 109-115.

[48] Y. Xuan, Y. Hong, Q. Li, Investigation on transient behaviors of flat plate heat pipes, Experimental Thermal and Fluid Science, 28(2) (2004) 249-255.

[49] A. Faghri, M. Buchko, Experimental and numerical analysis of low-temperature heat pipes with multiple heat sources, Journal of Heat Transfer, 113(3) (1991) 728-734.

[50] J.M. Tournier, M.S. El-Genk, A vapor flow model for analysis of liquid-metal heat pipe startup from a frozen state, International journal of heat and mass transfer, 39(18) (1996) 3767-3780.

[51] J.M. Tournier, M.S. El-Genk, ‘‘HPTAM’’ heat-pipe transient analysis model: an analysis of water heat pipes, AIP Conference Proceedings, 246(1) (1992) 1023-1037.

[52] J.-M. Tournier, M. El-Genk, A heat pipe transient analysis model, International Journal of Heat and Mass Transfer, 37(5) (1994) 753-762.

[53] J.-M. Tournier, M.S. El-Genk, Transient analysis of the start-up of a water heat pipe from a frozen state, Numerical Heat Transfer, Part A: Applications, 28(4) (1995) 461-486.

[54] Y. Cao, A. Faghri, Transient two-dimensional compressible analysis for high-temperature heat pipes with pulsed heat input, Numerical Heat Transfer, 18(4) (1991) 483-502.

[55] Y. Cao, A. Faghri, A numerical analysis of high-temperature heat pipe startup from the frozen state, Journal of heat transfer, 115(1) (1993) 247-254.

[56] F. Issacci, I. Catton, A. Heiss, N. Ghoniem, Analysis of heat pipe vapor dynamics, Chemical Engineering Communications, 85(1) (1989) 85-94.

[57] F. Issacci, I. Catton, N. Ghoniem, Vapor dynamics of heat pipe start-up, Journal of heat transfer, 113(4) (1991) 985-994.

[58] G. Carbajal, C.B. Sobhan, G.P. Peterson, Numerical study of heat pipe heat spreaders with large periodic heat input, J Thermophys Heat Tr, 20(4) (2006) 835-841.

[59] G. Carbajal, C.B. Sobhan, G.P.B. Peterson, D.T. Queheillalt, H.N.G. Wadley, A quasi-3D analysis of the thermal performance of a flat heat pipe, International Journal of Heat and Mass Transfer, 50(21-22) (2007) 4286-4296.

[60] U. Vadakkan, S.V. Garimella, J.Y. Murthy, Transport in flat heat pipes at high heat fluxes from multiple discrete sources, Journal of Heat Transfer-Transactions of the Asme, 126(3) (2004) 347-354.

[61] U. Vadakkan, S.V. Garimella, J.Y. Murthy, Prediction of Dryout in Flat Heat Pipes at High Heat Fluxes from Multiple Discrete Sources, in: ASME International Mechanical Engineering Congress, Washington D.C, USA, 2003 pp. 1-11.

[62] R. Ranjan, J.Y. Murthy, S.V. Garimella, U. Vadakkan, A numerical model for transport in flat heat pipes considering wick microstructure effects, International Journal of Heat and Mass Transfer, 54(1) (2011) 153-168.

[63] M. Famouri, G. Carbajal, C. Li, Transient analysis of heat transfer and fluid flow in a polymer-based Micro Flat Heat Pipe with hybrid wicks, International Journal of Heat and Mass Transfer, 70 (2014) 545-555.

[64] M. Famouri, M.M. Abdollahzadeh, A. Abdulshaheed, G. Huang, G. Carbajal, C. Li, Transient Analysis of a Cylindrical Heat Pipe Considering Different Wick Structures, in: ASME 2016 Heat Transfer Summer Conference collocated with the ASME 2016 Fluids Engineering Division Summer Meeting and the ASME 2016 14th International Conference on Nanochannels, Microchannels, and Minichannels, American Society of Mechanical Engineers, 2016, pp. V002T008A023-V002T008A023.

[65] R. Ranjan, J.Y. Murthy, S.V. Garimella, U. Vadakkan, A numerical model for transport in flat heat pipes considering wick microstructure effects, International Journal of Heat and Mass Transfer, 54(1-3) (2011) 153-168.

[66] S.V.G. Ram Ranjan Jayathi Y. Murthy, Unnikrishnan Vadakkan, A Numerical Model For Transport In Heat Pipes Considering Wick Microstructure Effects, in: Thermal and Thermomechanical Phenomena in Electronic Systems (ITherm), 12th IEEE Intersociety Conference, Las vegas, Nevada, USA, 2010, pp. 1-10.

[67] A.B. Solomon, K. Ramachandran, L.G. Asirvatham, B. Pillai, Numerical analysis of a screen mesh wick heat pipe with Cu/water nanofluid, International Journal of Heat and Mass Transfer, 75 (2014) 523-533.

[68] L.T. X. Dai, F. Yang, B. Shi, R. Yang, Y.C. Lee, C. Li, Characterization of Hybrid-Wicked Copper Heat Pipe, in: ASME Conference Proceedings, (38921) T30005, Atlanta, Georgia, USA, 2011.

[69] X. Dai, M. Famouri, A.I. Abdulagatov, R. Yang, Y.-C. Lee, S.M. George, C. Li, Capillary evaporation on micromembrane-enhanced microchannel wicks with atomic layer deposited silica, Applied Physics Letters, 103(15) (2013) 151602.

[70] X. Dai, F. Yang, R. Yang, Y.-C. Lee, C. Li, Micromembrane-enhanced capillary evaporation, International Journal of Heat and Mass Transfer, 64 (2013) 1101-1108.

[71] G.A. Huang, Ahmed; Chang,Wei; Li,Chen, An Evaluation of Hybrid Wick Design on High Performance Copper-Ethanol Heat Pipes, in: Joint 18th IHPC and 12th IHPS, Jeju, Korea, 2016.

[72] C. Oshman, B. Shi, C. Li, R. Yang, Y.C. Lee, G.P. Peterson, V.M. Bright, The Development of Polymer-Based Flat Heat Pipes, Journal of Microelectromechanical Systems, 20(2) (2011) 410-417.

[73] T. Cotter, Theory of heat pipes, DTIC Document, 1965.

[74] C. Bankston, H. Smith, Vapor flow in cylindrical heat pipes, Journal of Heat Transfer, 95(3) (1973) 371-376.

[75] H.v. Ooijen, C. Hoogendoorn, Vapor flow calculations in a flat-plate heat pipe, AIAA Journal, 17(11) (1979) 1251-1259.

[76] P. Bystrov, V. Goncharov, Starting dynamics of high-temperature gas-filled heat pipes, High Temperature Science, 21 (1984) 927-936.

[77] F.A. Costello, A.F. Montague, M.A. Merrigan, Detailed transient model of a liquid-metal heat pipe, Costello (FA), Inc., Herndon, VA (USA); Los Alamos National Lab., NM (USA); General Electric Co., Philadelphia, PA (USA), 1986.

[78] J. Ambrose, L. Chow, J. Beam, Transient heat pipe response and rewetting behavior, J Thermophys Heat Tr, 1(3) (1987) 222-227.

[79] J.H. Jang, A. Faghri, W.S. Chang, Analysis of the one-dimensional transient compressible vapor flow in heat pipes, International journal of heat and mass transfer, 34(8) (1991) 2029-2037.

[80] A. Faghri, C. Harley, Transient lumped heat pipe analyses, Heat Recovery Systems and CHP, 14(4) (1994) 351-363.

[81] F. Lefevre, M. Lallemand, Coupled thermal and hydrodynamic models of flat micro heat pipes for the cooling of multiple electronic components, International Journal of Heat and Mass Transfer, 49(7) (2006) 1375-1383.

[82] R. Sonan, S. Harmand, J. Pellé, D. Leger, M. Fakès, Transient thermal and hydrodynamic model of flat heat pipe for the cooling of electronics components, International Journal of Heat and Mass Transfer, 51(25) (2008) 6006-6017.

[83] M. Arab, A. Abbas, A model-based approach for analysis of working fluids in heat pipes, Applied Thermal Engineering, 73(1) (2014) 751-763.

[84] A. Faghri, S. Thomas, Performance characteristics of a concentric annular heat pipe. I-Experimental prediction and analysis of the capillary limit. II-Vapor flow analysis, in: ASME 1988 National Heat Transfer Conference, Volume 1, 1988, pp. 379-387.

[85] A. Faghri, S. Thomas, Performance characteristics of a concentric annular heat pipe: Part I—Experimental prediction and analysis of the capillary limit, Journal of heat transfer, 111(4) (1989) 844-850.

[86] J. Schmalhofer, A. Faghri, A study of circumferentially-heated and block-heated heat pipes—I. Experimental analysis and generalized analytical prediction of capillary limits, International journal of heat and mass transfer, 36(1) (1993) 201-212.

[87] J. Schmalhofer, A. Faghri, A study of circumferentially-heated and block-heated heat pipes—II. Three-dimensional numerical modeling as a conjugate problem, International journal of heat and mass transfer, 36(1) (1993) 213-226.

[88] A. Faghri, M. Buchko, Y. Cao, A study of high-temperature heat pipes with multiple heat sources and sinks: Part I—Experimental methodology and frozen startup profiles, Journal of heat transfer, 113(4) (1991) 1003-1009.

[89] A. Faghri, M. Buchko, Y. Cao, A Study of High-Temperature Heat Pipes With Multiple Heat Sources and Sinks: Part II—Analysis of Continuum Transient and Steady-State Experimental Data With Numerical Predictions, Journal of heat transfer, 113(4) (1991) 1010-1016.

[90] C. Harley, A. Faghri, Transient two-dimensional gas-loaded heat pipe analysis, Journal of heat transfer, 116(3) (1994) 716-723.

[91] J.M. Tournier, M.S. El-Genk, Segregated Solution Technique For Simulating The Transient Operation Of Heat Pipes, Numerical Heat Transfer, Part B: Fundamentals, 25(3) (1994) 331-355.

[92] L. Huang, M. El-Genk, J.-M. Tournier, Transient performance of an inclined water heat pipe with a screen wick, ASME-PUBLICATIONS-HTD, 236 (1993) 87-87.

[93] G. Carbajal, C.B. Sobhan, G.P. Peterson, D.T. Queheillalt, H.N.G. Wadley, Thermal response of a flat heat pipe sandwich structure to a localized heat flux, International Journal of Heat and Mass Transfer, 49(21-22) (2006) 4070-4081.

[94] M. Layeghi, A. Nouri-Borujerdi, Vapor flow analysis in partially-heated concentric annular heat pipes, International Journal of Computational Engineering Science, 5(01) (2004) 235-244.

[95] A. Nouri-Borujerdi, M. Layeghi, Liquid Flow Analysis in Concentric Annular Heat Pipes Wicks, Journal Of Porous Media, 8(5) (2005) 471.

[96] Y. Koito, H. Imura, M. Mochizuki, Y. Saito, S. Torii, Numerical analysis and experimental verification on thermal fluid phenomena in a vapor chamber, Applied Thermal Engineering, 26(14) (2006) 1669-1676.

[97] Y.-S. Chen, K.-H. Chien, C.-C. Wang, T.-C. Hung, B.-S. Pei, A simplified transient three-dimensional model for estimating the thermal performance of the vapor chambers, Applied thermal engineering, 26(17) (2006) 2087-2094.

[98] T. Kaya, J. Goldak, Three-dimensional numerical analysis of heat and mass transfer in heat pipes, Heat and Mass Transfer, 43(8) (2007) 775-785.

[99] L. Bai, The FEM Analysis of a Heat Pipe, Carleton University, Carleton University, 2004.

[100] R. Ranjan, J.Y. Murthy, S.V. Garimella, A microscale model for thin-film evaporation in capillary wick structures, International Journal of Heat and Mass Transfer, 54(1) (2011) 169-179.

[101] R. Ranjan, J.Y. Murthy, S.V. Garimella, U. Vadakkan, A numerical model for transport in heat pipes considering wick microstructure effects, in: Thermal and Thermomechanical Phenomena in Electronic Systems (ITherm), 2010 12th IEEE Intersociety Conference on, IEEE, 2010, pp. 1-10.

[102] Y.-S. Chen, K.-H. Chien, T.-C. Hung, C.-C. Wang, Y.-M. Ferng, B.-S. Pei, Numerical simulation of a heat sink embedded with a vapor chamber and calculation of effective thermal conductivity of a vapor chamber, Applied Thermal Engineering, 29(13) (2009) 2655-2664.

[103] S.V. Patankar, Numerical Heat transfer and Fluid Flow, McGraw-Hill, Ney York, USA, 1980.

[104] R. Ranjan, A. Patel, S.V. Garimella, J.Y. Murthy, Wicking and thermal characteristics of micropillared structures for use in passive heat spreaders, International Journal of Heat and Mass Transfer, 55(4) (2012) 586-596.

[105] K.H. Do, S.J. Kim, S.V. Garimella, A mathematical model for analyzing the thermal characteristics of a flat micro heat pipe with a grooved wick, International Journal of Heat and Mass Transfer, 51(19-20) (2008) 4637-4650.

[106] D. Khrustalev, A. Faghri, Heat transfer during evaporation on capillary-grooved structures of heat pipes, Journal of Heat Transfer, 117(3) (1995) 740-747.

[107] B. Suman, Modeling, experiment, and fabrication of micro-grooved heat pipes: An update, Applied Mechanics Reviews, 60(1-6) (2007) 107-119.

[108] X. Xu, V. Carey, Film evaporation from a micro-grooved surface-An approximate heat transfer model and its comparison with experimental data, J Thermophys Heat Tr, 4(4) (1990) 512-520.

[109] K.H. Do, H.J. Ha, S.P. Jang, Thermal resistance of screen mesh wick heat pipes using the water-based Al 2 O 3 nanofluids, International Journal of Heat and Mass Transfer, 53(25) (2010) 5888-5894.

[110] F. Lefèvre, J.-B. Conrardy, M. Raynaud, J. Bonjour, Experimental investigations of flat plate heat pipes with screen meshes or grooves covered with screen meshes as capillary structure, Applied Thermal Engineering, 37 (2012) 95-102.

[111] Z. Zhao, Y. Peles, M.K. Jensen, Properties of plain weave metallic wire mesh screens, International Journal of Heat and Mass Transfer, 57(2) (2013) 690-697.

[112] C. Li, G.P. Peterson, Evaporation/boiling in thin capillary wicks (II) - Effects of volumetric porosity and mesh size, Journal of Heat Transfer-Transactions of the Asme, 128(12) (2006) 1320-1328.

[113] C. Li, G.P. Peterson, The effective thermal conductivity of wire screen, International Journal of Heat and Mass Transfer, 49(21-22) (2006) 4095-4105.

[114] C. Li, G.P. Peterson, Y. Wang, Evaporation/boiling in thin capillary wicks (I) - Wick thickness effects, Journal of Heat Transfer-Transactions of the Asme, 128(12) (2006) 1312-1319.

[115] C.J. Morris, F.K. Forster, Oscillatory flow in microchannels, Experiments in Fluids, 36(6) (2004) 928-937.

[116] B.S. C. Oshman, A. Abdulagatov, S. George, R.G. Yang, Y.C. Lee, V.M. Bright, C. Li, Fabrication And Testing Of An Ald Tio2 Coated Flat Polymer Micro Heat Pipe, in: 15th International Heat Pipe Conference (15th IHPC), Clemson, USA, 2010.

[117] S. Maalej, M. Zaghdoudi, Experimental and theoretical analysis on enhanced flat miniature heat pipes with axial capillary grooves and screen meshes, in: 2007 International Conference on Thermal Issues in Emerging Technologies: Theory and Application, IEEE, 2007, pp. 21-32.

[118] J. Rice, A. Faghri, Analysis of screen wick heat pipes, including capillary dry-out limitations, J Thermophys Heat Tr, 21(3) (2007) 475-486.

[119] W.S. Chang, Porosity and effective thermal conductivity of wire screens, Journal of heat transfer, 112(1) (1990) 5-9.

[120] B.D. Marcus, Theory and design of variable conductance heat pipes, (1972).

[121] J.C. Armour, J.N. Cannon, Fluid flow through woven screens, AIChE Journal, 14(3) (1968) 415-420.

[122] J. Xu, R.A. Wirtz, In-plane effective thermal conductivity of plain-weave screen laminates, IEEE Transactions on components and packaging technologies, 25(4) (2002) 615-620.

[123] L. Rayleigh, LVI. On the influence of obstacles arranged in rectangular order upon the properties of a medium, The London, Edinburgh, and Dublin Philosophical Magazine and Journal of Science, 34(211) (1892) 481-502.

[124] B. Xiao, A. Faghri, A three-dimensional thermal-fluid analysis of flat heat pipes, International Journal of Heat and Mass Transfer, 51(11-12) (2008) 3113-3126.

[125] A. Bhattacharya, V. Calmidi, R. Mahajan, Thermophysical properties of high porosity metal foams, International Journal of Heat and Mass Transfer, 45(5) (2002) 1017-1031.

[126] C. Yang, A. Nakayama, A synthesis of tortuosity and dispersion in effective thermal conductivity of porous media, International Journal of Heat and Mass Transfer, 53(15) (2010) 3222-3230.

[127] J.K. Carson, S.J. Lovatt, D.J. Tanner, A.C. Cleland, Thermal conductivity bounds for isotropic, porous materials, International Journal of Heat and Mass Transfer, 48(11) (2005) 2150-2158.

[128] A. Driss, S. Maalej, M.C. Zaghdoudi, Experimentation and modeling of the steady-state and transient thermal performances of a helicoidally grooved cylindrical heat pipe, Microelectronics Reliability, (2016).

[129] N. Wakao, K. Kato, Effective thermal conductivity of packed beds, Journal of Chemical Engineering of Japan, 2(1) (1969) 24-33.

[130] J. Wang, J.K. Carson, M.F. North, D.J. Cleland, A new approach to modelling the effective thermal conductivity of heterogeneous materials, International journal of heat and mass transfer, 49(17) (2006) 3075-3083.

[131] C. Hsu, K. Wong, P. Cheng, Effective stagnant thermal conductivity of wire screens, J Thermophys Heat Tr, 10(3) (1996) 542-545.

[132] E. Alexander Jr, Structure--property relationships in heat pipe wicking materials, (1972).

[133] J. Koh, A. Fortini, Prediction of thermal conductivity and electrical resistivity of porous metallic materials, International Journal of Heat and Mass Transfer, 16(11) (1973) 2013-2022.

[134] M. Aivazov, I. Domashnev, Influence of porosity on the conductivity of hot-pressed titanium-nitride specimens, Powder Metallurgy and Metal Ceramics, 7(9) (1968) 708-710.

[135] R. Tye, An experimental investigation of the thermal conductivity and electrical resistivity of three porous 304L stainless steel ‘Rigimesh’material to 1300 K, NASA CR, 72710 (1970).

[136] D.A. Nield, A. Bejan, Convection in porous media, Springer Science & Business Media, 2006.

[137] S.K. Thomas, R.C. Lykins, K.L. Yerkes, Fully developed laminar flow in trapezoidal grooves with shear stress at the liquid–vapor interface, International Journal of Heat and Mass Transfer, 44(18) (2001) 3397-3412.

[138] S.J. Kim, J.K. Seo, K.H. Do, Analytical and experimental investigation on the operational characteristics and the thermal optimization of a miniature heat pipe with a grooved wick structure, International Journal of Heat and Mass Transfer, 46(11) (2003) 2051-2063.

[139] R. Shah, Laminar flow friction and forced convection heat transfer in ducts of arbitrary geometry, International Journal of Heat and Mass Transfer, 18(7-8) (1975) 849-862.

[140] D. Joseph, D. Nield, G. Papanicolaou, Nonlinear equation governing flow in a saturated porous medium, Water Resour. Res, 18(4) (1982) 1049-1052.

[141] S. Irmay, On the theoretical derivation of Darcy and Forchheimer formulas, Eos, Transactions American Geophysical Union, 39(4) (1958) 702-707.

[142] S. Ergun, A.A. Orning, Fluid flow through randomly packed columns and fluidized beds, Industrial & Engineering Chemistry, 41(6) (1949) 1179-1184.

[143] H. Kozai, H. Imura, Y. Ikeda, The permeability of screen wicks, JSME international journal. Ser. 2, Fluids engineering, heat transfer, power, combustion, thermophysical properties, 34(2) (1991) 212-219.

[144] H. Noda, K. Yoshioka, T. Hamatake, An Experimental Study on the Permeability of Screen Wicks, JSME International Journal Series B Fluids and Thermal Engineering, 36(2) (1993) 357-363.

[145] Y. IKEDA, Permeability of a screen wick, The Institute of Space and Astronautical Science report. SP, 3 (1985) 119-125.

[146] M. Balhoff, A. Mikelić, M.F. Wheeler, Polynomial filtration laws for low Reynolds number flows through porous media, Transport in Porous Media, 81(1) (2010) 35-60.

[147] R. Barree, M. Conway, Beyond beta factors: a complete model for Darcy, Forchheimer, and trans-Forchheimer flow in porous media, in: SPE annual technical conference and exhibition, Society of Petroleum Engineers, 2004.

[148] A.s. Montillet, Flow through a finite packed bed of spheres: a note on the limit of applicability of the Forchheimer-type equation, Journal of fluids engineering, 126(1) (2004) 139-143.

[149] ANSYS Fluent, ANSYS Fluent Theory Guide, ANSYS Inc., USA, (2015).

[150] ANSYS Fluent, 12.0 User's guide, ANSYS Inc., USA, (2015).

[151] ANSYS Fluent, ANSYS Fluent UDF Manual, ANSYS Inc., USA, (2015).

[152] R. Marek, J. Straub, Analysis of the evaporation coefficient and the condensation coefficient of water, International Journal of Heat and Mass Transfer, 44(1) (2001) 39-53.

[153] G.O. Rubel, J.W. Gentry, Measurement of the kinetics of solution droplets in the presence of adsorbed monolayers: Determination of water accommodation coefficients, The Journal of Physical Chemistry, 88(14) (1984) 3142-3148.

[154] I. Eames, N. Marr, H. Sabir, The evaporation coefficient of water: a review, International Journal of Heat and Mass Transfer, 40(12) (1997) 2963-2973.

[155] A. Mills, R. Seban, The condensation coefficient of water, International Journal of Heat and Mass Transfer, 10(12) (1967) 1815-1827.

[156] S.P. Sukhatme, W.M. Rohsenow, Heat transfer during film condensation of a liquid metal vapor, Journal of Heat Transfer, 88(1) (1966) 19-27.

[157] B. Paul, Compilation of evaporation coefficients, ARS Journal, 32(9) (1962) 1321-1328.

[158] B. Xiao, A. Faghri, A three-dimensional thermal-fluid analysis of flat heat pipes, International Journal of Heat and Mass Transfer, 51(11) (2008) 3113-3126.

[159] M. Ghajar, J. Darabi, N. Crews Jr, A hybrid CFD-mathematical model for simulation of a MEMS loop heat pipe for electronics cooling applications, Journal of Micromechanics and Microengineering, 15(2) (2004) 313.

[160] Y. Chen, C. Zhang, M. Shi, J. Wu, G. Peterson, Study on flow and heat transfer characteristics of heat pipe with axial "Ω"-shaped microgrooves, International Journal of Heat and Mass Transfer, 52(3) (2009) 636-643.

[161] S. Chi, Heat pipe theory and practice: A Sourcebook, (1976).

APPENDIX A – THE UDFS CODE

The following is the UDFs code complied in ANSYS Fluent:

```
/*****************************************************************
******** PROGRAM:                                        ********
********      USER DEFINED FUNCTIONS                     ********
********      TRANSIENT PERFORMANCE OF HEAT PIPE         ********
******** DEVELOPED BY:                                   ********
********      MEHDI FAMOURI (FAMOUR@GMAIL.COM)           ********
********      MICRO/NANOSCALE TRANSPORT LAB              ********
********      MECHANICAL ENGINEERING DEPARTMENT          ********
********      THE UNIVERSITY OF SOUTH CAROLINA           ********
********              FALL OF 2016                       ********
*****************************************************************/
#include "udf.h"
#include "math.h"
#include "sg_udms.h"
#include "sg.h"
#include "stdio.h"
#include "mem.h"
#include "dpm.h"
#include "surf.h"
double TOTAL_LENGHT;
double xx, xx_shadow;
double HEAT_FLUX, HTC, TEMP_COOLING;
double HFG, ZIGMA;
double MOLAR_MASS, PI_num, R_UNIVERSAL, R_R;
double T_REF, P_REF,TEMP_INITIAL;
double P_OP_1, P_OP_2, M_DOT_BALANCE;
double MASS_VAPOR1, MASS_VAPOR2, MASS_LIQUID_1, MASS_LIQUID_2;
double POROSITY, WICK_VOLUME, LIQUID_DENSITY_INITIAL;
double CP_L,CP_S,RO_L,RO_S;
double Y_WICK_1,Y_WICK_2,Y_WICK_3,Y_WICK_4;
double K_WICK_1,K_WICK_2,K_WICK_3;
double D_WICK_1,D_WICK_2,D_WICK_3;
double POROSITY1,POROSITY2,POROSITY3;
double VISCOUS_RES_1,VISCOUS_RES_2,VISCOUS_RES_3;
double INERTIAL_RES_1,INERTIAL_RES_2,INERTIAL_RES_3;
double PRESSURE_INTERFACE,PRESSURE_VAPOR_0;
```

```
double PRESSURE_VAPOR, P_VAPOR_MIN, PRESSURE_WICK_MAX,
PRESSURE_WICK_MIN;
double URF_VEL, URF_TEMP;
double VEL_MAX_V_VAPOR,VEL_MAX_U_VAPOR,VEL_MAX_U_WICK,
double X_SEPARATION,X_VEL_MAX_U_VAPOR,X_VEL_MAX_U_WICK
double TEMP_WALL_MAX,TEMP_WALL_MIN;
double Q_VAPOR,Q_VAPOR_E,Q_VAPOR_C,Q_WICK,Q_OUT,Q_IN;
double DENSITY_VAPOR,DENSITY_VAPOR_E,DENSITY_VAPOR_C;
double DENSITY_VAPOR_MAX,DENSITY_VAPOR_MIN, LIQUID_DENSITY;
double M_DOT[1000],VEL_INTERFACE_VAPOR[1000];
double VEL_INTERFACE_WICK[1000],TEMP_INTERFACE[1000];
double TIME_STEP
double aa1,aa2,aa3,aa4=0.0;
double bb1,bb2,bb3,bb4=0.0;
double x[ND_ND];
double A[ND_ND],es[ND_ND],A_by_Es,dr0[ND_ND], ds;
double As[ND_ND],ess[ND_ND],A_by_Ess,dr0s[ND_ND], ds_shadow;
double temp_Cell, temp_Cell_shadow;
double temp_face, temp_face_shadow;
double k_Cell, k_Cell_shadow;
double ro_Cell, ro_Cell_shadow;
double cp_Cell, cp_Cell_shadow;
double P_Cell, P_Cell_shadow;
double v_face, v_face_shadow;
double k_ds; k_ds_shadow;
int iii_WICK_VAPOR[1000],iii_VAPOR_WICK[1000];
int zone_ID, N_ITERATION,N_TIME
int N_print,N_print_time,N_print_iter,iii,jjj,i,j;
int MARZ_WICK_VAPOR_ID=189;
int MARZ_VAPOR_WICK_ID=187;
int MARZ_WALL_WICK_ID=215;
int MARZ_WICK_WALL_ID=213;
int WALL_heating_ID=220;
int WALL_insulated_ID=219;
int WALL_Cooling_ID=218;
int VAPOR_Core_ID=8;
int WICK_Core_ID=14;
int WALL_ID=56;
Domain *dd;
face_t ff, ff_shadow;
Thread *tt, *t0, *t0_shadow, *tt_shadow;
cell_t c0, cell_t c0_shadow;
face_t ff_WALL_WICK [1000];
face_t ff_WICK_WALL [1000];
face_t ff_WICK_VAPOR [1000];
face_t ff_VAPOR_WICK [1000];
```

```
/*****************************************************************
******** THIS UDF IS USED TO INITIALIZE THE PARAMETERS *******
*****************************************************************/
DEFINE_INIT(INITIAL_SETTINGS, domain)
{
        FILE *fp0;
        FILE *fp1;
        FILE *fp2;
        fp0 = fopen ("Data_0Transient.txt", "w");
        fp1 = fopen ("Data_1Interface.txt", "w");
        fp2 = fopen ("Data_2WALL.txt", "w");
        fprintf (fp0,"TIME          P_OP_2          TEMP_WALL_MAX
TEMP_WALL_MIN     Vap_MAX_VEL     Q_OUT          Q_IN          Q_VAPOR
Q_VAPOR_E      Q_VAPOR_C       M_DOT_BALANCE     MASS_VAPOR2
MASS_LIQUID_2          VEL_MAX_inte    WICK_MAX_VEL    X_SEPARATION
x_MAX_U_VAPOR   x_MAX_U_WICK    P_drop_VAPOR
P_droPRESSURE_WICK      DENSITY_VAPOR       DENSITY_VAPOR_E
DENSITY_VAPOR_C      DENSITY_VAPOR_MAX    DENSITY_VAPOR_MIN\n");
        fclose (fp0);
        fclose (fp1);
        fclose (fp2);
        //=====================================
        zone_ID = MARZ_WALL_WICK_ID;
        tt = Lookup_Thread(domain,zone_ID);
        begin_f_loop (ff,tt)
        {
                c0 = F_C0(ff,tt);
                t0= F_C0_THREAD(ff,tt);
                RO_S=C_R_M1(c0,t0);
                CP_S=C_CP(c0,t0);
        }
        end_f_loop (ff,tt)
                bb4=bb4;
        //=====================================
        zone_ID = MARZ_WICK_WALL_ID;
        tt = Lookup_Thread(domain,zone_ID);
        begin_f_loop (ff,tt)
        {
                c0 = F_C0(ff,tt);
                t0= F_C0_THREAD(ff,tt);
                RO_L=C_R_M1(c0,t0);
                CP_L=C_CP(c0,t0);
        }
        end_f_loop (ff,tt)
                bb4=bb4;
        TOTAL_LENGHT=0.370;
```

```
//HEAT_FLUX=17.42084554;   //Q=30
//HEAT_FLUX=34.39316262;   //Q=60
//HEAT_FLUX=51.48508728;   //Q=90
//HEAT_FLUX=68.35573791;   //Q=120
HEAT_FLUX=84.03031263;   //Q=150
//HTC=1175.87;    //Q=30
//HTC=927.25;    //Q=30
//HTC=905.09;    //Q=30
//HTC=919.03;    //Q=30
HTC=928.83;   //Q=150
TEMP_COOLING=21+273.15;
TEMP_INITIAL=TEMP_COOLING;
HFG=2406*1.0E3;
ZIGMA=0.03;
MOLAR_MASS=18.015;
PI_num=3.141592653589;
R_UNIVERSAL=8314.40;
R_R=R_UNIVERSAL/MOLAR_MASS;
LIQUID_DENSITY_INITIAL=992.45;
//======================================
Y_WICK_1=(5.55)*0.001;
Y_WICK_2=(5.55-0.28)*0.001;
Y_WICK_3=(5.55-0.280-0.2)*0.001;
Y_WICK_4=(5.55-0.280-0.2-0.1)*0.001;
K_WICK_1=1.72;
K_WICK_2=62.507;
K_WICK_3=62.507;
D_WICK_1=K_WICK_1/CP_L;
D_WICK_2=K_WICK_2/CP_L;
D_WICK_3=K_WICK_3/CP_L;
POROSITY1=0.713;
POROSITY2=0.707;
POROSITY3=0.707;
VISCOUS_RES_1=3.331E+08;
VISCOUS_RES_2=1.161E+10;
VISCOUS_RES_3=1.161E+10;
INERTIAL_RES_1=8.663E+03;
INERTIAL_RES_2=5.178E+04;
INERTIAL_RES_3=5.178E+04;
//======================================
P_OP_1=2490;
P_REF=P_OP_1;
T_REF=TEMP_INITIAL;
P_REF=P_OP_1;
URF_VEL=0.1;
URF_TEMP=0.1;
```

```
N_ITERATION=0;
N_TIME=1;
N_print=1;
N_print_time=1;
N_print_iter=100;
PRESSURE_VAPOR_0=0.0;
//=====================================
thread_loop_C (t0,domain)
{
        begin_C_loop_all (c0,t0)
        {
                C_UDSI(c0,t0,0)=TEMP_INITIAL;
        }
        end_C_loop_all (c0,t0)
}
//=====================================
zone_ID = VAPOR_Core_ID;
t0 = Lookup_Thread(domain,zone_ID);
aa1=0.0;
iii=0;
begin_C_loop (c0,t0)
{
        iii=iii+1;
        C_CENTROID(x,c0,t0);
        aa1=aa1+C_VOLUME(c0,t0)/C_UDSI(c0,t0,0);
}
end_C_loop (c0,t0)
        bb4=bb4;
MASS_VAPOR1=aa1*P_OP_1/R_R;
//=====================================
zone_ID = WICK_Core_ID;
t0 = Lookup_Thread(domain,zone_ID);
WICK_VOLUME=0.0;
begin_C_loop (c0,t0)
{
        C_CENTROID(x,c0,t0);
        if ((x[1] <= Y_WICK_1) && (x[1] >= Y_WICK_2))
        {

WICK_VOLUME=WICK_VOLUME+C_VOLUME(c0,t0)*POROSITY1;
        }
        else if ((x[1] < Y_WICK_2) && (x[1] >= Y_WICK_3))
        {

WICK_VOLUME=WICK_VOLUME+C_VOLUME(c0,t0)*POROSITY2;
        }
```

```
			else
			{

		WICK_VOLUME=WICK_VOLUME+C_VOLUME(c0,t0)*POROSITY3;
			}
		}
		end_C_loop (c0,t0)
			bb4=bb4;
		MASS_LIQUID_1=LIQUID_DENSITY_INITIAL*WICK_VOLUME;
		//======================================
		P_OP_2=P_OP_1;
		MASS_VAPOR2=MASS_VAPOR1;
		MASS_LIQUID_2=MASS_LIQUID_1;
		iii=0;
		while (iii<1000)
		{
			M_DOT[iii]=0;
			TEMP_INTERFACE[iii]=TEMP_INITIAL;
			VEL_INTERFACE_VAPOR[iii]=0.0;
			VEL_INTERFACE_WICK[iii]=0.0;
			iii=iii+1;
		}
		Message("P_OP=%e   MASS_VAPOR=%e   MASS_LIQUID=%e
\n",P_OP_1,MASS_VAPOR1,MASS_LIQUID_1);
}
/*************************************************************
********   THIS UDF IS USED TO READ FACES AND THREADS  ********
********   OF THE NEIGHBOR CELLS IN DIFFERENT DOMAINS********
********   AND SAVE THEM TO BE USED IN OTHER UDFS        ********
*************************************************************/
DEFINE_INIT(SHADOW_READING, domain)
{
		zone_ID = MARZ_WALL_WICK_ID;
		tt= Lookup_Thread(domain,zone_ID);
		zone_ID = MARZ_WICK_WALL_ID;
		tt_shadow = Lookup_Thread(domain,zone_ID);
		iii=-1;
		begin_f_loop(ff, tt)
		{
			iii=iii+1;
			F_CENTROID(x,ff,tt);
			xx = x[0];
			jjj=-1;
			begin_f_loop(ff_shadow, tt_shadow)
			{
				jjj=jjj+1;
```

```
                F_CENTROID(x,ff_shadow, tt_shadow);
                xx_shadow = x[0];
                if (fabs((xx_shadow-xx)/TOTAL_LENGHT) < 1.0E-6)
                {
                        ff_WALL_WICK [iii]=ff_shadow;
                }
        }
        end_f_loop(ff_shadow, tt_shadow)
}
end_f_loop(ff, tt)
        bb4=bb4;
//=====================================
zone_ID = MARZ_WICK_WALL_ID;
tt= Lookup_Thread(domain,zone_ID);
zone_ID = MARZ_WALL_WICK_ID;
tt_shadow = Lookup_Thread(domain,zone_ID);
iii=-1;
begin_f_loop(ff, tt)
{
        iii=iii+1;
        F_CENTROID(x,ff,tt);
        xx = x[0];
        begin_f_loop(ff_shadow, tt_shadow)
        {
                F_CENTROID(x,ff_shadow, tt_shadow);
                xx_shadow = x[0];

                if (fabs((xx_shadow-xx)/TOTAL_LENGHT) < 1.0E-6)
                {
                        ff_WICK_WALL [iii]=ff_shadow;
                }
        }
        end_f_loop(ff_shadow, tt_shadow)
}
end_f_loop(ff, tt)
        bb4=bb4;
//=====================================
//=====================================
zone_ID = MARZ_WICK_VAPOR_ID;
tt= Lookup_Thread(domain,zone_ID);
zone_ID = MARZ_VAPOR_WICK_ID;
tt_shadow = Lookup_Thread(domain,zone_ID);
iii=-1;
begin_f_loop(ff, tt)
{
        iii=iii+1;
```

```
        F_CENTROID(x,ff,tt);
        xx = x[0];
        jjj=-1;
        begin_f_loop(ff_shadow, tt_shadow)
        {
                jjj=jjj+1;
                F_CENTROID(x,ff_shadow, tt_shadow);
                xx_shadow = x[0];
                if (fabs((xx_shadow-xx)/TOTAL_LENGHT) < 1.0E-6)
                {
                        ff_WICK_VAPOR [iii]=ff_shadow;
                        iii_WICK_VAPOR[jjj]=iii;
                }
        }
        end_f_loop(ff_shadow, tt_shadow)
}
end_f_loop(ff, tt)
        bb4=bb4;
//=====================================
zone_ID = MARZ_VAPOR_WICK_ID;
tt= Lookup_Thread(domain,zone_ID);
zone_ID = MARZ_WICK_VAPOR_ID;
tt_shadow = Lookup_Thread(domain,zone_ID);
iii=-1;
begin_f_loop(ff, tt)
{
        iii=iii+1;
        F_CENTROID(x,ff,tt);
        xx = x[0];
        jjj=-1;
        begin_f_loop(ff_shadow, tt_shadow)
        {
                jjj=jjj+1;
                F_CENTROID(x,ff_shadow, tt_shadow);
                xx_shadow = x[0];

                if (fabs((xx_shadow-xx)/TOTAL_LENGHT) < 1.0E-6)
                {
                        ff_VAPOR_WICK [iii]=ff_shadow;
                        iii_VAPOR_WICK[jjj]=iii;
                }
        }
        end_f_loop(ff_shadow, tt_shadow)
}
end_f_loop(ff, tt)
        bb4=bb4;
```

```
}
/**************************************************************
********  THIS UDF IS USED TO CALCULATE AND UPDATE      ********
********  THE SYSTEM LEVEL PARAMETERS SUCH AS P_OP    ********
**************************************************************/
DEFINE_ADJUST(PARAMETERS_UPDATE, domain)
{
        FILE *fp;
        double P_OP_2_old,P_OP_2_new;
        double AAA,BBB,CCC,DDD;
        double NV_VEC(f_area);
        double d_area;
        TIME_STEP=CURRENT_TIMESTEP;
        N_ITERATION=N_ITERATION+1;
   //====================================
        tt = Lookup_Thread(domain,zone_ID);
        aa1=0.0;
        iii=-1;
        begin_f_loop (ff,tt)
        {
                iii=iii+1;
                c0 = F_C0(ff,tt);
                t0= F_C0_THREAD(ff,tt);
                v_face =F_V(ff,tt);
                ro_Cell=C_R(c0,t0);
                F_AREA(f_area,ff,tt);
                d_area = NV_MAG(f_area);
                aa1=aa1+v_face*ro_Cell*d_area;
        }
        end_f_loop (ff,tt)
                bb4=bb4;
        M_DOT_BALANCE=aa1;
        MASS_VAPOR2=MASS_VAPOR1-TIME_STEP*(aa1);
        MASS_LIQUID_2=MASS_LIQUID_1+TIME_STEP*(aa1);
        //================================================
        zone_ID = VAPOR_Core_ID;
        t0 = Lookup_Thread(domain,zone_ID);
        aa1=0.0;
        begin_C_loop (c0,t0)
        {
                aa1=aa1+C_VOLUME(c0,t0)/C_UDSI(c0,t0,0);
        }
        end_C_loop (c0,t0)
                bb4=bb4;
        P_OP_2_old=MASS_VAPOR2/(aa1/R_R);
        BBB=R_R/aa1;
```

```
    zone_ID = MARZ_VAPOR_WICK_ID;
    tt = Lookup_Thread(domain,zone_ID);
    CCC=0.0;
    DDD=0.0;
    iii=-1;
    begin_f_loop (ff,tt)
    {
        iii=iii+1;
        c0 = F_C0(ff,tt);
        t0= F_C0_THREAD(ff,tt);
        v_face = F_V(ff,tt);
        ro_Cell=C_R(c0,t0);
        temp_Cell=C_UDSI(c0,t0,0);
        temp_face=TEMP_INTERFACE [iii];
        PRESSURE_INTERFACE=P_REF*exp(HFG/R_R*(1.0/T_REF-
1.0/temp_face));
        P_Cell=C_P(c0,t0)-PRESSURE_VAPOR_0;
        F_AREA(f_area,ff,tt);
        d_area = NV_MAG(f_area);
        CCC=CCC+d_area*(P_Cell/sqrt(temp_Cell)-
PRESSURE_INTERFACE/sqrt(temp_face));
        DDD=DDD+d_area*(1/sqrt(temp_Cell));
    }
    end_f_loop (ff,tt)
        bb4=bb4;
    AAA=(2.0*ZIGMA/(2.0-ZIGMA))*(1/sqrt(2*PI_num*R_R));
    P_OP_2_new=(BBB*(MASS_VAPOR1-
TIME_STEP*AAA*CCC))/(1+BBB*TIME_STEP*AAA*DDD);
}
/****************************************************************
********   THIS UDF IS USED TO CALCULATE AND UPDATE     ********
********   THE INTERFACIAL TEMPERATURE AND VELOCITY ********
****************************************************************/
DEFINE_ADJUST(WICK_VAPOR_INTERFACE, domain)
{
    zone_ID = MARZ_VAPOR_WICK_ID;
    tt = Lookup_Thread(domain,zone_ID);
    zone_ID = MARZ_WICK_VAPOR_ID;
    tt_shadow = Lookup_Thread(domain,zone_ID);
    iii=-1;
    begin_f_loop(ff, tt)
    {
        iii=iii+1;
        F_CENTROID(x,ff,tt);
        xx = x[0];
        ff_shadow=ff_VAPOR_WICK [iii];
```

```
                c0 = F_C0(ff,tt);
                t0 = F_C0_THREAD(ff,tt);
                temp_Cell=C_UDSI(c0,t0,0);
                temp_face=F_UDSI(ff,tt,0);
                k_Cell=C_K_L(c0,t0);
                ro_Cell=C_R(c0,t0);
                cp_Cell=C_CP(c0,t0);
                v_face=F_V(ff,tt);
                P_Cell=C_P(c0,t0)-PRESSURE_VAPOR_0;
                BOUNDARY_FACE_GEOMETRY(ff,tt,A,ds,es,A_by_Es,dr0);
                c0_shadow = F_C0(ff_shadow,tt_shadow);
                t0_shadow = F_C0_THREAD(ff_shadow,tt_shadow);
                temp_Cell_shadow=C_UDSI(c0_shadow,t0_shadow,0);
                temp_face_shadow=F_UDSI(ff_shadow,tt_shadow,0);
                k_Cell_shadow=C_K_L(c0_shadow,t0_shadow);
                ro_Cell_shadow=C_R(c0_shadow,t0_shadow);
                cp_Cell_shadow=C_CP(c0_shadow,t0_shadow);
                v_face_shadow=F_V(ff_shadow,tt_shadow);
                BOUNDARY_FACE_GEOMETRY(ff_shadow,
tt_shadow,A,ds_shadow,ess,A_by_Ess,dr0s);
                //=====================================
                temp_face=TEMP_INTERFACE [iii];
                aa1=HFG/R_R*(1.0/T_REF-1.0/temp_face);
                PRESSURE_INTERFACE=P_REF*exp(aa1);
                aa1=2.0*ZIGMA/(2.0-ZIGMA);
                aa2=1/sqrt(2*PI_num*R_R);
                aa3=((P_OP_2+P_Cell)/sqrt(temp_Cell)-
PRESSURE_INTERFACE/sqrt(temp_face));
                M_DOT[iii]=aa1*aa2*aa3;
                VEL_INTERFACE_VAPOR[iii] =
VEL_INTERFACE_VAPOR[iii]+URF_VEL*(M_DOT[iii]/ro_Cell-
VEL_INTERFACE_VAPOR[iii]);
                VEL_INTERFACE_WICK[iii]=
VEL_INTERFACE_VAPOR[iii]*ro_Cell/ro_Cell_shadow;
                //=====================================
                k_ds=k_Cell/ds;
                k_ds_shadow=k_Cell_shadow/ds_shadow;
                aa1=temp_Cell_shadow*k_ds_shadow;
                aa2=temp_Cell*k_ds;
                aa3=-2.0*ZIGMA/(2.0-
ZIGMA)*1/sqrt(2*PI_num*R_R)*((P_OP_2+P_Cell)/sqrt(temp_Cell))*HFG;
                bb1=k_ds_shadow;
                bb2=k_ds;
                bb3=-2.0*ZIGMA/(2.0-
ZIGMA)*1/sqrt(2*PI_num*R_R)*(PRESSURE_INTERFACE/sqrt(temp_face))*HFG/te
mp_face;
```

```
                    TEMP_INTERFACE [iii] =TEMP_INTERFACE
[iii]+URF_TEMP*((aa1+aa2+aa3)/(bb1+bb2+bb3)-TEMP_INTERFACE [iii]);
          }
          end_f_loop(ff, tt)
                    bb4=bb4;
}
/*****************************************************************
********   THIS UDF IS USED TO UPDATE THE PARAMETERS   ********
********    NEEDED FOR THE NEXT TIME STEP                        ********
*****************************************************************/
DEFINE_EXECUTE_AT_END(TRANSIENT)
{
          FILE *fp1;
          FILE *fp2;
          //====================================
          if (floor(N_TIME/N_print)*N_print == N_TIME)
          {
                    fp1 = fopen ("Data_0Transient.txt", "a");
                    fprintf (fp1, "%E   %E   %E   %E   %E   %E   %E   %E   %E   %E   %E
%E   %E   %E   %E   %E   %E   %E   %E   %E   %E   %E   %E   %E   %E\n",
CURRENT_TIME,
P_OP_2,TEMP_WALL_MAX,TEMP_WALL_MIN,VEL_MAX_U_VAPOR,Q_OUT,Q
_IN,Q_VAPOR,Q_VAPOR_E,Q_VAPOR_C,M_DOT_BALANCE,MASS_VAPOR2,M
ASS_LIQUID_2,VEL_MAX_V_VAPOR,VEL_MAX_U_WICK,X_SEPARATION,X_
VEL_MAX_U_VAPOR,X_VEL_MAX_U_WICK,PRESSURE_VAPOR-
P_VAPOR_MIN,PRESSURE_WICK_MAX-
PRESSURE_WICK_MIN,DENSITY_VAPOR,DENSITY_VAPOR_E,DENSITY_VAP
OR_C,DENSITY_VAPOR_MAX,DENSITY_VAPOR_MIN);
                    fclose (fp1);
          }
          //====================================
          LIQUID_DENSITY=MASS_LIQUID_2/(WICK_VOLUME);
          P_OP_1=P_OP_2;
          MASS_VAPOR1=MASS_VAPOR2;
          MASS_LIQUID_1=MASS_LIQUID_2;
          N_ITERATION=0;
          N_TIME=N_TIME+1;
}
/*****************************************************************
********   HIS UDF IS USED TO COMPUTE AND PRINT DATA    ********
********     ON THE WICK-VAPOR INTERFACE                        ********
*****************************************************************/
DEFINE_EXECUTE_AT_END(WICK_VAPOR_INTERFACE_PRINTOUT)
{
          FILE *fp2;
          double data_interface [1000][10];
```

```
double NV_VEC(f_area);
double d_area;
double ru;
double x_separation1,x_separation2
        //====================================
        for (iii=0;iii<1000;iii=iii+1)
        {
                for (jjj=0;jjj<10;jjj=jjj+1)
                {
                        data_interface [iii][jjj]=12345.0;
                }
        }
        dd=Get_Domain(1);
        zone_ID = MARZ_VAPOR_WICK_ID;
        tt = Lookup_Thread(dd,zone_ID);
        zone_ID = MARZ_WICK_VAPOR_ID;
        tt_shadow = Lookup_Thread(dd,zone_ID);
        PRESSURE_VAPOR=-1.0E15;
        P_VAPOR_MIN=1.0E15;
        PRESSURE_WICK_MAX=-1.0E15;
        PRESSURE_WICK_MIN=1.0E15;
        iii=-1;
        begin_f_loop (ff,tt)
        {
                iii=iii+1;
                c0 = F_C0(ff,tt);
                t0 = F_C0_THREAD(ff,tt);
                ff_shadow=ff_VAPOR_WICK [iii];
                c0_shadow= F_C0(ff_shadow,tt_shadow);
                t0_shadow= F_C0_THREAD(ff_shadow,tt_shadow);
                F_CENTROID(x,ff,tt);
                aa1=C_P(c0,t0);
                temp_Cell= C_UDSI(c0, t0, 0);
                ru=P_OP_2/R_R/temp_Cell;
                F_AREA(f_area,ff,tt);
                d_area = NV_MAG(f_area);
                data_interface [iii][0]=x[0];
                data_interface [iii][1]=F_V(ff,tt);
                data_interface [iii][2]=F_V(ff_shadow,tt_shadow);
                data_interface [iii][3]=aa1;
                data_interface [iii][4]=M_DOT[iii]*d_area;
                data_interface [iii][5]=ru;
                aa1=C_P(c0,t0);
                bb1=C_P(c0_shadow,t0_shadow);
                if (aa1>PRESSURE_VAPOR)
                {
```

```
                PRESSURE_VAPOR=aa1;
        }
        if (aa1<P_VAPOR_MIN)
        {
                P_VAPOR_MIN=aa1;
        }
        if (bb1>PRESSURE_WICK_MAX)
        {
                PRESSURE_WICK_MAX=bb1;
        }
        if (bb1<PRESSURE_WICK_MIN)
        {
                PRESSURE_WICK_MIN=bb1;
        }
}
end_f_loop (ff,tt)
        bb4=bb4;
for (i=0;i<1000;i=i+1)
{
        for (iii=0; iii<1000-1;iii=iii+1)
        {
                if (data_interface [iii][0]>data_interface [iii+1][0])
                {
                        for (jjj=0;jjj<10;jjj=jjj+1)
                        {
                                bb4=data_interface [iii+1][jjj];
                                data_interface [iii+1][jjj]=data_interface
[iii][jjj];

                                data_interface [iii][jjj]=bb4;
                        }
                }
        }
}
//======================================
VEL_MAX_V_VAPOR=-1.0;
X_SEPARATION=0.0;
PRESSURE_VAPOR_0=0.0;
Q_VAPOR_E=0.0;
Q_VAPOR_C=0.0;
DENSITY_VAPOR_E=0.0;
DENSITY_VAPOR_C=0.0;
i=0;
j=0;
for (iii=0;iii<1000;iii=iii+1)
{
        if (data_interface [iii][0]<99.0)
```

```
                        {
                                if (VEL_MAX_V_VAPOR < fabs(data_interface [iii][1]))
                                {
                                        VEL_MAX_V_VAPOR=fabs(data_interface
[iii][1]);
                                }
                                if (data_interface [iii][4]<0)
                                {
                                        i=i+1;
                                        Q_VAPOR_E=Q_VAPOR_E+data_interface
[iii][4];

        DENSITY_VAPOR_E=DENSITY_VAPOR_E+data_interface [iii][5];
                                }
                                if (data_interface [iii][4]>0)
                                {
                                        j=j+1;
                                        Q_VAPOR_C= Q_VAPOR_C+data_interface
[iii][4];

        DENSITY_VAPOR_C=DENSITY_VAPOR_C+data_interface [iii][5];
                                }
                        }
                        if (data_interface [iii][1]*data_interface [iii+1][1]< 0.0)
                        {
                                x_separation1=data_interface [iii][0];
                                aa2=data_interface [iii][1];
                                aa3=data_interface [iii][3];
                                x_separation2=data_interface [iii+1][0];
                                bb2=data_interface [iii+1][1];
                                bb3=data_interface [iii+1][3];
                                bb4=(bb2-aa2)/(x_separation2-x_separation1);
                                X_SEPARATION=1/bb4*(0.0-aa2)+x_separation1;
                                bb4=(bb3-aa3)/(x_separation2-x_separation1);
                                PRESSURE_VAPOR_0=bb4*(X_SEPARATION-
x_separation1)+aa3;
                        }
                }
                Q_VAPOR_E=Q_VAPOR_E*HFG;
                Q_VAPOR_C=-Q_VAPOR_C*HFG;
                DENSITY_VAPOR_E=DENSITY_VAPOR_E/i;
                DENSITY_VAPOR_C=-DENSITY_VAPOR_C/j;
                //=====================================
                if (floor(N_TIME/N_print_time)*N_print_time == N_TIME)
                {
                        fp2 = fopen ("Data_1Interface.txt", "a");
```

```
            fprintf (fp2, "Time= %E \n", CURRENT_TIME);
            for (iii=0;iii<1000;iii=iii+1)
            {
                if (data_interface [iii][0]<99.0)
                {
                    fprintf (fp2, "%E   %E   %E   %E   %E
%E\n",data_interface [iii][0],data_interface [iii][1],data_interface [iii][2],data_interface
[iii][3]-PRESSURE_VAPOR_0,data_interface [iii][4],data_interface [iii][5]);
                }
            }
            fclose (fp2);
        }
}
/*************************************************************
********   THIS UDF IS USED TO COMPUTE AND PRINT DATA ********
********     ON THE WICK AND VAPOR DOMAINS                ********
*************************************************************/
DEFINE_EXECUTE_AT_END(WICK_VAPOR_DOMAINS_PRINTOUT)
{
    double data_interface [1000][10];
    double NV_VEC(f_area);
    double d_area;
    double ru;
//====================================
    VEL_MAX_U_VAPOR=-1.0;
    DENSITY_VAPOR=0.0;
    DENSITY_VAPOR_MAX=-1.0E15;
    DENSITY_VAPOR_MIN=1.0E15;
    zone_ID = VAPOR_Core_ID;
    t0 = Lookup_Thread(dd,zone_ID);
    iii=-1;
    begin_C_loop (c0,t0)
    {
        iii=iii+1;
        if (VEL_MAX_U_VAPOR < fabs(C_U(c0,t0)))
        {
            VEL_MAX_U_VAPOR=fabs(C_U(c0,t0));
            C_CENTROID(x,c0,t0);
            X_VEL_MAX_U_VAPOR=x[0];
        }
        temp_Cell= C_UDSI(c0, t0, 0);
        ru=P_OP_2/R_R/temp_Cell;
        if (DENSITY_VAPOR_MAX < ru )
        {
            DENSITY_VAPOR_MAX = ru;
        }
```

```
		if (DENSITY_VAPOR_MIN > ru )
		{
			DENSITY_VAPOR_MIN = ru;
		}
		DENSITY_VAPOR=DENSITY_VAPOR+ru;
	}
	end_C_loop (c0,t0)
		bb4=bb4;
	DENSITY_VAPOR=DENSITY_VAPOR/(iii+1);
	//=====================================
	VEL_MAX_U_WICK=-1.0;
	zone_ID = WICK_Core_ID;
	t0 = Lookup_Thread(dd,zone_ID);
	begin_C_loop (c0,t0)
	{
		if (VEL_MAX_U_WICK < fabs(C_U(c0,t0)))
		{
			VEL_MAX_U_WICK=fabs(C_U(c0,t0));
			C_CENTROID(x,c0,t0);
			X_VEL_MAX_U_WICK=x[0];
		}
	}
	end_C_loop (c0,t0)
		bb4=bb4;
	//=====================================
	Q_VAPOR=0.0;
	zone_ID = VAPOR_Core_ID;
	t0 = Lookup_Thread(dd,zone_ID);
	for (iii=0;iii<1000;iii=iii+1)
	{
		for (jjj=0;jjj<10;jjj=jjj+1)
		{
			data_interface [iii][jjj]=12345.0;
		}
	}
	iii=-1;
	begin_C_loop (c0,t0)
	{
		c_face_loop(c0, t0, i)
		{
			ff = C_FACE(c0,t0,i);
			tt = C_FACE_THREAD(c0,t0,i);
			F_CENTROID(x,ff,tt);
			aa1=x[0];
			aa2=x[1];
			C_CENTROID(x,c0,t0);
```

```
                        bb1=x[0];
                        bb2=x[1];
                        if ((aa1 < x_separation2) && (aa1 > x_separation1) && (fabs(aa2-
bb2)<1.0E-7))
                        {
                                iii=iii+1;
                                F_AREA(f_area,ff,tt);
                                d_area = NV_MAG(f_area);
                                data_interface [iii][0]=bb2;
                                data_interface [iii][1]=bb1;
                                data_interface [iii][2]=d_area;
                                data_interface [iii][3]=F_U(c0,t0);
                                data_interface [iii][4]=C_R(c0,t0);
                        }
                }
        }
        end_C_loop (c0,t0)
                bb4=bb4;
        //=====================================
        for (i=0;i<1000;i=i+1)
        {
                for (iii=0; iii<1000-1;iii=iii+1)
                {
                        if (data_interface [iii][0]>data_interface [iii+1][0])
                        {
                                for (jjj=0;jjj<10;jjj=jjj+1)
                                {
                                        bb4=data_interface [iii+1][jjj];
                                        data_interface [iii+1][jjj]=data_interface [iii][jjj];
                                        data_interface [iii][jjj]=bb4;
                                }
                        }
                }
        }
        //=====================================
        for (iii=0;iii<1000;iii=iii+2)
        {
                if ((data_interface [iii][0]< 99.0) && (data_interface [iii][1]< 99.0))
                {
                        aa1=(data_interface [iii+1][3]-data_interface
[iii][3])/(data_interface [iii+1][1]-data_interface [iii][1]);
                        bb1=aa1*(X_SEPARATION-data_interface
[iii][1])+data_interface [iii][3];
                        data_interface [iii][5]=bb1;
                        data_interface [iii][6]=bb1*data_interface [iii][2]*data_interface
[iii][4];
```

```
                    Q_VAPOR=Q_VAPOR+data_interface [iii][6];
                }
        }
        Q_VAPOR=Q_VAPOR*HFG;
}
/*****************************************************************
********   THIS UDF IS USED TO COMPUTE AND PRINT DATA  ********
********    ON THE OUTSIDE WALL OF HEAT PIPE                  ********
*****************************************************************/
DEFINE_EXECUTE_AT_END(WALL_PRINTOUT)
{
        FILE *fp3;
        double data_WALL [1000][10];
        double NV_VEC(f_area);
        double d_area;
        double ru;
        //====================================
        TEMP_WALL_MAX=-10.0E10;
        TEMP_WALL_MIN=10.0E10;
        Q_IN=0.0;
        Q_OUT=0.0;
        zone_ID = WALL_heating_ID;
        tt = Lookup_Thread(dd,zone_ID);
        begin_f_loop (ff,tt)
        {
                c0 = F_C0(ff,tt);
                t0= F_C0_THREAD(ff,tt);
                temp_Cell=C_UDSI(c0,t0,0);
                temp_face=F_UDSI(ff,tt,0);
                k_Cell=C_K_L(c0,t0);
                BOUNDARY_FACE_GEOMETRY(ff,tt,A,ds,es,A_by_Es,dr0);
                F_AREA(f_area,ff,tt);
                d_area = NV_MAG(f_area);
                Q_IN=Q_IN+(k_Cell*(temp_Cell-temp_face)/ds)*d_area;
                if (TEMP_WALL_MAX < F_UDSI(ff,tt,0))
                {
                        TEMP_WALL_MAX=F_UDSI(ff,tt,0);
                }
        }
        end_f_loop (ff,tt)
                bb4=bb4;
        zone_ID = WALL_Cooling_ID;
        tt = Lookup_Thread(dd,zone_ID);
        begin_f_loop (ff,tt)
        {
                c0 = F_C0(ff,tt);
```

```
		t0= F_C0_THREAD(ff,tt);
		temp_Cell=C_UDSI(c0,t0,0);
		temp_face=F_UDSI(ff,tt,0);
		k_Cell=C_K_L(c0,t0);
		BOUNDARY_FACE_GEOMETRY(ff,tt,A,ds,es,A_by_Es,dr0);
		F_AREA(f_area,ff,tt);
		d_area = NV_MAG(f_area);
		Q_OUT=Q_OUT+(k_Cell*(temp_Cell-temp_face)/ds)*d_area;
		if (TEMP_WALL_MIN > F_UDSI(ff,tt,0))
		{
			TEMP_WALL_MIN=F_UDSI(ff,tt,0);
		}
	}
	end_f_loop (ff,tt)
		bb4=bb4;
	//======================================
	for (iii=0;iii<1000;iii=iii+1)
	{
		for (jjj=0;jjj<10;jjj=jjj+1)
		{
			data_WALL [iii][jjj]=12345.0;
		}
	}
	zone_ID = WALL_heating_ID;
	tt = Lookup_Thread(dd,zone_ID);
	iii=-1;
	begin_f_loop (ff,tt)
	{
		iii=iii+1;
		F_CENTROID(x,ff,tt);
		xx=x[0];
		data_WALL [iii][0]=xx;data_WALL [iii][1]=F_UDSI(ff,tt,0);
	}
	end_f_loop (ff,tt)
		bb4=bb4;
	zone_ID = WALL_insulated_ID;
	tt = Lookup_Thread(dd,zone_ID);
	begin_f_loop (ff,tt)
	{
		iii=iii+1;
		F_CENTROID(x,ff,tt);
		xx=x[0];
		data_WALL [iii][0]=xx;data_WALL [iii][1]=F_UDSI(ff,tt,0);
	}
	end_f_loop (ff,tt)
		bb4=bb4;
```

```
    zone_ID = WALL_Cooling_ID;
    tt = Lookup_Thread(dd,zone_ID);
    begin_f_loop (ff,tt)
    {
        iii=iii+1;
        F_CENTROID(x,ff,tt);
        xx=x[0];
        data_WALL [iii][0]=xx;data_WALL [iii][1]=F_UDSI(ff,tt,0);
    }
    end_f_loop (ff,tt)
        bb4=bb4;
    //====================================
    for (i=0;i<1000;i=i+1)
    {
        for (iii=0; iii<1000-1;iii=iii+1)
        {
            if (data_WALL [iii][0]>data_WALL [iii+1][0])
            {
                for (jjj=0;jjj<2;jjj=jjj+1)
                {
                    bb4=data_WALL [iii+1][jjj];
                    data_WALL [iii+1][jjj]=data_WALL [iii][jjj];
                    data_WALL [iii][jjj]=bb4;
                }
            }
        }
    }

    //====================================
    if (floor(N_TIME/N_print_time)*N_print_time == N_TIME)
    {
        fp3 = fopen ("Data_2WALL.txt", "a");
        fprintf (fp3, "Time= %E \n", CURRENT_TIME);
        for (iii=0;iii<1000;iii=iii+1)
        {
            if (data_WALL [iii][0]<99.0)
            {
                fprintf (fp3, "%E   %E\n",data_WALL [iii][0],data_WALL
[iii][1]);
            }
        }
        fclose (fp3);
    }
}
/*****************************************************************
********  THIS UDF IS USED TO ASSIGN THE VELOCITY TO      ********
```

```
********  VAPOR-WICK INTERFACE ON THE VAPOR DOMAIN ********
*****************************************************************/
DEFINE_PROFILE(VELOCITY_VAPOR_WICK, tt, ii)
{
        iii=-1;
        begin_f_loop(ff, tt)
        {
                iii=iii+1;
                F_PROFILE(ff, tt, ii) = -VEL_INTERFACE_VAPOR[iii];
        }
        end_f_loop(ff, tt)
}
/*****************************************************************
********   THIS UDF IS USED TO ASSIGN THE VELOCITY TO     ********
********   VAPOR-WICK INTERFACE ON THE WICK DOMAIN   ********
*****************************************************************/
DEFINE_PROFILE(VELOCITY_WICK_VAPOR, tt, ii)
{
        iii=-1;
        begin_f_loop(ff, tt)
        {
                iii=iii+1;
                F_PROFILE(ff, tt, ii) =
VEL_INTERFACE_WICK[iii_WICK_VAPOR[iii]];
        }
        end_f_loop(ff, tt)
}
/*****************************************************************
********   THIS UDF IS USED TO ASSIGN THE TEMPERATURE  ********
********  TO VAPOR-WICK INTERFACE ON THE WICK DOMAIN ******
*****************************************************************/
DEFINE_PROFILE(TEMPERATURE_WICK_VAPOR, tt, ii)
{
        iii=-1;
        begin_f_loop(ff, tt)
        {
                iii=iii+1;
                F_PROFILE(ff, tt, ii) = TEMP_INTERFACE [iii_VAPOR_WICK[iii]];
        }
        end_f_loop(ff, tt)
}
/*****************************************************************
********   THIS UDF IS USED TO ASSIGN THE TEMPERATURE   *******
********TO VAPOR-WICK INTERFACE ON THE VAPOR DOMAIN******
*****************************************************************/
DEFINE_PROFILE(TEMPERATURE_VAPOR_WICK, tt, ii)
```

```
{
        iii=-1;
        begin_f_loop(ff, tt)
        {
                iii=iii+1;
                F_PROFILE(ff, tt, ii) =TEMP_INTERFACE [iii];
        }
        end_f_loop(ff, tt)

}
/*****************************************************************
********   THIS UDF IS USED TO CALCULATE AND ASSIGN        *******
********   TEMPERATURE TO WALL-WICK INTERFACE BUT ON*******
********   THE WALL DOMAIN                                 ********
*****************************************************************/
DEFINE_PROFILE(TEMPERATURE_WALL_WICK, tt, ii)
{
        dd=Get_Domain(1);
        zone_ID = MARZ_WICK_WALL_ID;
        tt_shadow = Lookup_Thread(dd,zone_ID);
        iii=-1;
        begin_f_loop(ff, tt)
        {
                iii=iii+1;
                c0 = F_C0(ff,tt);
                t0 = F_C0_THREAD(ff,tt);
                temp_Cell=F_UDSI(c0,t0,0);
                temp_face=F_UDSI(ff,tt,0);
                k_Cell=C_K_L(c0,t0);
                BOUNDARY_FACE_GEOMETRY(ff,tt,A,ds,es,A_by_Es,dr0);
                ff_shadow=ff_WALL_WICK [iii];
                c0_shadow = F_C0(ff_shadow,tt_shadow);
                t0_shadow = F_C0_THREAD(ff_shadow,tt_shadow);
                temp_Cell_shadow=C_UDSI(c0_shadow,t0_shadow,0);
                temp_face_shadow=F_UDSI(ff_shadow,tt_shadow,0);
                k_Cell_shadow=C_K_L(c0_shadow,t0_shadow);
                BOUNDARY_FACE_GEOMETRY(ff_shadow,
tt_shadow,A,ds_shadow,ess,A_by_Ess,dr0s);
                k_ds=k_Cell/ds;
                k_ds_shadow=k_Cell_shadow/ds_shadow;
                aa1 =
(k_ds*temp_Cell+k_ds_shadow*temp_Cell_shadow)/(k_ds+k_ds_shadow);
                F_PROFILE(ff, tt, ii) =aa1;
        }
        end_f_loop(ff, tt)
                bb4=bb4;
```

```
}
/***************************************************************
********   THIS UDF IS USED TO CALCULATE AND ASSIGN      ********
********   TEMPERATURE TO WALL-WICK INTERFACE BUT ON********
********   THE WICK DOMAIN                                ********
******************************************************************/
DEFINE_PROFILE(TEMPERATURE_WICK_WALL, tt, ii)
{
        dd=Get_Domain(1);
        zone_ID = MARZ_WALL_WICK_ID;
        tt_shadow = Lookup_Thread(dd,zone_ID);
        iii=-1;
        begin_f_loop(ff, tt)
        {
                iii=iii+1;
                c0 = F_C0(ff,tt);
                t0 = F_C0_THREAD(ff,tt);
                temp_Cell=C_UDSI(c0,t0,0);
                temp_face=F_UDSI(ff,tt,0);
                k_Cell=C_K_L(c0,t0);
                BOUNDARY_FACE_GEOMETRY(ff,tt,A,ds,es,A_by_Es,dr0);
                ff_shadow=ff_WICK_WALL [iii];
                c0_shadow = F_C0(ff_shadow,tt_shadow);
                t0_shadow = F_C0_THREAD(ff_shadow,tt_shadow);
                temp_Cell_shadow=C_UDSI(c0_shadow,t0_shadow,0);
                temp_face_shadow=F_UDSI(ff_shadow,tt_shadow,0);
                k_Cell_shadow=C_K_L(c0_shadow,t0_shadow);
                BOUNDARY_FACE_GEOMETRY(ff_shadow,
tt_shadow,A,ds_shadow,ess,A_by_Ess,dr0s);
                k_ds=k_Cell/ds;
                k_ds_shadow=k_Cell_shadow/ds_shadow;
                aa1 =
(k_ds*temp_Cell+k_ds_shadow*temp_Cell_shadow)/(k_ds+k_ds_shadow);
                F_PROFILE(ff, tt, ii) =aa1;
        }
        end_f_loop(ff, tt)
                bb4=bb4;
}
/***************************************************************
********   THIS UDF IS USED TO CALCULATE AND ASSIGN      ********
********   TEMPERATURE TO COOLING WALL OF HEAT PIPE  ********
***************************************************************/
DEFINE_PROFILE(TEMPERATURE_COOLING, tt, ii)
{
        iii=-1;
        begin_f_loop(ff, tt)
```

```
        {
                iii=iii+1;
                c0 = F_C0(ff,tt);
                t0 = F_C0_THREAD(ff,tt);
                temp_Cell=C_UDSI(c0,t0,0);
                temp_face=F_UDSI(ff,tt,0);
                k_Cell=C_K_L(c0,t0);
                BOUNDARY_FACE_GEOMETRY(ff,tt,A,ds,es,A_by_Es,dr0);

        aa1=(temp_Cell+HTC*ds/k_Cell*TEMP_COOLING)/(1.0+HTC*ds/k_Cell);
                F_PROFILE(ff, tt, ii) =aa1;
        }
        end_f_loop(ff, tt)
                bb4=bb4;
}
/**************************************************************
********    THIS UDF IS USED TO ASSIGN HEAT FLUX TO         ********
********    THE HEATING WALL OF HEAT PIPE                   ********
**************************************************************/
DEFINE_PROFILE(WALL_HEAT_FLUX, tt, ii)
{
        begin_f_loop(ff, tt)
        {
                F_PROFILE(ff, tt, ii) =HEAT_FLUX;
        }
        end_f_loop(ff, tt)
}
/**************************************************************
********    THIS UDF IS USED TO CALCULATE AND RETURN  ********
********    THE LOCAL DENSITY OF THE VAPOR            ********
**************************************************************/
DEFINE_PROPERTY(VAPOR_DENSITY, c0, t0)
{
        temp_Cell= C_UDSI(c0, t0, 0);
        aa1=P_OP_2/R_R/temp_Cell;
        return aa1;
}
/**************************************************************
********   THIS UDF IS USED TO CALCULATE AND RETURN    ********
********    THE DENSITY OF THE LIQUID                  ********
**************************************************************/
DEFINE_PROPERTY(LIQUID_DENSITY, c0, t0)
{
        aa1=MASS_LIQUID_2/(WICK_VOLUME);
        return aa1;
}
```

```
/*****************************************************************
********   THIS UDF IS USED TO CALCULATE AND RETURN     ********
********    THE THERMAL CONDUCTIVITY OF THE WICK        ********
*****************************************************************/
DEFINE_PROPERTY(WICK_CONDUCTIVITY, c0, t0)
{
        C_CENTROID(x,c0,t0);
        if ((x[1] <= Y_WICK_1) && (x[1] >= Y_WICK_2))
        {
                aa1=K_WICK_1;
        }
        else if ((x[1] < Y_WICK_2) && (x[1] >= Y_WICK_3))
        {
                aa1=K_WICK_2;
        }
        else
        {
                aa1=K_WICK_3;
        }
        return aa1;
}
/*****************************************************************
********   THIS UDF IS USED TO CALCULATE AND RETURN     ********
********    THE POROSITY OF THE WICK                    ********
*****************************************************************/
DEFINE_PROFILE(WICK_POROSITY, t0, ii)
{
        begin_C_loop(c0, t0)
        {
                C_CENTROID(x,c0,t0);
                if ((x[1] <= Y_WICK_1) && (x[1] >= Y_WICK_2))
                {
                        aa1=POROSITY1;
                }
                else if ((x[1] < Y_WICK_2) && (x[1] >= Y_WICK_3))
                {
                        aa1=POROSITY2;
                }
                else
                {
                        aa1=POROSITY3;
                }
                C_PROFILE(c0, t0, ii) =a11;
        }
        end_C_loop(ff, tt)
}
```

```
/*****************************************************************
********   THIS UDF IS USED TO CALCULATE AND RETURN      ********
********    THE VISCOUS RESISTANCE OF THE WICK           ********
*****************************************************************/
DEFINE_PROFILE(VISCOUS_RESISTANCE, t0, ii)
{
        begin_C_loop(c0, t0)
        {
                C_CENTROID(x,c0,t0);
                if ((x[1] <= Y_WICK_1) && (x[1] >= Y_WICK_2))
                {
                        aa1=VISCOUS_RES_1;
                }
                else if ((x[1] < Y_WICK_2) && (x[1] >= Y_WICK_3))
                {
                        aa1=VISCOUS_RES_2;
                }
                else
                {
                        aa1=VISCOUS_RES_3;
                }
                C_PROFILE(c0, t0, ii) =aa1;
        }
        end_C_loop(ff, tt)
}
/*****************************************************************
********   THIS UDF IS USED TO CALCULATE AND RETURN      ********
********    THE INERTIAL RESISTANCE OF THE WICK          ********
*****************************************************************/
DEFINE_PROFILE(INERTIAL_RESISTANCE, t0, ii)
{
        begin_C_loop(c0, t0)
        {
                C_CENTROID(x,c0,t0);
                if ((x[1] <= Y_WICK_1) && (x[1] >= Y_WICK_2))
                {
                        aa1=INERTIAL_RES_1;
                }
                else if ((x[1] < Y_WICK_2) && (x[1] >= Y_WICK_3))
                {
                        aa1=INERTIAL_RES_2;
                }
                else
                {
                        aa1=INERTIAL_RES_3;
                }
```

```
		C_PROFILE(c0, t0, ii) =aa1;
	}
	end_C_loop(ff, tt)
}
/***************************************************************
********   THIS UDF IS USED TO CALCULATE AND RETURN     ********
********    THE UDS UNSTEADY TERMS                      ********
***************************************************************/
DEFINE_UDS_UNSTEADY(UDS_UNSTEADY_REVISION,c,t,i,apu,su)
{
	double physical_dt, vol, rho, rho_old, phi_old;
	physical_dt = RP_Get_Real("physical-time-step");
	zone_ID = THREAD_ID (t);
	vol = C_VOLUME(c,t);
	C_CENTROID(x,c,t);
	if ((x[1] <= Y_WICK_1) && (x[1] >= Y_WICK_2))
	{
		POROSITY=POROSITY1;
	}
	else if ((x[1] < Y_WICK_2) && (x[1] >= Y_WICK_3))
	{
		POROSITY=POROSITY2;
	}
	else
	{
		POROSITY=POROSITY3;
	}
	RO_L=LIQUID_DENSITY;
	if (zone_ID == WICK_Core_ID)
	{
		aa1=(1.0-POROSITY)*RO_S*CP_S+POROSITY*RO_L*CP_L;
		aa2=aa1/CP_L;
		rho = aa2;
		rho_old=aa2;
	}
	else
	{
		rho = C_R(c,t);
		rho_old=C_R_M1(c,t);
	}
	*apu = -rho*vol/physical_dt;
	phi_old = C_STORAGE_R(c,t,SV_UDSI_M1(i));
	*su  = rho_old*vol*phi_old/physical_dt;
}
/***************************************************************
********   THIS UDF IS USED TO CALCULATE AND RETURN     ********
```

```
********    THE DIFFUSIVITY OF UDS IN THE WICK                 ********
*********************************************************************/
DEFINE_DIFFUSIVITY(WICK_DIFFUSIVITY, c0, t0, i)
{
        C_CENTROID(x,c0,t0);
        if ((x[1] <= Y_WICK_1) && (x[1] >= Y_WICK_2))
        {
                aa1=D_WICK_1;
        }
        else if ((x[1] < Y_WICK_2) && (x[1] >= Y_WICK_3))
        {
                aa1=D_WICK_2;
        }
        else
        {
                aa1=D_WICK_3;
        }
        return aa1;
}
/*********************************************************************
********   THIS UDF IS USED TO CALCULATE AND RETURN   ********
********    THE DYNAMIC TIME STEPS                             ********
*********************************************************************/
DEFINE_DELTAT(TIME_STEP,d)
{
        TIME_STEP=0.01*pow(1.20,N_TIME-1);
        TIME_STEP=floor(TIME_STEP*1000)/1000;
        if (TIME_STEP >= 1)
        {
                TIME_STEP=1.0;
        }
        return TIME_STEP;
}
/*********************************************************************
********            THE END                                    ********
********            THE END                                    ********
********            THE END                                    ********
*********************************************************************/
```